Parametric Variation Identification Techniques in Nonlinear Dynamical Systems

by

Andrew R. Sloboda

A dissertation submitted in partial fulfillment
of the requirements for the degree of
Doctor of Philosophy
(Mechanical Engineering)
in the University of Michigan
2013

Doctoral Committee:

Associate Professor Bogdan Epureanu, Chair
Professor Karl Grosh
Assistant Professor Kenn R. Oldham
Professor Nickolas Vlahopoulos

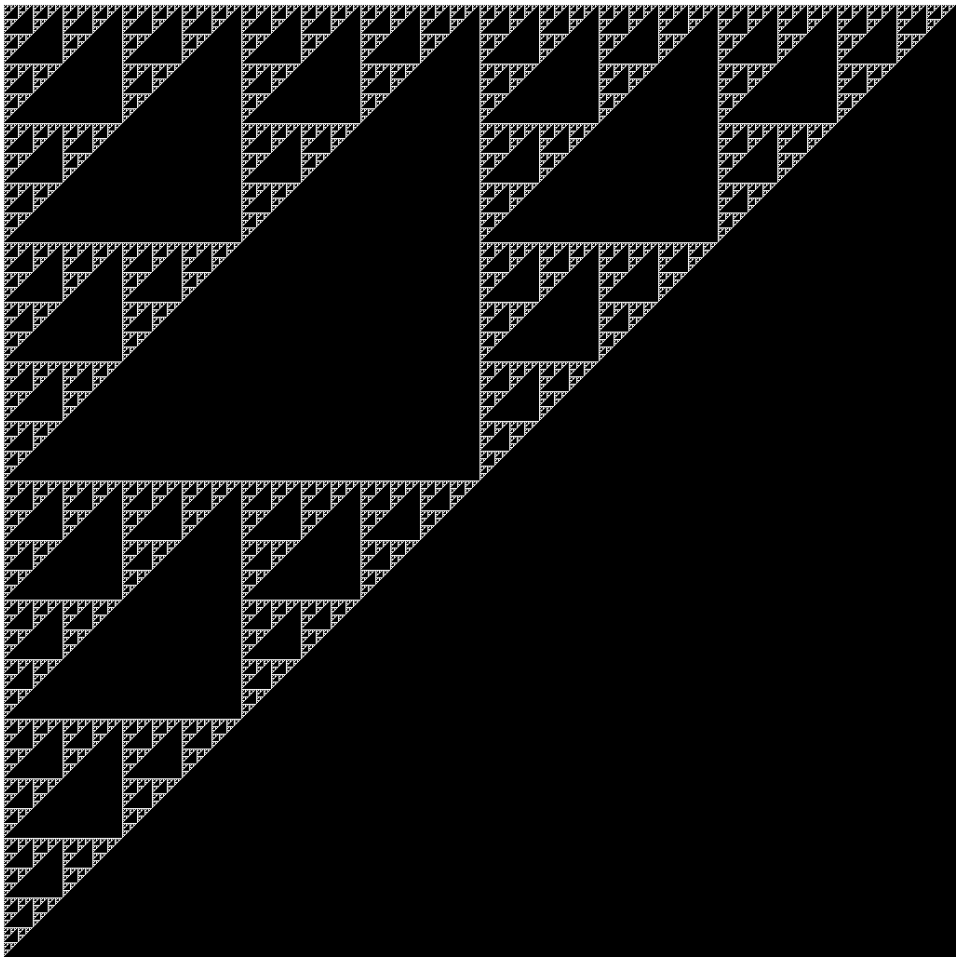

2013

To Darcée, the love of my life.
And to my parents, who have blessed me in innumerable ways.

A C K N O W L E D G M E N T S

I would like to thank my advisor Dr. Bogdan Epureanu for his support of my research. His willingness to offer advice and generously give of his time were critical to moving my research forward. He has shown me what true dedication to one's work looks like. I would also like to thank the members of my committee, Dr. Karl Grosh, Dr. Kenn Oldham, and Dr. Nickolas Vlahopoulos for the constructive feedback they have imparted regarding my research and this dissertation. A special thanks to Dr. Oldham for providing me with the opportunity to support myself and gain teaching experience by serving as the graduate student instructor for his class *ENG 561 Design of Digital Control Systems*.

I would also like to extend thanks to all of the members of our research group who have helped me along the way. Special thanks to Olguta Marinescu for sharing the experimental space with me and to Kiran D'Souza for helping me quickly get up to speed when I sought to further develop work in the area of system augmentation.

Away from the lab, I would like to thank Charles and Dianne Roeper, whose friendship and mentoring has anchored me during my time at Michigan. Thanks are also owed to them for letting me camp out in their basement for an entire month!

Lastly, I want thank my family. My parents have worked hard to breathe wisdom and blessing into my life. Mom and Dad, I owe you more than it is possible to express. Thank you for setting the bar so high in terms of how you live your lives.

Thanks to my wife Darcée for her unwavering support, wisdom, and love. Darcée, I am so fortunate to have you by my side as we journey together.

TABLE OF CONTENTS

LIST OF FIGURES

LIST OF TABLES

LIST OF ABBREVIATIONS

DSPI direct system parameter identification

eSV embedded sensitivity vector

eSVF embedded sensitivity vector field

ePCA embedded point cloud averaging

GMRPT generalized minimum rank perturbation theory

MEMS micro-electro-mechanical systems

PCA point cloud averaging

SOD smooth orthogonal decomposition

SV sensitivity vector

SVF sensitivity vector field

CHAPTER 1

Introduction

Characterizing variations in system parameters is essential in a variety of sensing and diagnostic applications. Many of these applications have traditionally belonged to the field of structural health monitoring, where parameter variations can indicate that a structure, such as a bridge or an airframe, has been damaged or otherwise modified. However, with the increasing ubiquity of micro-electro-mechanical systems (MEMS), characterizing variations is important not only on the macro-scale but the micro-scale as well. Tapping-mode atomic force microscopes may immediately spring to mind, but particular classes of micro-sensors, such as those designed to measure trace amounts of chemical or biological material, also require precise measurement of parameter variations in order to be effective. These kinds of sensors are employed in a diverse array of applications, ranging from the diagnosis of bacterial infections to the characterization of substances for counter-terrorism screenings. Thus, the ability to determine in what way and to what extent system parameters have changed is an important task.

Active, vibration-based methods are one of the most common means of identifying and quantifying system parameter variations. For a system subjected to a given excitation, a particular change in the system parameters will result in some corresponding change in the dynamic response. Monitoring the system response is thus sufficient to capture any variations in the system parameters so long as the changes in the response are measurable and can be mapped to specific parameter variations.

Within the purview of vibration-based methods, the most commonly used techniques involve the measurement of changes in modal parameters, such as resonant frequency shifts. Frequency-shift or other modal methods are generally effective, and have served as the basis for many successful sensors and devices. However, modal methods can be ineffective under several circumstances: when a system has a low quality factor, when a system is insensitive to the parameters of interest, when a

system is significantly nonlinear, or when multiple simultaneous parameter changes need to be distinguished.

Sensitivity vector fields (SVFs) are one alternative to modal-based methods. SVFs are composed of sets of vectors that quantify how a system attractor deforms due to parametric variations. Individual fields are first constructed by sampling system trajectories that are diverging under known parametric variations. The resulting snapshots of known deformation are then stored and can be used as a reference to characterize any unprescribed variations in system parameters that occur at a later time. The SVF approach has several advantages. In many cases, using SVF analysis allows nonlinear features of a system to be enhanced and exploited to increase sensitivity rather than hindering the interrogation (as is the case for modal methods). Moreover, the simultaneous sensing of multiple parameter variations with a single sensor is possible since vector, rather than scalar, quantities are measured.

A second approach to dealing with system nonlinearities that cause the failure of traditional modal methods is to cast a given nonlinear system model within a larger, linear system model. In this process of system augmentation, each nonlinearity in the original system model is replaced by a new linear variable. Differential equations that describe the evolution of these new variables are added to the model, but the added equations are forced in such a way that the new variables evolve identically to the original nonlinearities. The augmented linear system can then be used in conjunction with traditional modal analysis techniques in order to determine any parameter variations that have occurred. Although there are many options for determining parameter variations from modal data, one choice is a process known as generalized minimum rank perturbation theory (GMRPT).

This dissertation further develops the SVF and system augmentation methodologies so that they can be effectively applied to real, physical systems.

1.1 Background

Many vibration-based methods have been developed to detect and quantify variations in system parameters. A fairly comprehensive review of these methods in the context of structural health monitoring and damage detection can be found in works by Doebling [1, 2]. Uniting these diverse methods is their reliance on the measurement of changes in modal parameters (e.g. frequencies, mode shapes, or modal damping) as the means of detecting variations in system parameters. Thus, almost all of these methods are inherently limited to linear models and cannot account for nonlinear

effects. In addition, usually only one parameter variation can be reliably detected at a time and it may be difficult to discriminate between variations in parameters of interest and variations in other parameters, such as might be caused by a drift in environmental conditions. More exotic methods that make use of subspace identification and updating [3], neural networks [4, 5], or wavelet analysis [6, 7, 8] are also possible. However, these again primarily focus on linear systems.

When a system has significant damping, the reduced quality factor can cause problems in trying to characterize parameter variations via modal methods. This is primarily because resonance peaks are attenuated and it becomes increasingly difficult to identify frequency shifts clearly. For micro-scale systems, the need for a high quality factor is of particular interest because it may often be necessary for these systems to operate in highly damped liquid environments [9, 10, 11, 12]. For instance, many different micro-scale mass sensors have been successfully designed that operate in low damping environments of vacuum or air [13, 14]. However, it took a creative approach by Burg and collaborators, who constructed a resonator that has the flow channeled within the vibrating structure itself, to arrive at an effective micro-sensor for measuring micro-particles in liquids [15, 16].

For over a decade, different methods for quantifying variations in systems where modal methods can fail have been in development. These include a diverse range of techniques for nonlinear systems. One such technique is chaotic interrogation [17, 18, 19, 20], where a system is excited by a chaotic signal and then analyzed based on its performance as a filter for that signal. Another technique is state space interrogation and reconstruction [21, 22, 23, 24] where errors in making predictions are tied to the identification of parameter variations. Further techniques, including those that make use of Lyapunov exponents [25], those that consider bifurcation morphing [26, 27], and others [28, 29] have also been proposed. However, each of these methods is also limited in some significant way; for instance, state space reconstruction can detect variations in only a single parameter and chaotic interrogation requires a chaotic input or forcing.

Sensitivity vector fields (SVFs) [30, 31], which quantify changes in the morphology of system attractors, are an attractive alternative identification method. SVFs have proven to be a reliable means of identifying parameter variations and remain effective even in cases where other vibration-based methods fail. Originally developed for structural health monitoring in mechanical systems [32], SVF techniques have since been used to detect parameter variations in a variety of simulated dynamical systems, including tapping-mode atomic force microscopes [33, 34]. Limited work has also

been performed to show that sensitivity vector fields can be generated in experimental systems [35]. However, fundamental questions about what kind of dynamics should be generated to maximize SVFs were never answered and are explored in this dissertation. Additionally, based on indications [36] that carefully designed feedback could further enhance SVF sensitivity, the design of feedback for SVFs is another topic presented in this dissertation.

For SVFs to be practical in real, physical systems, an approach to their construction that does not involve the entire state is required. Thankfully, a large body of work on representing systems in state space starting from time-series data is available [37, 38, 39, 40, 41, 42]. Constructing SVFs in time-delay coordinate embeddings is an additional topic developed in this dissertation.

When system nonlinearities are an impediment to established techniques, a completely different approach to identifying parameter variations is to cast the nonlinear system in a linear form via system augmentation so that modal methods are applicable. This approach was pioneered and developed by D'Souza et al. [43, 44] and has been applied to a wide range of simulated dynamical systems in many variations, such as with feedback [45, 46] and with multiple augmentations [47, 48]. It makes use of techniques such as direct system parameter identification (DSPI) [49, 50] and smooth orthogonal decomposition (SOD) [51, 52] to extract eigenvalue information from time series data and then uses this data in a process, such as GMRPT, to predict parameter variations. A method to reduce the noise content of the modal methods typically associated with system augmentation (DSPI and SOD) was also proposed by the same author [53]. The system augmentation framework is extended and further developed as one of the topics of this dissertation.

1.2 Research Aims

The aim of this research is to further develop the SVF and system augmentation methods for identifying parameter variations so they can be effectively applied to physical dynamical systems. Within this goal are four main research foci:

1. **Improving Fundamental Understanding of SVFs**
   Fundamental questions can be asked about the best way to go about producing a set of SVFs for a particular purpose. For instance, do chaotic or non-chaotic regimes produce more sensitive SVFs? Is there an optimal evolution time to allow trajectories to develop before sampling in order to maximize the sensitivity of a SVF? If a system is harmonically excited, should a particular phase be used

to generate the SVFs or should all phases be included equally? These types of basic questions are explored in this focus.

2. **Designing Feedback to Enhance SVF Performance**
   The key to effectively utilizing SVFs is the design of nonlinear feedback control to enhance system behavior. This feedback needs to provide system excitation that maximizes attractor deformations caused by changes in parameters of interest (thereby enhancing sensitivity) while minimizing attractor deformations caused by changes in other system parameters (thereby improving selectivity). We explore how to design such nonlinear feedback for simple linear and nonlinear systems in two ways: using feedback based on polynomial functions and using feedback based on spline surfaces.

3. **Constructing SVFs in Time-Delay Coordinate Embeddings**
   In all but the simplest physical systems, knowledge of the entire state is not possible; as the dimensionality of the system increases it can become increasingly difficult and expensive to measure the full state. Often, we may have access to only a single time-series: a sequence of scalar data points measured at successive times. If the system dynamics are low-dimensional, it is still possible to reconstruct the state space of the dynamical system using time-delay coordinate embeddings. How to implement SVFs in coordinate embeddings is demonstrated in this focus.

4. **Applying System Augmentation to Physical Systems**
   Past research into system augmentation has shown it to be a effective method for identifying parameter variations in simulated structural dynamics problems. In this focus, using system augmentation to analyze more general nonlinear systems having a state space form is investigated. Along with the development of additional techniques which make using GMRPT easier, system augmentation is successfully applied to physical systems in the form of analog circuits for the first time.

1.3 Dissertation Outline

With the exception of Chapter 6, each of the additional chapters of this thesis present detailed information related to the aims outlined in Section 1.2. These chapters are based on conference or journal papers and, as a result, there may be some repetition in

the presented background and methodology. A brief summary of each of the chapters is provided below:

- Chapter 2 presents a parametric study of SVFs to further develop fundamental understanding of the role the evolution time ΔT and the system dynamics play in the properties of constructed SVFs. It also proposes two different forms of feedback, one of fixed polynomial form and the other based on a spline surface, to enhance sensitivity vector field (SVF) performance. Optimizing this feedback tends to select for dynamics near bifurcation or stability boundaries.

- In Chapter 3, a complete method for constructing SVFs in time-delay embedded coordinates is presented. This method makes use of local modeling techniques and weighs neighborhood points in a unique way referred to as embedded point cloud averaging (ePCA). Data from simulations and experiments is generated and used to demonstrate the effectiveness of this method.

- Chapter 4 details work towards the design of an immersed, vibrating sensor that would harvest flow energy and effectively detect micro-scale particles in liquids. Although these design efforts were only partially successful, the forms of feedback proposed in Chapter 2 can be applied to simple models derived from the fluid-structure interaction simulation, with results suggesting feedback could be used to improve sensor performance.

- In Chapter 5, system augmentation methodology is extended to non-structural systems. A new method for extracting left eigenvector information from time series data using SOD is presented and system augmentation is performed experimentally for the first time. Discussion of finer points regarding sampling considerations and the filtering of noise is also included.

CHAPTER 2

Maximizing Sensitivity Vector Fields: A Parametric Study

2.1 Introduction

Changing the parameters of a dynamical system can sometimes result in significant changes in its qualitative behavior. Period-doubling and other types of bifurcations come to mind as examples of this type of phenomena. However, more often than not, parametric variations only change the quantitative behavior of a system. In such cases, after a parameter has been changed the attractor appears much as it did before, its structure undergoing only a subtle deformation. Determining whether or not parameters have changed in such cases and, if so, by how much, is important - arguably sometimes more important than if a qualitative change had occurred. As one example, consider systems prone to damage or degradation. In such systems, a parametric variation could indicate damage and a set amount of variation could indicate that maintenance is required or that it is no longer safe to continue operation. Being able to accurately monitor the level of parametric variations despite obvious qualitative changes in the dynamics is valuable in these cases and can inform decision-making regarding system intervention and its scheduling (adaptation, repair, replacement, etc.). As a second example, consider sensors. Many dynamics-based sensing devices, including MEMS mass sensors and tapping-mode atomic force microscopes (AFMs), rely on the detection of changes in the parameters of resonant microstructures. Although the variations are application specific (added mass in the case of MEMS mass sensors and substrate topology in the case of AFMs), they can all be classified as subtle parametric changes requiring detection and quantification.

The most common way of determining parametric variations has traditionally been via modal methods, in which changes in a dynamical system's resonant frequencies, mode shapes, or other modal parameters serve as indicators of parametric changes

[2, 54]. These methods are effective for linear systems with a high quality factor, but may not be as effective for highly damped or strongly nonlinear systems. When only one mode or resonant frequency is monitored, they are also limited to detecting only a single variation. This has spurred the development of alternate techniques for detecting parametric variations [55], including techniques designed specifically for nonlinear systems that look at attractor changes. Some examples include methods based on what is known as phase space warping [21, 22, 56] or other local features such as attractor variance [57] or cross-prediction error [17, 18]. Recently hyperchaotic excitation was suggested for use with such techniques [19]. One specific alternate method of detecting parametric variations within this broader family is based on sensitivity vector fields (SVFs) [58, 31]. SVFs are a measure of how the morphology of a system attractor changes when system parameters change. An individual sensitivity vector (SV) is constructed by sampling pairs of diverging trajectories, one from the nominal system and the other from the varied system. The collection of these vectors across the entire attractor forms a SVF. A set of SVFs, collected for known variations, can be used as a basis for identifying and quantifying future, unknown parametric variations of the system.

Because SVFs are composed of vector rather than scalar quantities, they can often be used to detect several different parametric variations simultaneously. This is because SVs generated as a result of multiple parametric variations can be resolved along different SVFs using, for example, proper orthogonal decomposition. SVFs are also effective for systems with strong nonlinearities. These two advantages make them well suited for detecting variations in a variety of systems including aeroelastic systems [32], vibrating cantilevers [35], and tapping-mode AFMs [34].

SVFs are most effective when selectively sensitive: that is, when they are sensitive to changes in parameters of interest and insensitive to changes in other parameters. To improve selective sensitivity, either the system dynamics need to be altered in some way to improve performance or only the most sensitive regions of the nominal attractor should be included. This paper considers both options as potential means of improving SVF performance. First, how widely sensitivity can vary across different regions of an attractor is demonstrated along with an indication of how selecting these regions for analysis could improve outcomes. Second, adding nonlinear terms to a system in the form of feedback and attempting to optimize this feedback for better results is considered.

2.2 SVF Theory

A SVF is made up of a collection of SVs distributed across the attractor of a dynamical system. Each SV is a vector quantifying the separation of two trajectories that have diverged over an evolution time ΔT having begun at a coincident initial state. One of the trajectories belongs to the dynamical system having its nominal parameters, while the other belongs to the dynamical system under some parametric variation. Taken together, the SVs in a SVF indicate how the nominal attractor will deform under a specific parametric variation. If SVFs are known for several different parametric variations, they can be used to quantify any future variations that occur.

Mathematically, consider the dynamical system described by the flow

$$\dot{\mathbf{x}} = \mathbf{f}(\mathbf{x}, p, t), \tag{2.1}$$

where $\mathbf{x}$ is the state vector and p is the parameter to be varied. A Taylor series can be used to describe the evolution of the variation about the nominal system trajectory having $\mathbf{x}(t) = \mathbf{x_0}(t)$ and $p = p_0$ via the variational equation

$$\frac{d}{dt}\delta\mathbf{x} = \mathbf{A}(t)\delta\mathbf{x} + \mathbf{b}(t)\delta p, \tag{2.2}$$

$$\text{where} \qquad \mathbf{A}(t) = \left.\frac{\delta\mathbf{f}}{\delta\mathbf{x}}\right|_{\substack{\mathbf{x}=\mathbf{x}_o \\ p=p_o}}, \tag{2.3}$$

$$\text{and} \qquad \mathbf{b}(t) = \left.\frac{\delta\mathbf{f}}{\delta p}\right|_{\substack{\mathbf{x}=\mathbf{x}_o \\ p=p_o}}. \tag{2.4}$$

Here $\delta\mathbf{x}$ is the state variation and δp is the parametric variation of the varied system. The expansion is truncated to include only linear terms, which makes it exact for linear systems. For nonlinear systems, the approximation is valid so long as all higher order terms remain much smaller than the first order terms. This will occur if both the state variation and the parameter variation remain small, although the state itself need not be small. Thus, for nonlinear systems there is a limit on the evolution time for which Eq. (2.2) will remain a valid approximation and this limit depends on the system, the initial state, and the size of the parametric variation(s).

If integrated over the evolution time, Eq. (2.2) can be expressed in the form of a map given by

$$\delta\mathbf{x}(t_o + \Delta T) = \Phi(t_o + \Delta T, t_o)\delta\mathbf{x}(t_o) + \mathbf{q}\delta p, \tag{2.5}$$

where Φ is the state transition matrix from time t_0 to time $t_0 + \Delta T$ and $\mathbf{q}\delta p$ is

the sensitivity vector. Φ depends only on $\mathbf{A}(\mathbf{t})$ given in Eq. (2.3) while the SV $\mathbf{q}\delta p$ depends on both $\mathbf{A}(\mathbf{t})$ in Eq. (2.3) and $\mathbf{b}(\mathbf{t})$ in Eq. (2.4).

If the trajectories used in constructing a SV are truly initially coincident so that $\delta\mathbf{x}(t_0) = \mathbf{0}$, then the separation of these two trajectories after evolution time ΔT is the sensitivity vector $\mathbf{q}\delta p$. As long as the evolution time remains short enough that the Taylor series truncation remains valid, the SV is linearly dependent on the parameter variation δp. This proportionality between the parameter variation and the SV forms the basis for using SVs to ascertain parametric variations. However, it can oftentimes be advantageous to consider the normalized SV given by $\mathbf{q}$. Here q represents the sensitivity per unit of parametric variation, which makes it a convenient measure when comparing SVs generated by variations of differing magnitudes because it is independent of the size of the parametric variation under consideration.

2.3 Analytical Investigations

Although the variational equation given by Eq. (2.2) cannot be solved analytically in general, in some cases it is amenable to closed-form solution. This section presents two specific cases where Eq. (2.2) can be solved exactly, highlighting important features generally present in SVFs.

The first example is a damped, driven linear harmonic oscillator, whose equation (non-dimensionalized) is expressed:

$$\ddot{x} + b\dot{x} + kx = \sin(t). \tag{2.6}$$

Once the system has settled onto the attractor, the dynamics are given by

$$x = \frac{1}{\sqrt{(k-1)+b}} \sin(t + \psi), \tag{2.7}$$

where ψ is a phase shift given by

$$\psi = \tan^{-1}(\frac{b}{k-1}). \tag{2.8}$$

The variational equation given by Eq. (2.2) in this specific case is

$$\frac{d}{dt}\delta\mathbf{x} = \begin{bmatrix} 0 & 1 \\ k & b \end{bmatrix} \delta\mathbf{x} + \begin{bmatrix} 0 \\ s(t) \end{bmatrix} \delta p, \tag{2.9}$$

where $s(t)$ depends on which parameter is varied. For example $s(t) = x$ if k is the varied parameter, while $s(t) = \dot{x}$ if b is the varied parameter. The general solution for a linear system in the form of Eq. (2.2) (if $\delta\mathbf{x}(0) = \mathbf{0}$) is

$$\delta\mathbf{x}(t) = \int_{t_0}^{t} e^{\mathbf{A}(t-\tau)}\mathbf{b}(\tau)\delta p d\tau. \tag{2.10}$$

Using this formula in conjunction with Eq. (2.9) provides an exact solution to the problem if we specify $t - t_0$ as the evolution time ΔT. The explicit expressions for the case of $s(t) = k$ or $s(t) = b$ are too unwieldy to be provided in full here, but some important features should be mentioned. First, solutions consist of two parts: an exponentially decaying transient component and a long-term steady-state component. If the evolution time ΔT is long enough, only the steady-state component will remain. This is because the varied system is being forced (due to its initial condition being on the nominal system's limit cycle) to trace a path transitioning from one limit cycle to another. Second, solutions to Eq. (2.10) for a variation in k or b will be similar but out of phase by $\frac{\pi}{4}$ just as the position and velocity given by Eq. (2.7) and its derivative will be out of phase by $\frac{\pi}{4}$. Finally, damping plays the role one would expect: underdamped systems will show a great deal of oscillatory behavior in their SVs over a range of evolution times, while overdamped systems will show very little.

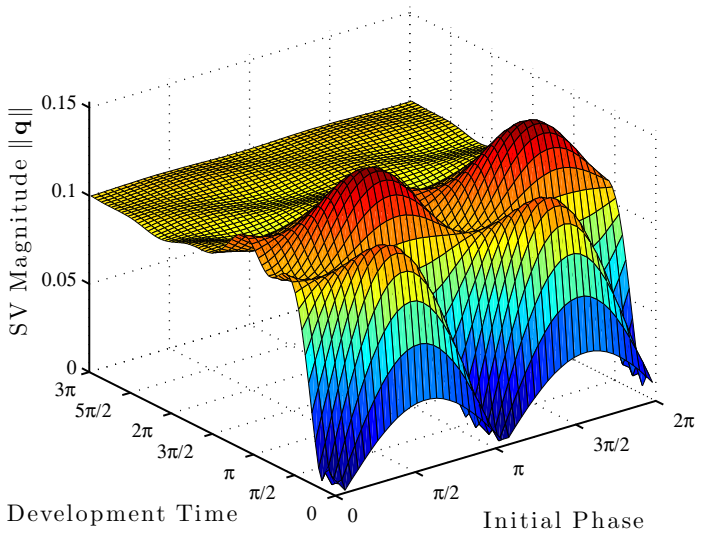

Figure 2.1: How SV magnitude varies with evolution time and initial phase for the damped, driven harmonic oscillator ($k = 4, b = 1$). Variation is in k.

Figure (2.1) illustrates typical variations in SV magnitude that occur as a function

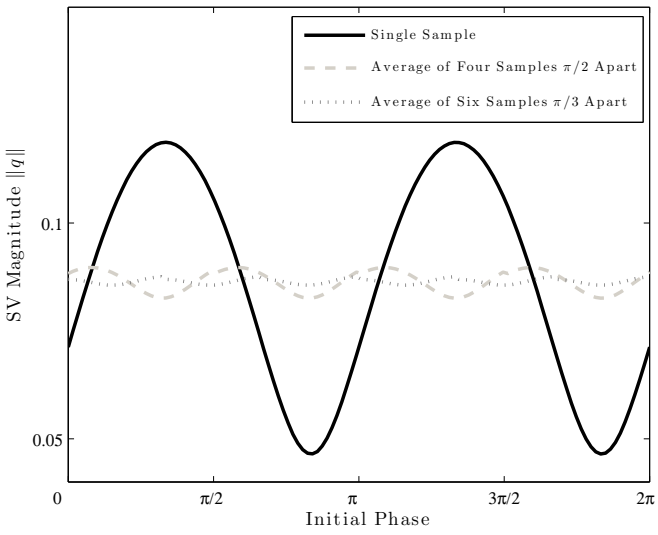

Figure 2.2: How average SV magnitude varies with number of samples around the attractor for the damped, driven harmonic oscillator ($k = 4, b = 1$). Variation is in k.

of initial phase ψ and evolution time ΔT. The phase ψ plays a critical role for short evolution times (here less than approximately π); for very short times there is nearly an order of magnitude difference between the lowest and highest sensitivity magnitudes based solely on initial phase. This is not an isolated case as similar results are seen for a range of different system parameters. If one wants to consider an average SV magnitude that is independent of the phase, sufficient sampling is necessary. Figure (2.2) shows average normalized SV magnitude as a function of initial phase for an evolution time that corresponds to 20% of the excitation period with different numbers of samples in the average. Here, six evenly spaced samples per cycle significantly reduce the phase dependent variation in average SV magnitude. Examining this figure and also turning back to Fig. (2.1), it is apparent that for optimal sensitivity a specific initial phase ψ and a specific evolution time ΔT will maximize the SV magnitude. This is typical of many systems.

As a second example of a dynamical system that can be solved exactly, consider the hybrid system recently proposed by Corron et al. [59]. This system combines a continuous dynamical system described by a differential equation with a map-like switching variable. The system's overall response is a hybrid of continuous and map-like dynamics. The system is described by

$$\ddot{u} - 2\beta\dot{u} + (\omega^2 + \beta^2)(u - s) = 0, \tag{2.11}$$

$$\text{when} \quad u(\tau) = 0 \quad \text{then} \quad s(\tau) = \text{sgn}(u(\tau)). \tag{2.12}$$

The solution of the system is given by

$$u(t) = s_n + (u_n - s_n)e^{\beta(t-n)}(\cos(\omega t) - \frac{\beta}{\omega}\sin(\omega t)), \tag{2.13}$$

$$\text{where} \quad u_{n+1} = e^{\beta}u_n - (e^{\beta} - 1)s_n \tag{2.14}$$

is the map that describes how u_n is transformed to u_{n+1}. Here the u_n correspond to the times when $\dot{u}(\tau) = 0$. Typically $\omega = 2\pi$ and $\beta < \log 2$. Again, the closed-form expressions that solve the variational equations are unwieldy, but can be used to obtain results such as those shown in Fig. (2.3). This system is chaotic, but it is apparent that, as in the case of the harmonic oscillator, there is an optimal initial state and evolution time which maximize the SV magnitude. Moreover, for the ensemble considered, there is a preferred evolution time for maximum SV magnitude that is independent of the exact initial condition within the ensemble. The average SV magnitude across the ensemble will be maximized for this evolution time of about 0.75s.

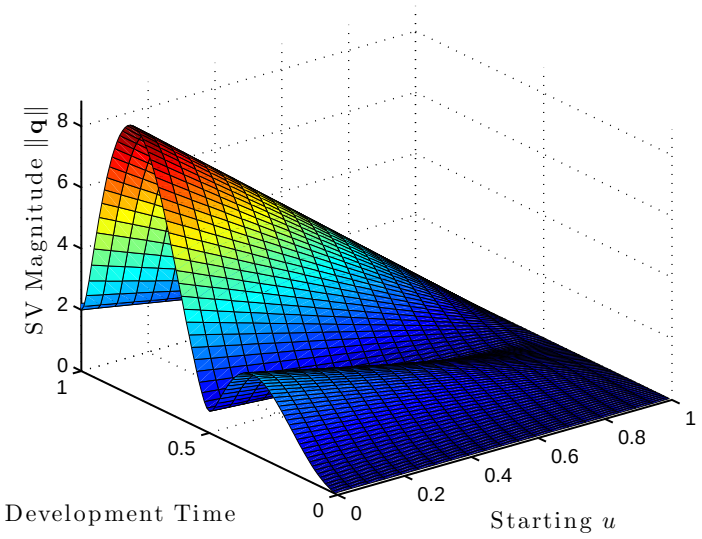

Figure 2.3: SV magnitude varies with evolution time for an ensemble of initial conditions $\dot{u} = 0, u > 0$ on the Corron system attractor.

2.4 Numerical Investigations

The analytical results above indicate there may be preferred combinations of system, initial condition, and evolution time for generating large magnitude SVs. This idea will be explored further in the context of systems that can only be integrated numerically. Specifically, the average SV magnitude generated over a large collection of initial states for a given attractor will be examined in an attempt to understand what occurs when the role of the initial condition is minimized. Towards these ends, consider the Duffing oscillator, a well known nonlinear dynamical system, which can be represented in non-dimensional form by the set of equations

$$\begin{aligned} \dot{x} &= y, \\ \dot{y} &= -x^3 - kx - by + A\sin z, \\ \dot{z} &= 1. \end{aligned} \tag{2.15}$$

Obviously, other non-dimensional forms are possible, but they will also be 3-dimensional dynamical systems with 3-dimensional parameter spaces and no generality is lost by selecting this form in particular. Integrating Eq. (2.15) in conjunction with the variational equation that corresponds to the parameter whose variation we would like to quantify allows SVFs to be constructed. For example, for the Duffing oscillator, if one considers k as the parameter to be varied in generating SVFs with A and b as controllable parameters that can be adjusted to change the dynamic regime but are otherwise treated as fixed with respect to any variations, we obtain the following variational equation

$$\begin{aligned} \dot{\delta x} &= \delta y, \\ \dot{\delta y} &= -3x^2\delta x - k\delta x - b\delta y + A\cos z\delta z - x, \\ \dot{\delta z} &= 0. \end{aligned} \tag{2.16}$$

Integrating the combined system of Eq. (2.15) and Eq. (2.16) for 500 cycles while generating SVs for 20 initial conditions within each cycle allows enough data to be gathered to arrive at a reasonable estimate of how SV magnitudes vary across the attractor, and for an estimate of the average SV magnitude for the attractor as a whole. For each initial condition, SVs are generated for evolution times ranging from 1% to 100% of a 2π period cycle, in increments of 1%.

As shown in the series of images in Fig. (2.4), which regions of the parameter space have the highest average SV magnitude is dependent on the selected evolution

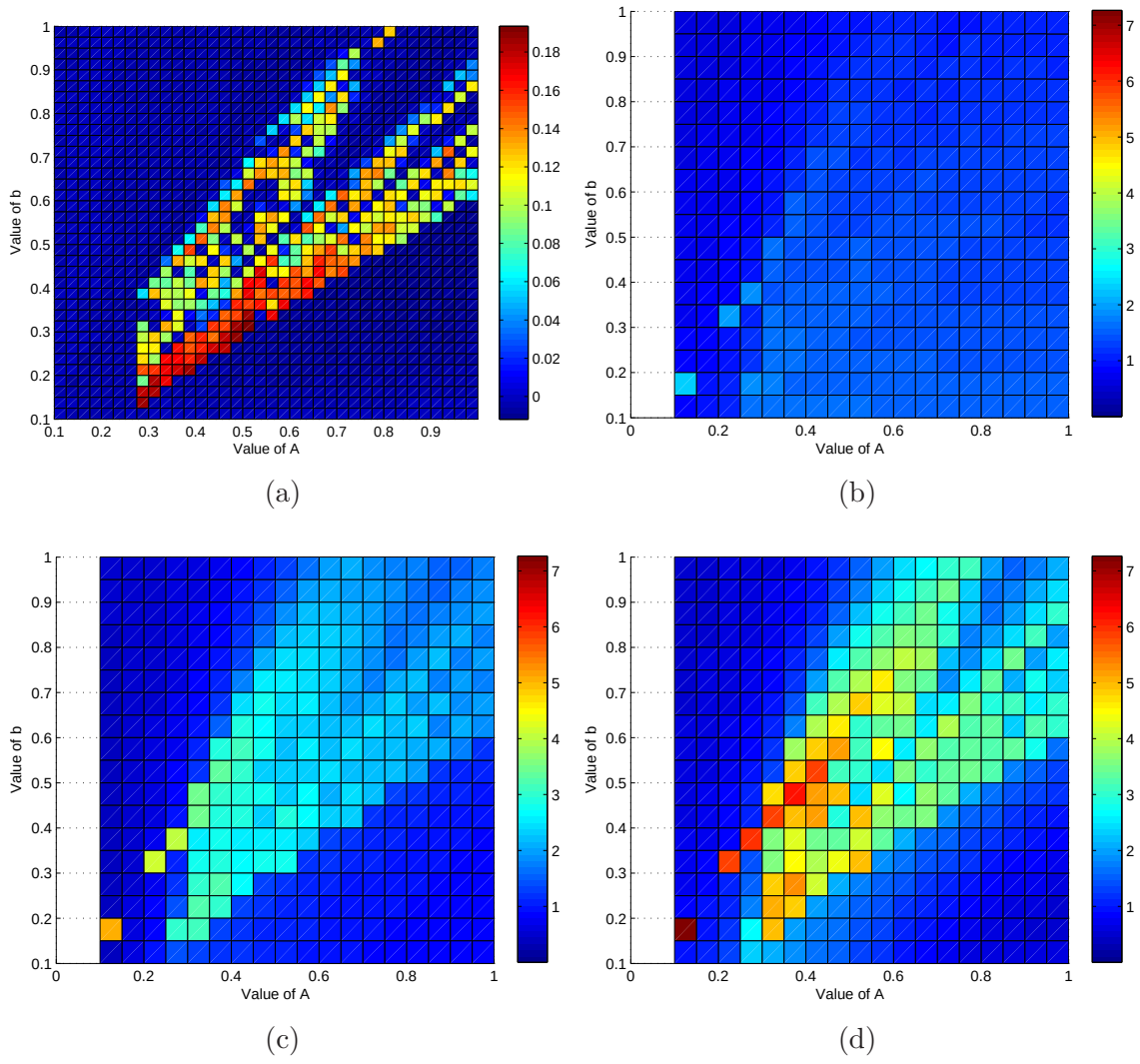

Figure 2.4: How average SV magnitude varies with the evolution time for different regions within the parameter space of the Duffing oscillator of Eq. (2.15). The subfigures are largest Lyapunov exponent (a Lyapunov exponent greater than zero indicates chaos) (a), average SV magnitude for 50% of a period (b), average SV magnitude for 75% of a period (c), and average SV magnitude for 100% of a period (d).

time ΔT. For short evolution times (times shorter than 50% of a period) both chaotic and non-chaotic regimes display very similar average SV magnitudes. However, for longer evolution times (times greater than 75% of a period) chaotic regimes, in general, generate higher average SV magnitudes. This suggests that if the linearity assumption inherent in the variational equation of Eq. (2.16) remains valid for evolution times greater than 75% of a period, it is likely to be advantageous to be in a chaotic regime in order to generate large magnitude (and therefore sensitive) SVs. Chaotic regimes have other advantages as well, such as sampling more of the state space and providing more opportunities for coincident initial conditions, as discussed in sections 2.5 and 2.6.

The SV magnitudes generated via the variational equation are, by definition, possible when the parameter variation is infinitesimal. However, whether those magnitudes remain possible when the variation is finite is a question that needs to be addressed. This question can be explored by comparing SVs generated in two different ways: via the system equations with varied parameters, and via the variational equations. One can assume that the validity of the variational equations has broken down if the SVs generated in each way disagree by a certain amount. This is done for Eq. (2.15) and Eq. (2.16), assuming that a 5% difference in their predicted SV endpoints indicates a breakdown of the assumed linearity of the variational equations. Examining the same regions of the parameter space for which SVs were generated previously, Fig. (2.5) shows the length of the evolution time for which the linear assumption remains valid for a 1% difference in k. The variational equations are valid for close to an entire period or more for most of the parameter space, although somewhat less where the dynamic regime is chaotic (refer to Fig. (2.4)).

For larger variations, the time the variational equations remain valid is shorter than for smaller variations, but for variations of equal magnitude chaotic regions will generally have shorter times of validity than non-chaotic regions.

Examining the distribution of SVs within a generated SVF for a given set of system parameters can also be insightful. Figure (2.6) shows the distribution for a chaotic regime of the Duffing oscillator when the evolution time is 50% of a period, and when it is 100% of a period. Figure (2.7) shows how such SVs are spatially distributed for ten Poincaré sections in the attractor at an evolution time of 100% of a period. Together, these figures show that in chaotic regimes, there are a small number of highly sensitivity SVs within a given SVF. This suggests that using some form of targeting control [60, 61] to stabilize orbits near these highly sensitive regions of the attractor might be an effective strategy for increasing SVF sensitivity.

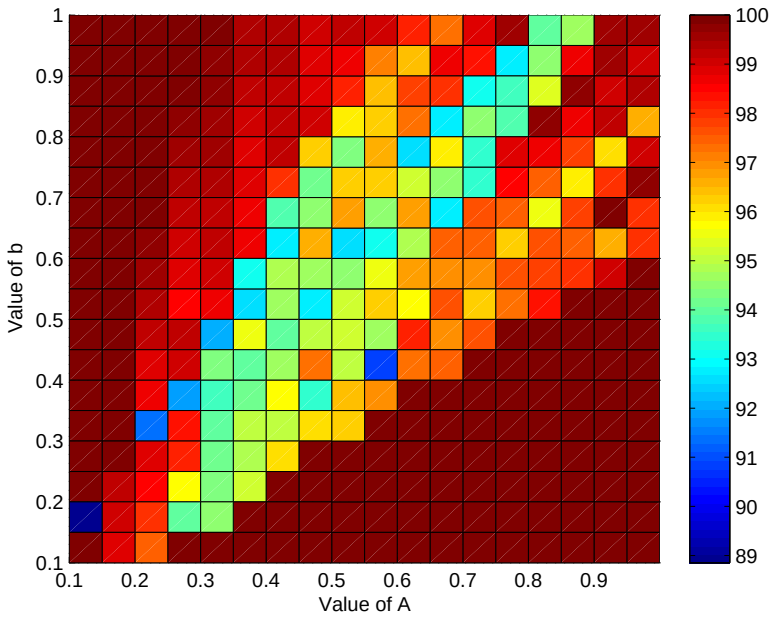

Figure 2.5: The length of time the linear variational equation assumption for SVs holds for a 1% variation in k. Here the assumption is considered broken when a 5% difference is observed between predictions of the system equations with varied parameters and the variational equations. 100% indicates the assumption holds for a period or longer.

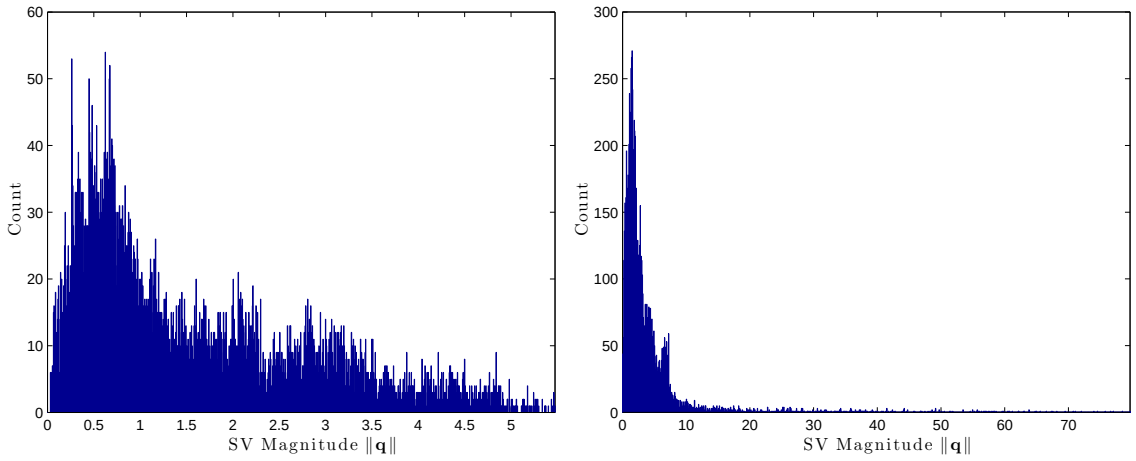

(a) (b)

Figure 2.6: How SV magnitudes are distributed for $10,000$ SVs in a SVF belonging to the Duffing oscillator of Eq. (2.15) with variation in k ($A = 0.4, b = 0.25$). The subfigures are for an ΔT of 50% of a period (a), and an ΔT of 100% of a period (b).

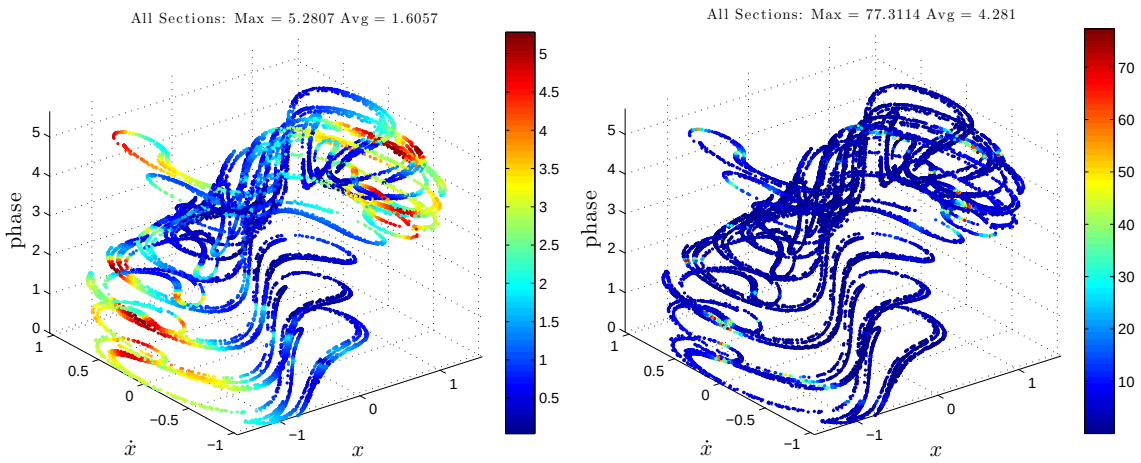

(a) (b)

Figure 2.7: How SV magnitudes are distributed within state space for a SVF belonging to the Duffing oscillator of Eq. (2.15) with variation in k ($A = 0.4, b = 0.25$). The subfigures are for an ΔT of 50% of a period (a), and an ΔT of 100% of a period (b).

2.5 Feedback Design

Sections 2.3 and 2.4 demonstrate that the nature of the dynamical system and the choices involved in how sensitivity vectors are sampled, including the evolution time ΔT and the chosen initial conditions, impact the average SV magnitude of a SVF. This naturally leads to the question: if one has the capability to modify a dynamical system, can the average SV magnitude be maximized through modification? In this section, it is shown that by changing a system through feedback, it is possible to augment a system's natural sensitivity. Consider again the damped, harmonic oscillator of Eq. (2.6). Choosing an appropriate feedback excitation $N(x, \dot{x}, t)$ in the equation

$$\ddot{x} + b\dot{x} + kx = N(x, \dot{x}, t) \ , \tag{2.17}$$

has the effect of changing the system and thereby the sensitivity of any generated SVs.

Feedback such as $N(x, \dot{x}, t)$ is typically subject to some constraints in a real physical system. Such constraints may include restrictions on the range of allowable system states (e.g. position or velocity) or limits on the magnitude of the inputs (e.g. the amount of force the feedback controller can output). In this work, such constraints are taken into account by considering a limit on the size of the attractor by penalizing attractors that are too big, or too small (SV magnitude is somewhat correlated with attractor size) and by limiting the magnitude of the applied forcing. With these

Table 2.1: High sensitivity parameter combinations for polynomial control

Set	k_c	α_c	A	b_c	Average SV Magnitude
1	-2.3	0.2	0.2	0	7.03
2	0	0	0.5	0	7.01
3	-1.3	0.05	0.4	0	6.95
4	0.35	-0.05	0.5	0	6.78
5	-2.1	0.15	0.2	0	6.61
6	-1.7	0.1	0.35	0	6.00

constraints, a question can be posed: what is the best form of feedback to generate a maximized SVF magnitude?

To establish a basis for answering this question, first consider an $N(x, \dot{x}, t)$ having the fixed form

$$N(x, \dot{x}, t) = b_c\dot{x} - k_c x - \alpha_c x^3 + A \sin t \ , \tag{2.18}$$

where the parameters having subscripts c are considered control parameters.

A pattern search method, where each of the control parameters is tuned sequentially while the others are regarded as fixed, can be used to seek dynamic regimes that will maximize average SV magnitude. The reason for adopting such an approach is to avoid discontinuities in the parameter space caused by bifurcations that gradient-based algorithms have difficulty handling. Consider one instance of these optimizations as an illustration. For a system having $b = 0.1$ and $k = 1$, a maximum force constraint of 3, and no size penalty for attractors with position and velocity between 1 and 5, the controller in Eq. (2.18) is optimized by adjusting the parameters (A, b_c, k_c, α_c) in increments of either 0.05 or 0.025. Possible initial values of A belong to the set $[0.1, 0.5]$, those of b_c to the set $[0, 1]$, and those of α_c to the set $[0, 1]$. The value of k_c is left un-initialized because it will always be adjusted first by this particular algorithm. One hundred and fifty different initial parameter combinations were considered. After several cycles of parameter adjustment, the parameter sets resulting in the highest magnitude SV average are as given in Table 2.1. Limit cycles dominate the results for this controller, and particularly prominent among the results are parameter combinations that have $k_c = -2.1$ or $k_c = -1.7$.

Having a controller of fixed polynomial form, especially one with a relatively low number of terms, greatly reduces the possible distributions of feedback force across the state space. For this reason, feedback based on control points distributed

throughout the state space and that can be interpolated with splines to arrive at an overall feedback law was also considered. This arrangement allows a feedback force distribution that can take on a much wider variety of configurations than one based on a small number of polynomial terms alone. Consider the case where

$$N(x, \dot{x}, t) = R(x, \dot{x}) + A \sin \omega t \ , \tag{2.19}$$

with $R(x, \dot{x})$ given by a spline surface of forces distributed over the state space.

Here the form of $R(x, \dot{x})$ can be optimized by adjusting the force values at certain control points. The number and position of the control points will thus play an important role in the feedback description. For this investigation, a force surface which is required to be symmetric about the origin and which has a total of twelve equally-spaced control points is considered. The harmonic excitation is taken to have fixed parameters. SVs are sampled four times each excitation period, each SV taken after an evolution time of 50% of a period. These conditions match those for the earlier optimization using the controller that has polynomial terms in Eq. (2.18).

For the system having the same constraints as for the pattern search but with its feedback of the form given by Eq. (2.19), greater SV magnitudes are observed. By initializing the spline surface over many different random initial surfaces that are symmetric about the $x - \dot{x}$ line and optimizing, an average SV magnitude of 11.06 can be arrived at for the system shown in Figures 2.8 and 2.9. Here the attractor is shown as the thickened black line superimposed on the spline surface.

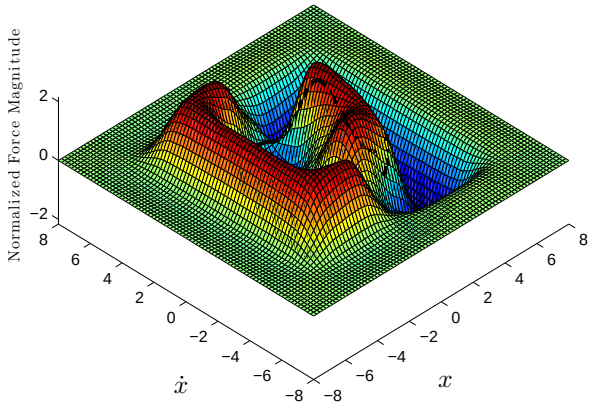

Figure 2.8: High sensitivity spline force surface generated using 12 control points and symmetry: angled view.

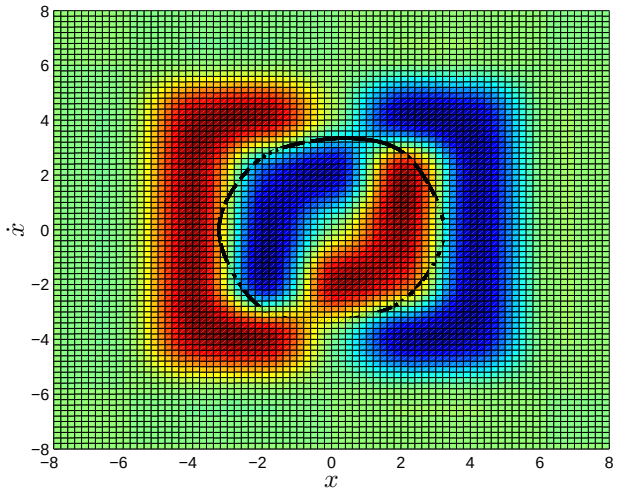

Figure 2.9: High sensitivity spline force surface generated using 12 control points and symmetry: top view.

This specific example is not an isolated case of higher sensitivity. When using spline force surfaces for feedback, almost all the initial parameter sets that were optimized resulted in higher sensitivities than in the case of the polynomial-based controller. Part of this comparison is skewed since the polynomial-based controller has fewer adjustable parameters to begin with. Nonetheless, in examining the topology of the optimized spline force surfaces, it seems clear that this type of feedback surface would be difficult to construct with a small number of polynomial terms. When the constraint requiring the symmetry of the force surface is removed, even larger magnitude SVs can be generated. Table 2.2 shows the values of the three highest sensitivity regimes for a non-symmetric controller.

Table 2.2: High sensitivity results for non-symmetric spline surfaces

Set	Average SV Magnitude
1	17.31
2	15.71
3	15.32

The results in Table 2.2 are somewhat expected, since giving the optimizer more freedom in the parameter space should result in improved solutions. However, they do highlight how significantly the assumed form of the controller can impact the ability to arrive at high sensitivity regimes. Using a larger number of control points was

also considered to determine whether increasing the number of points could lead to improvements in sensitivity. When the number of points was doubled for the case of the symmetric controller, this did not always lead to significantly improved average SV magnitudes; however, in the case of greatest improvement the sensitivity roughly doubled. Thus, a more varied or "wavy" surface can sometimes yield higher average SV magnitudes.

Now, let us revisit controllers of fixed form when more freedom is allowed in the values of the parameters. Consider an $N(x, \dot{x}, t)$ having the form

$$N(x, \dot{x}, t) = b_c\dot{x} - k_c x - \beta_c x^2 + \alpha_c x^3 + A \sin t \ , \tag{2.20}$$

where, again, the parameters having the subscripts c are considered control parameters. This time, however, the search methodology is a genetic search and the control parameters are not restricted to a certain set of values but can range over all of the real numbers within the constraints. Here one hundred different genetic searches for $b = 0.1$ and $k = 0.8$, were performed, beginning with randomized initial parameters. The solutions were allowed to evolve over 100 generations using the standard parameter settings within MATLAB's genetic search algorithm. This kind of search resulted in even higher average SV magnitude SVFs as Table 2.3 indicates.

Table 2.3: High sensitivity results for a fixed-form genetic search

Set	Average SV Magnitude
1	56.2
2	55.7
3	53.4

What is most interesting about the genetic search results is that they indicate that fragile attractors are oftentimes the most sensitive. Here fragile is used to denote attractors that are close to a bifurcation, either because they exist in a periodic window, at the edge of chaos [62], or near some other type of bifurcation. A small fluctuation in the k_c value (and sometimes in other parameter values as well) will result in the attractor changing form. Figure 2.10 shows an example of this phenomenon. That SVFs should be most sensitive near bifurcations makes sense; obviously an attractor that deforms a great deal should provide a sensitive SVF. How closely a system should be positioned with respect to the bifurcation boundary then depends

on the levels of the parameter variations expected and the level of noise or hysteresis that could impact the attractor's structural stability.

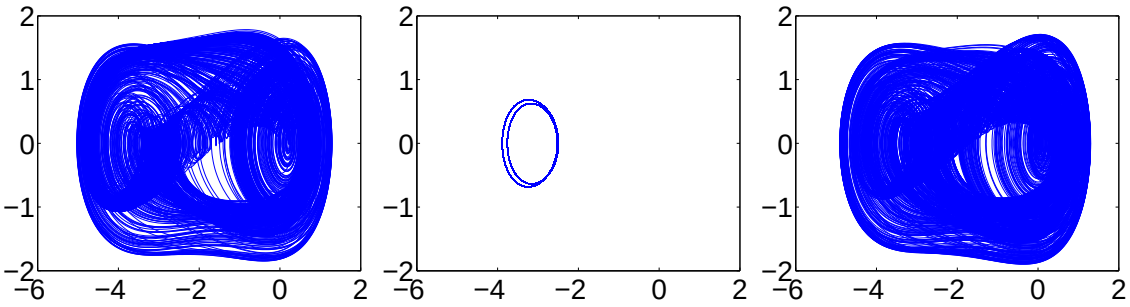

Figure 2.10: Bifurcations of a fixed-form feedback control found using a genetic search algorithm. The nominal control parameters are $[A\ b_c\ k_c\ \beta_c\ \alpha_c] = [0.6716\ 0.0902\ 0.2660\ 0.6847\ 0.1076]$. The subfigures are $k_c = 0.2560$ (a), $k_c = 0.2660$ (b), and $k_c = 0.2760$ (c).

2.6 Feedback When Coincidence is Required

The results in Section 2.5 show that implementing a controller of fixed form and then optimizing its parameters or creating a synthetic force surface by controlling the values of a set points on a grid throughout the state space can both be used to alter a dynamical system to increase average SV magnitude. However, performing this type of optimization in a completely theoretical sense can be misleading because we still need to enforce $\delta\mathbf{x}(t_0) = \mathbf{0}$ in Eq. (2.2) in any real system in order to generate SVs. One way to do this is to generate discrete data for a dynamical system under its nominal parameters along with data for some set of variations and then construct SVs using local modeling such as point cloud averaging (PCA) [31]. By examining what regions of the attractor are accessible for SV generation, one can determine if and when feedback control will be effective.

Reconsider the Duffing system given by Eq. (2.15). If one makes use of the parameter space used in the previous numerical analysis (see Section 2.4), where A and b are considered adjustable, but is now concerned with whether or not nearly coincident initial conditions can be generated, the results in Fig. (2.11) are obtained in comparison to those of Fig. (2.4). Here a 1% variation in the value of k is being captured using an embedded coordinate system (see Chapter 3), where x is embedded 3-dimensionally.

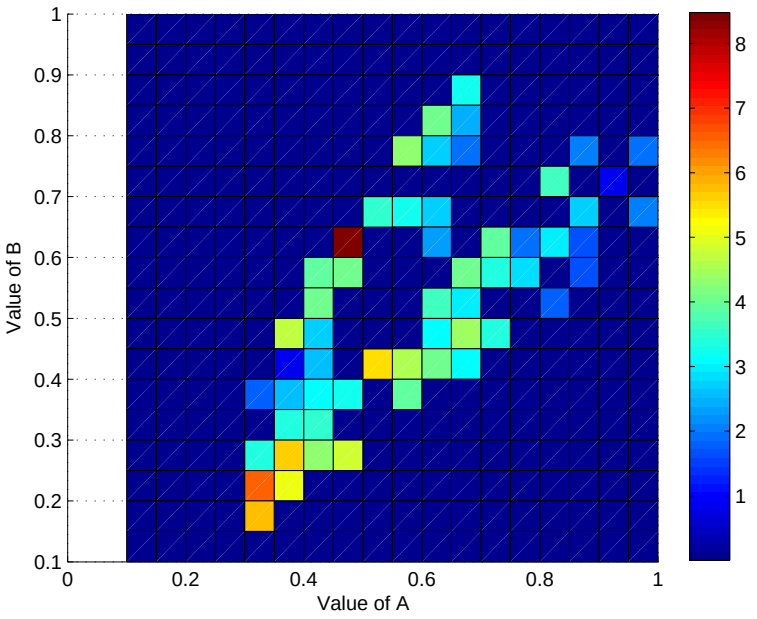

Figure 2.11: Average SV magnitude over the parameter space for the Duffing oscillator of Eq. (2.15) reconstructed using discrete data sets and local modeling.

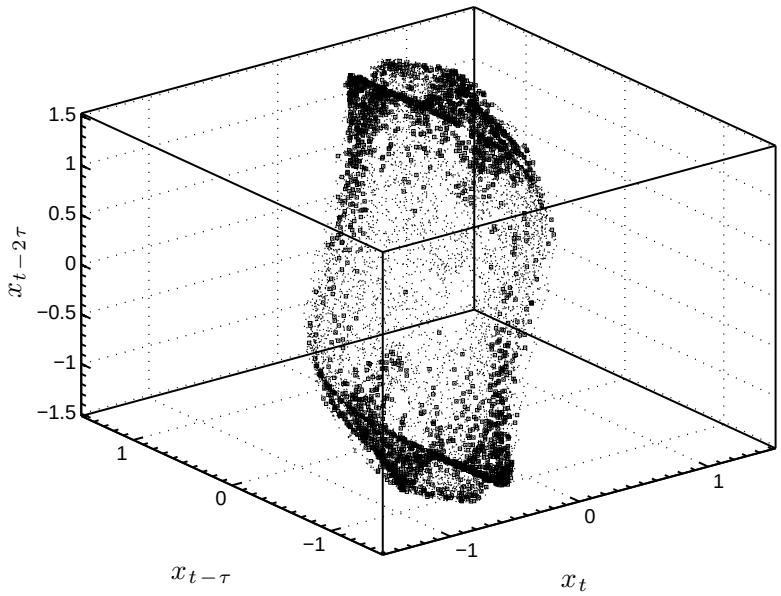

Figure 2.12: Initial conditions used in generating SVs via PCA for variations in k ($A = 0.4, b = 0.25$). Darker points indicate initial conditions from which SVs could be constructed.

Apart from the average SV values being somewhat different, this figure illustrates that in many cases limit cycles may not be accessible via a PCA approach because there may be no or few initial conditions on the nominal and varied attractors that are close enough to being coincident to generate meaningful results. Attempts at local modeling in these cases will produce unreasonably large model coefficients and estimated parametric variations will be prone to error. Many of the zero or near zero SV magnitudes in Fig. (2.11) result from an inability to construct SVs using local modeling because the nominal attractor is a limit cycle. However, inability to generate SVs can also occur when the system undergoes a bifurcation from a chaotic attractor to a limit cycle over the range of the parametric variations of interest. Thus, it is advantageous to be in a chaotic regime when using discrete data to construct SVs, as chaos ensures that more of the state space is sampled, despite attractor deformations. Any sensitivity optimization in a physical system should therefore be initialized in a chaotic regime. Figure (2.12) shows an example of which of the discrete initial conditions can be used to successfully generate SVs via local modeling for the Duffing system when the dynamics are chaotic.

2.7 Conclusions

This paper has presented analytic and numerical investigations into factors that influence the generation of SVFs, specifically considering the roles the dynamic regime and evolution time play in influencing SVF sensitivity. It also presented two methods for altering a system via feedback to increase sensitivity: an optimized controller of fixed form, and a feedback force surface generated using control points and interpolation. The results suggest that attractors near bifurcation points generate the most sensitive SVFs, but that it may be difficult to realize this high sensitivity in physical systems if the nominal and deformed attractors do not overlap. For this reason, beginning in a chaotic regime and using feedback to position a system near the edge of chaos is likely to provide optimal sensitivity.

CHAPTER 3

Sensitivity Vector Fields in Embedded Coordinates

3.1 Introduction

Change in the dynamic response of a system indicates that its parameters have changed in some way. Thus, by monitoring a system's dynamic response it is often possible to identify and characterize any parametric variations the system undergoes. Knowing about parametric variations can be valuable in diagnostic or sensing applications, particularly when identifying incipient changes is paramount, as it is in cases of damage detection.

Vibration-based modal methods [2] have been the traditional means of identifying parametric variations via the dynamic response. These methods rely on relating measured changes in modal parameters, such as resonant frequencies or mode shapes, to underlying variations in the parameters. Frequently employed in mechanical systems, modal methods are the basis of both dynamic atomic force microscopy (dAFM) and micro-cantilever based sensing. For these systems, accurate measurements of frequency shifts of vibrating microcantilevers are the basis of successful devices [63, 64, 15]. Continued efforts to improve these and related technologies attest to the general effectiveness of modal methods.

Under certain circumstances, however, modal methods can be less effective. For example, when a system is significantly nonlinear, when it has a low quality factor, or when multiple simultaneous parametric variations need to be distinguished from one another, other methods may be preferable. A specific alternative championed here is based on sensitivity vector fields (SVFs) [32, 58, 31], which quantify how dynamical system attractors deform under parametric variations. Because a SVF consists of a field of vectors distributed in state space, it can be successful even when a frequency-shift method would fail. To date, SVFs have been used in conjunction

with a variety of dynamical systems [34] and proven to be an effective method of identifying parametric variations. Carefully designed nonlinear feedback can further adjust a system's sensitivity to the parametric variations of interest.

Although SVFs have been successfully employed in conjunction with data from both simulations and experiments [35], previous SVF research has been limited to systems where a full set of state variables is accessible. In all but the simplest real systems, this kind of complete access is impossible. For some systems, measuring certain dynamical variables may be difficult. For others, it may be cost prohibitive to measure the full state because the system has a large dimension. For these kinds of systems, it is typical to have records of only a few state variables in the form of one or more time series, a time series being a sequence of scalar data points measured at successive times. So long as the system has a low-dimensional attractor, further analysis is feasible. Previous research concerned with methods of reconstructing dynamical system attractors when only time series data are available has shown reconstruction is possible using an embedding. The most common form is a time-delay coordinate embedding, in which the embedded vectors are composed of individual time series observations separated by a fixed delay time. The mathematical basis of time-delay coordinate embedding has been rigorously established [37, 38, 39, 40] and several texts [41, 42] illustrate methods for performing such reconstructions.

The focus of this work is creating SVFs within the reconstructed state space established by a time-delay coordinate embedding of time series data. Specifically, for an initial condition in the reconstructed space, it is necessary to determine two future embedded states: one for the system retaining the nominal set of parameters, and a second for the system having some parametric variation(s). The difference between these two future states is defined as an embedded sensitivity vector (eSV). A collection of eSVs across the entire attractor is an embedded sensitivity vector field (eSVF). Thus, the fundamental problem involved in constructing eSVFs is one of prediction. Making predictions using embedded nonlinear time series is an established research area, and we draw on the previous body of work [65, 66, 67, 68]. Typically, we choose initial conditions that are on the nominal attractor so that only the future state of the varied system needs to be predicted. Making a good prediction then requires gathering neighborhoods of states for the varied system surrounding a given initial condition belonging to the nominal system and constructing local models to fit these neighborhoods. Once an eSV is estimated, it must be validated to ensure its accuracy. This is accomplished by requiring accurate predictions of near-neighbor surrogates, checking local modeling coefficients, and ensuring the correct linearity and

proportionality of eSVs that are generated by known parametric variations of different magnitudes. A method of quantifying the error in eSV predictions based on local modeling is outlined for cases where the equations of motion for the system are known. Applications of the methodology to various simulated time series, including series for a Duffing oscillator and for the Lorenz attractor demonstrate the effectiveness of the technique. These systems are also used to explore how additive noise influences the results. Further application to experimental time series generated by a Chua's oscillator and a cantilever beam demonstrate how the methodology can be applied to real, physical systems.

3.2 Embedded Sensitivity Vector Fields

3.2.1 SVF Definition

A SVF is a collection of vectors that capture how a dynamical system attractor deforms as a result of a given parametric variation. The individual SVs making up a SVF are constructed by sampling trajectories of nominal and varied systems as they diverge over time. Two trajectories that are initially coincident in state space but differ by some parametric variation will evolve differently. By sampling these trajectories a time ΔT after their coincidence, a SV is generated that connects the sampled point on the nominal attractor to the sampled point on the varied attractor. This vector quantifies the divergence of the two trajectories. It depends on the underlying dynamical system, the nature of the parametric variation, and the evolution time ΔT. For short ΔT, the SV will be proportional to the parametric variation. Thus, by obtaining SVFs corresponding to several known parametric variations, a set of basis vectors can be constructed against which further unknown parametric variations can be compared, allowing them to be identified.

More mathematically, consider a dynamical system described by the flow $\dot{\mathbf{x}} = \mathbf{f}(\mathbf{x}, p, t)$, where $\mathbf{x}$ is the state vector, and p is a system parameter that can vary. Using a Taylor series to develop a variational equation about the nominal trajectory $\mathbf{x}(t) = \mathbf{x}_o(t)$ and nominal parameter value $p = p_o$ and retaining only the linear terms results in

$$\dot{\delta\mathbf{x}}(t) = \mathbf{A}(t)\delta\mathbf{x}(t) + \mathbf{b}(t)\delta p \ , \tag{3.1}$$

$$\text{where} \qquad \mathbf{A}(t) = \left.\frac{\partial \mathbf{f}}{\partial \mathbf{x}}(t)\right|_{\substack{\mathbf{x}=\mathbf{x}_o \\ p=p_o}} , \tag{3.2}$$

$$\text{and} \qquad \mathbf{b}(t) = \frac{\partial \mathbf{f}}{\partial p}(t)\bigg|_{\substack{\mathbf{x}=\mathbf{x}_o \\ p=p_o}}. \tag{3.3}$$

Here, the state variation (from the nominal trajectory) is represented by $\delta\mathbf{x}$ and the parameter variation (from the nominal parameter value) is represented by δp. If Eq. (3.1) is integrated over the evolution time ΔT, the result is an equivalent map

$$\delta\mathbf{x}(t + \Delta T) = \Phi(t + \Delta T, t)\delta\mathbf{x}(t) + \mathbf{q}(t + \Delta T)\delta p, \tag{3.4}$$

where the state transition matrix for the dynamical system Φ, depends only on $\mathbf{A}(t)$. Trajectory divergence, expressed in the state variation $\delta\mathbf{x}(t+\Delta T)$ that develops over the evolution time Δt, can be interpreted as the sensitivity vector $\mathbf{q}(t+\Delta T)\delta p$ when $\delta\mathbf{x}(t) = \mathbf{0}$ at the initial time (that is, if the trajectories are truly initially coincident at time t). In general, $\mathbf{q}$ will depend on both $\mathbf{A}(t)$ and $\mathbf{b}(t)$. The linearity of Eq. (3.4) highlights the fact that a specific parametric variation will elicit a proportional change in the generated SVF. This proportionality is what enables quantification of parametric variations through the comparison of newly generated SVFs to known, reference SVFs.

3.2.2 eSVF Definition

Consider again the flow $\dot{\mathbf{x}} = \mathbf{f}(\mathbf{x}, p, t)$, where the state is given by $\mathbf{x} = [x_1\ x_2 \ldots x_n]^T$, with n being the dimension of the system. In its simplest form, performing a time-delay coordinate embedding of the flow involves sampling a single state component and then constructing time-delay coordinate vectors having the form

$$\mathbf{s}(t) = [x_*(t)\ x_*(t-\tau) \ldots x_*(t-m\tau)]^T, \tag{3.5}$$

where $*$ indicates a single state of the system (from the total of n states), τ is the delay time, and m is the number of time-delay coordinates. It has been proven [40] that $m \geq 2d_A$ is a sufficient condition to reconstruct an attractor of dimension d_A, although the necessary dimension may be less. In this time-delay coordinate embedding space, the definition of an eSVF is similar to that of a SVF in ordinary state space, but what is measured is time-delay coordinate variation $\delta\mathbf{s}$ rather than state variation $\delta\mathbf{x}$. Time-delay coordinate variation is variation solely in the component of the state x_* selected for constructing the time-delay coordinate vectors. Figure 3.1 shows the flow and its variation for a two dimensional embedding in x_*, illustrating graphically

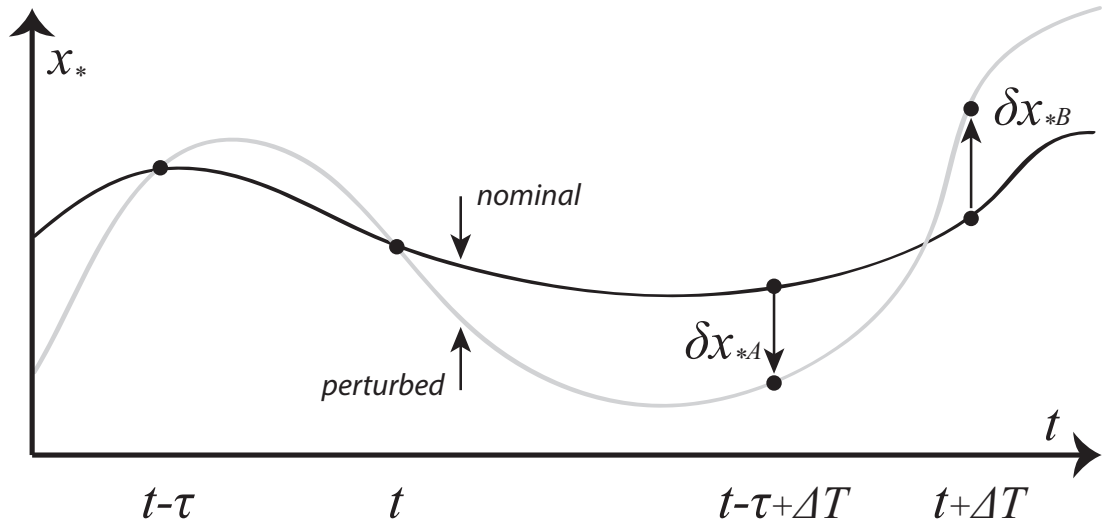

Figure 3.1: Consider a flow with two state variables x_1 and x_2 embedded two dimensionally in x_*. This figure illustrates the required initial coincidence of the nominal and varied trajectories, and the variations δx_* at later times which comprise an eSV.

how the time-delay coordinate variation has the general form

$$\delta\mathbf{s}(t+\Delta T) = [\delta x_*(t+\Delta T)\delta x_*(t-\tau+\Delta T)\ldots\delta x_*(t-m\tau+\Delta T)]^T. \tag{3.6}$$

In the embedding space, time-delay coordinate vectors are guaranteed to have a map of the form $\mathbf{s}(t+\Delta T) = \mathbf{H}(\mathbf{s}(t))$, where $\mathbf{H}$ depends on ΔT (which we assume is some multiple of τ) and p. This means we can define an eSV $\mathbf{q}_*\delta p$ as

$$\delta\mathbf{s}(t+\Delta T) = \frac{\partial\mathbf{H}}{\partial\mathbf{s}}(t+\Delta T,t)\bigg|_{\substack{\mathbf{s}=\mathbf{s}_o\\p=p_o}}\delta s(t) + \mathbf{q}_*(t+\Delta T)\delta p, \tag{3.7}$$

$$\text{where}\qquad \mathbf{q}_*(t+\Delta T) = \frac{\partial\mathbf{H}}{\partial p}(t+\Delta T,t)\bigg|_{\substack{\mathbf{s}=\mathbf{s}_o\\p=p_o}}. \tag{3.8}$$

Note that one can numerically compute the eSVs using Eq. (3.4) when the state space and the time-delay embedding space have the same dimension *and* the equations for the original flow $\dot{\mathbf{x}} = \mathbf{f}(\mathbf{x},p,t)$ are available. This idea is further developed in Section 3.3.5 in the context of eSV validation.

In practical cases, one is unlikely to know the function $\mathbf{H}$, and must rely on some form of modeling to generate eSVs. The natural choice is to use local modeling, where neighborhoods of states are collected that serve as analogues for the initial conditions of interest. The future images of these states, used in conjunction with the local

modeling, allow unknown trajectories to be predicted.

3.3 Methodology

There are four steps to generate an eSV for a given initial condition drawn from the nominal system's data set, namely:

1. Gather a neighborhood of nearby states from the varied system's data set.

2. Adjust the size of the neighborhood to optimize its accuracy in making predictions.

3. Use local modeling in conjunction with the resized neighborhood to make a prediction of the varied system's trajectory beginning at the given initial condition.

4. Take the difference between the varied trajectory (predicted by local modeling) and the nominal trajectory (known) in order to construct an eSV.

This process of eSV construction is illustrated in Fig. 3.2.

Once eSVs have been constructed, they are validated. There are three steps in this validation, namely:

1. Rank eSV neighborhoods based on the distance between the initial condition and the nearest state of the varied system along with the error in predicting that state's future trajectory.

2. Examine the coefficients resulting from the local modeling used to generate a given eSV and discard those eSVs whose coefficients are poor. For example, discard all neighborhoods when any coefficients are larger than 1.

3. If the eSVs are being used to build up basis vectors for future testing (and hence have known parametric variations), check their colinearity and proportionality in conjunction with the eSVs of other calibration sets.

This process of eSV validation is also illustrated in Fig. 3.2.

Below some important details regarding both the eSV construction process and the eSV validation process are provided.

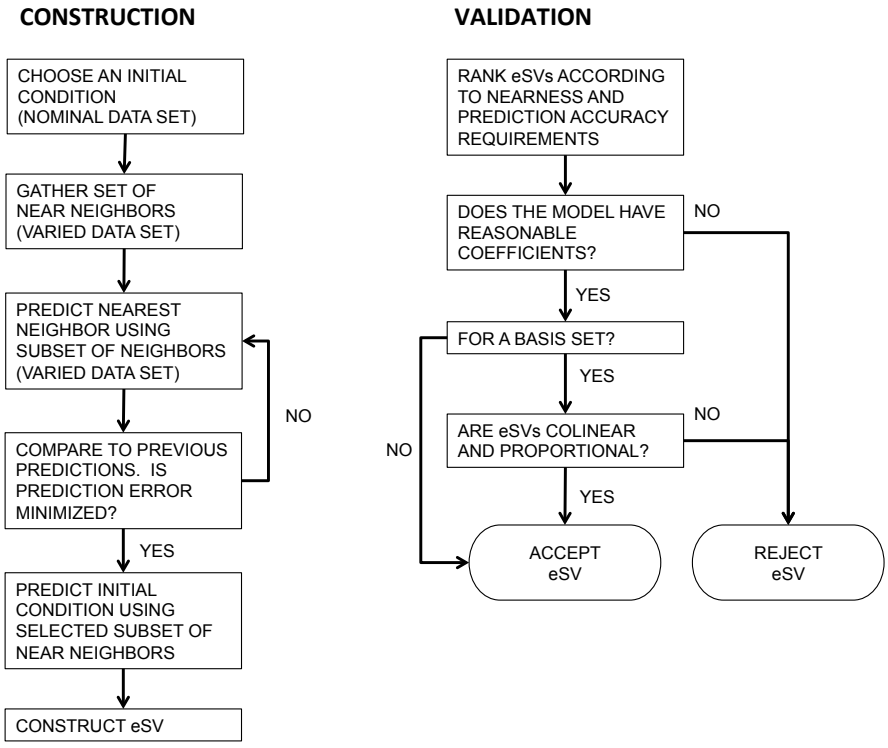

Figure 3.2: The process of generating and validating eSVs that are suitable for analyzing parametric variations.

3.3.1 Local Modeling using ePCA

The question of how to effectively predict nonlinear time series using local models has been studied by several authors [65, 67, 68]. Global approaches for nonlinear time series prediction have also been proposed, including methods based on radial basis functions [66]. However, global methods are more difficult to implement and less likely to give accurate results. Thus, our focus is constructing eSVs using local models exclusively, specifically using embedded point cloud averaging (ePCA) (similar to the original PCA [31]).

For an initial condition on the nominal attractor, ePCA involves solving an underdetermined problem involving the neighboring embedded states from the varied data set given by

$$\begin{bmatrix} 1 \\ \mathbf{x}^t_{k,\text{center}} \end{bmatrix}_{m+1\times 1} = \mathbf{X}^t_k \alpha \ , \tag{3.9}$$

$$\text{with} \qquad \alpha = \begin{bmatrix} \alpha_1 & \dots & \alpha_n \end{bmatrix}^T , \tag{3.10}$$

$$\text{and} \qquad \mathbf{X}^t_k = \begin{bmatrix} 1 & 1 & \dots & 1 \\ \mathbf{x}^t_1 & \mathbf{x}^t_2 & \dots & \mathbf{x}^t_n \end{bmatrix}_{m+1\times n} . \tag{3.11}$$

Here $\mathbf{x}^t_{k,\text{center}}$ is an initial condition of interest on the nominal attractor (i.e. the center of neighborhood k at time t), and α is a vector of unknowns. $\mathbf{X}^t_k$ holds the n embedded states from the varied data set in neighborhood k, and m is the embedding dimension. This is the original PCA formulation [31]. For ePCA, we enforce the additional condition that

$$\sum_{i=1}^{n} \alpha_i x^t_{i,r} x^t_{i,s} = x^t_{\text{center},r} x^t_{\text{center},s}, \forall\ r,s = 1,\dots,m \tag{3.12}$$

where $x^t_{i,s}$ refers to the s-th component of the measured embedded state $\mathbf{x}^t_i$. Solving Eqs. (3.9) and (3.12) together in the least-norm sense determines the weights each measured embedded state should be given so that their weighted average matches the initial condition as closely as possible while also minimizing quadratic cross terms.

Minimizing the terms in Eq. (3.12) minimizes the second order terms in the Taylor series expansion Eq. (3.7). This is important and can improve eSV accuracy. A (future) prediction at time $t+\Delta T$ can then be made using the previously determined α by calculating

$$\mathbf{x}^{t+\Delta T}_{k,\text{center}} = \mathbf{X}^{t+\Delta T}_k \ \alpha, \tag{3.13}$$

$$\text{with} \qquad \mathbf{X}^{t+\Delta T}_k = \begin{bmatrix} \mathbf{x}^{t+\Delta T}_1 & \mathbf{x}^{t+\Delta T}_2 & \dots & \mathbf{x}^{t+\Delta T}_n \end{bmatrix} . \tag{3.14}$$

Here $\mathbf{X}_k^{t+\Delta T}$ holds (future) states that correspond to the embedded states in the initial neighborhood k at time $t + \Delta T$. The eSV $\mathbf{q}$ is given by the difference between future points on the nominal and varied trajectories, i.e. the known nominal system trajectory known and the varied system trajectory predicted by the model. That is

$$\mathbf{q} = \delta\mathbf{x} = \mathbf{y}_{k,\text{center}}^{t+\Delta T} - \mathbf{x}_{k,\text{center}}^{t+\Delta T} \tag{3.15}$$

where $\mathbf{y}_{k,\text{center}}^{t+\Delta T}$ is the predicted embedded future state of the varied system and $\mathbf{x}_{k,\text{center}}^{t+\Delta T}$ is the known embedded future state of the nominal system.

More typical linear (first-order) approximations found in the literature [68] have the form

$$[\mathbf{X}_k^{t+\Delta T}]^T = [\mathbf{X}_k^t]^T\beta + \epsilon, \tag{3.16}$$

$$\text{with} \qquad \beta = \begin{bmatrix} \beta_{1,1} & \dots & \beta_{1,m} \\ \vdots & \vdots & \vdots \\ \beta_{m,1} & \dots & \beta_{m,n} \end{bmatrix}. \tag{3.17}$$

Here, β is, in general, a collection of vectors of unknowns, and ϵ represents error terms. Solving this overdetermined system for β in the least-squares sense, and then using the β vector in conjunction with an initial state allows computation of a predicted (future) state at $t+\Delta T$. Using this general framework, more accurate predictions may be possible by using higher-order models [69], but these quickly require a large number of neighborhood points, as the required coefficients increase as $m(s+m)!/s!m!$, where m is the embedding dimension and s is the order of the model. Related methods with additional complexities such as filtering [70] or methods which avoid a least-squares solution [71] have also been proposed.

The primary advantage of ePCA over these other methods is that the α vector provides a metric that can be used to judge the relative contribution of each neighborhood point in constructing eSVs. Different magnitudes in the α entries can indicate a poor neighborhood that will generate an inaccurate eSV.

3.3.2 Neighborhood Sizing

Once a neighborhood of nearby states from the varied system's data set have been gathered, the closest of these states is sequestered as a surrogate for the initial condition. Predictions are made for this surrogate using local modeling in conjunction with neighborhoods of various sizes to determine what neighborhood size to use when making a prediction from the actual initial condition. Because we know the future

(embedded) state of the surrogate, it is easy to determine what neighborhood size results in the most accurate prediction of its future trajectory.

This optimal neighborhood sizing capability is incorporated into the algorithm in two different ways. The first is suitable for cases where there are a large number of measured embedded states. Using the points closest to the initial condition, one can set up a series of increasing radii around the initial condition and consider the accuracy of predictions based on the neighborhood of embedded states contained within each radii. The radius with the lowest prediction error is selected for making predictions from the actual initial condition. The second way, appropriate when data are sparser, eschews the need for radii and simply drops the embedded state furthest from the initial condition in making consecutive predictions. One again chooses the neighborhood that results in the minimum prediction error.

3.3.3 Validation

To avoid regions of the state space giving poor eSVs, one can calculate the distance between the surrogate embedded states and the initial condition of interest. Then, one can rank eSV generating neighborhoods according to the product of this distance and the prediction error. Thus, close surrogate embedded states with good predictions are highly ranked whereas neighborhoods with surrogates that are distant or poorly predicted are not. This helps to avoid neighborhoods with especially bad predictions or disparate state space structure.

When the state space is highly structured, as is the case for many chaotic attractors, an initial condition that lies on the attractor of the nominal data set likely will not lie on the attractor of the varied data set. This occurs, for instance, when the parametric variation is large enough to significantly deform the varied attractor with respect to the nominal attractor. Simply using the neighborhood of embedded states in the varied set that is closest to the initial condition could lead to an incorrect eSV in this case because the selected neighborhood does not provide reasonable analogues for the initial condition.

In general, the ranking methodology places the worst performing neighborhoods near the bottom of the ranking. However, there is still considerable variability in eSVF accuracy for highly ranked neighborhoods so it is not sufficient in and of itself. The method's value lies in the fact that it quickly provides a list of reasonably good neighborhoods, and thus can be used to save time when checking for proportionality (discussed next) by providing a basis for limiting the number of neighborhoods that

need to be checked in this subsequent stage.

The second validation of constructed eSVs is ensuring reasonable neighborhood coefficients. The α coefficients for successful eSVs must all be less than 1 for the eSV to meet the requirements of this test. This ensures that all of the states in the neighborhood are contributing relatively equally in predicting the future trajectory.

The third validation of constructed eSVs is a proportionality check (in conjunction with a colinearity check). It only applies to eSVs for which we know the corresponding parametric variations, such as those generated to serve as part of a basis set. The proportionality check requires eSVs meet the linearity requirement of Eq. (3.7). That is, any change in a given parameter perturbation δp should elicit a proportional change in the magnitude of the eSV. Checking proportionality requires having at least two different parameter perturbations for each parameter of interest available when generating SVFs belonging to the basis sets. The proportionality check can be used to reduce the error in the acceptable eSVs to very low levels for noiseless data.

3.3.4 Combination

Once a collection of validated eSVs is obtained, one can combine them into an eSVF in the form of a column vector of individual eSVs. If one is concerned with identifying only a single parameter, simply examining a test vector's proportionality to this eSVF can determine the unknown variation. However, to identify linearly independent changes in the attractor that occur under multiple simultaneous parameter variations, proper orthogonal decomposition (POD) is required [32, 58, 31, 34, 35]. When different eSVFs corresponding to several different parameter variations are collected as column vectors, they can be used to form a matrix $\mathbf{Q}$. The correlation matrix $\mathbf{C} = \mathbf{Q}\mathbf{Q}^T$ can then be constructed. The dominant eigenvalues of the correlation matrix indicate the number of linearly independent parameter changes that can be identified and the corresponding eigenvectors provide the basis for doing so.

3.3.5 Measuring Prediction Error

To determine the accuracy of eSVs, it is necessary to have some means of determining eSV error. When predictions are made for a single time series, it is typical to report the root mean square (rms) prediction error for out-of-sample data. This means that while most of the time series is used as a training set to determine the parameters to be used in the local modeling, the remainder of the series is sequestered to serve as a test set. This provides an independent repository of states for which predictions

can be made using local models, but for which one also knows future states exactly. To determine the modeling error, one simply compares model predictions to known future states.

However, in constructing eSVs, we are making predictions for initial conditions on the nominal attractor using data from the varied attractor. This means that we have no test set to sequester. Thus, for cases when time series data alone is available, it seems that estimates of an eSVF's efficacy must be based solely on its ability to identify parameter variations accurately. However, when generating time series data from flow equations, there is an advantage in that the variables of the dynamical state that are not being embedded (and that would normally be unknown) can be retained. Having knowledge of these normally hidden state variables allows eSVs to be checked analytically.

An example serves to illustrate the methodology. Consider a two dimensional dynamical system with a state $\mathbf{x} = [x_1\ x_2]^T$ that is also embedded in two dimensions using the x_1 variable. One can rewrite Eq. (3.1) as

$$\begin{bmatrix} \dot{\delta x_1} \\ \dot{\delta x_2} \end{bmatrix} = \begin{bmatrix} \frac{\partial f_1}{\partial x_1} & \frac{\partial f_1}{\partial x_2} \\ \frac{\partial f_2}{\partial x_1} & \frac{\partial f_2}{\partial x_2} \end{bmatrix} \begin{bmatrix} \delta x_1 \\ \delta x_2 \end{bmatrix} + \begin{bmatrix} \frac{\partial f_1}{\partial p} \\ \frac{\partial f_2}{\partial p} \end{bmatrix} \delta p. \tag{3.18}$$

The equivalent of Eq. (3.4), the map involving the state transition matrix, is then given by

$$\begin{bmatrix} \delta x_1(t+\tau) \\ \delta x_2(t+\tau) \end{bmatrix} = \begin{bmatrix} \phi_{x_1x_1} & \phi_{x_1x_2} \\ \phi_{x_2x_1} & \phi_{x_2x_2} \end{bmatrix} \begin{bmatrix} \delta x_1(t) \\ \delta x_2(t) \end{bmatrix} + \begin{bmatrix} b_{x_1} \\ b_{x_2} \end{bmatrix} \delta p. \tag{3.19}$$

Here, the time t corresponds to the initial condition in the embedded state, and the time $t+\tau$ corresponds to a future state, which occurs at a time lag τ later. Since both the nominal and the varied trajectories are required to have the same initial embedded state, one has a boundary value problem, as $\delta x_1(t) = \delta x_1(t+\tau) = 0$, in Eq. (3.19). One obtains two equations for variations in the variable x_2 as

$$\delta x_2(t) = \frac{-b_{x_1}\delta p}{\phi_{x_1x_2}}, \tag{3.20}$$

$$\text{and} \qquad \delta x_2(t+\tau) = \phi_{x_2x_2}\delta x_2(t) + b_{x_2}\delta p. \tag{3.21}$$

Integrating Eq. (3.18) between t and $t+\tau$ in conjunction with the original flow $\dot{\mathbf{x}} = \mathbf{f}(\mathbf{x}, p, t)$, allows one to obtain the unknown entries of Eqs. (3.20) and (3.21). One integrates once with the initial conditions $[\delta x_1\ \delta x_2]^T = [0\ 1]^T$ and $\delta p = 0$ to obtain

$\delta x_1(\tau) = \phi_{x_1 x_2}$ and $\delta x_2(\tau) = \phi_{x_2 x_2}$, and again with initial conditions $[\delta x_1\ \delta x_2]^T = [0\ 0]^T$ and $\delta p = 1$ to obtain $\delta x_1(\tau) = b_{x_1}$ and $\delta x_2(\tau) = b_{x_2}$. Using these to solve Eqs. (3.20) and (3.21), one finds the δx_2 values for $\delta x_1 = 0$ at t and $t+\tau$. Integrating from either of these states with the known δx_2 values and a specified δp allows the calculation of δx_{1A} and δx_{1B} at $t+\Delta T$ and $t+\tau+\Delta T$. These quantities, δx_1 and δx_2, are the two components of the eSV. Figure 3.1 illustrates this when $x_* = x_1$. Note that this technique for validating eSV predictions only works when the dimensions of the original state space and the embedded state space are equal and is susceptible to singularities if the parametric variation is large or the evolution time is long.

3.4 Time Series Sources

3.4.1 Simulated Time Series Sources

Two familiar dynamic systems are used to generate simulated time series for analysis. The first system is the well-known Lorenz attractor whose equations are given by

$$\begin{aligned} \dot{x} &= \sigma(y - x), \\ \dot{y} &= -xz + rx - y, \\ \dot{z} &= xy - bz, \end{aligned} \tag{3.22}$$

where x, y, and z are state variables, and σ, r, and b are system parameters. For these parameters, the standard nominal values $\sigma = 10$, $r = 28$, and $b = 8/3$ were chosen. The system was sampled every $\Delta t = 0.05$. Collected data consisted of 10^5 samples for each data set with 10^4 samples on the nominal attractor serving as initial conditions.

The second system for demonstrating the approach is a Duffing oscillator whose representation is

$$\begin{aligned} \dot{x} &= y, \\ \dot{y} &= -x^3 + x - by + A\sin z, \\ \dot{z} &= \omega, \end{aligned} \tag{3.23}$$

where x, y, and z are state variables, and A, b, and ω are system parameters. The nominal parameter values were $A = 0.4$, $b = 0.25$, and $\omega = 1$. The system was sampled 100 times each driving period, and 10^5 samples for each data set were collected with 10^4 samples on the nominal attractor serving as initial conditions.

The data sets generated computationally were also corrupted by having various

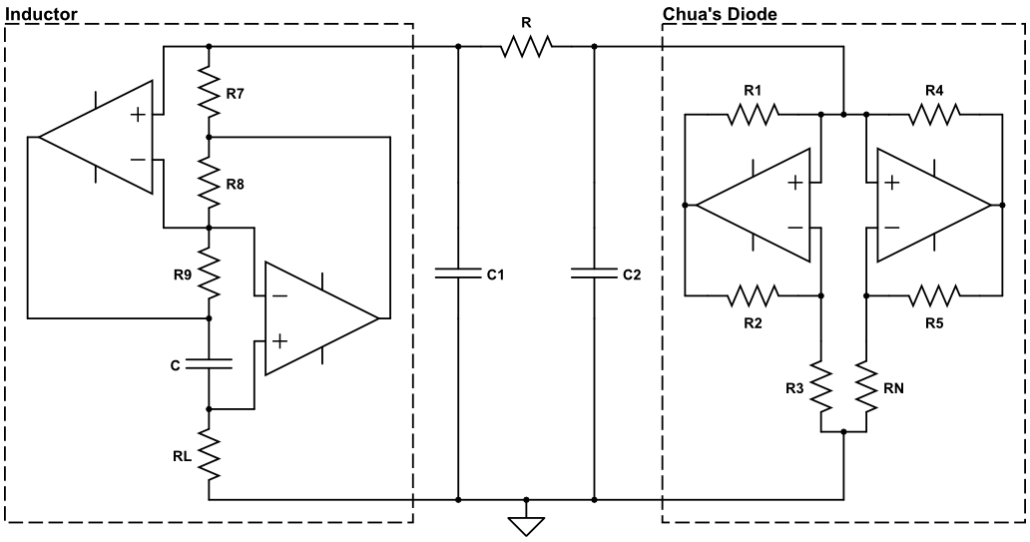

Figure 3.3: Layout of the Chua's circuit used to acquire experimental data.

levels of Gaussian white noise added to them. This additive noise has the form

$$x_n = s_n + \eta_n, \tag{3.24}$$

where x_n is the noisy signal, s_n is the clean signal, and η_n is the additive white noise included at each time instant indicated by subscript n. The relative noise level can then be expressed as

$$\frac{<\eta^2>}{<(s-<s>)^2>}, \tag{3.25}$$

with $<>$ representing the mean.

3.4.2 Experimental Time Series Sources

One source of experimental time series is a variant on the well-known Chua's circuit where the inductor is replaced by an op-amp realization of a gyrator [72]. Fig. 3.3 shows the layout of the circuit. The relevant component values are given in Tab. 3.1. These are identical to those in [72] except the capacitors are adjusted to 10 nF and 100 nF respectively. Within the gyrator is a variable resistance R_L. One of the resistors within the realization of Chua's diode is also replaced with a variable resistor R_N. Thus, the circuit has three parameters (R, R_L, and R_N) which can be varied (to construct eSVFs) and also be identified.

During each test, the system was sampled for approximately 10^6 data points using a digital to analogue converter having a 16-bit resolution over a $\pm$10V range. A set

Table 3.1: Chua's circuit properties

Component	Value
R1	220 Ω
R2	220 Ω
R3	2.2 kΩ
R4	220 kΩ
R5	220 kΩ
R7	100 Ω
R8	1 kΩ
R9	1 kΩ
R	2 kΩ pot
R_L	2 kΩ pot
R_N	5 kΩ pot
C	100 nF
C1	10 nF
C1	100 nF

of 10^4 samples was drawn from the nominal system to serve as the set of initial conditions.

Another source of experimental time series is a smart sensing beam consisting of an aluminum body with two PZT patches in a bimorph configuration providing actuation. The relevant dimensions and properties of the beam and PZT patches are given in Tab. 3.2.

This beam is also equipped with a capacitive sensor at its tip, which measures beam deflection. This signal is amplified and conditioned by a B&K NEXUS four channel charge conditioning amplifier and fed to a National Instruments field programmable gate array (FPGA) PCI-7833R which, in conjunction with custom LABVIEW programs, allows it to be recorded and processed. The FPGA modifies the signal according to a control law before feeding it back to the beam as an excitation through a Krohn-Hite amplifier, as shown in Fig. 3.4. For all of the experiments, the conditioning amplifier was set to a gain of 10 mV/ms^2, and the feedback amplifier had a gain of approximately 144 dB. The feedback law specified in the FPGA was of the form

$$F = \alpha x + \beta x^2 + \gamma x^3 + A \sin \omega t, \tag{3.26}$$

where F is the feedback signal prior to amplification, x is the input signal, and α, β, γ, A, and ω are controller parameters. All signals are measured in volts. The

Table 3.2: Smart sensing beam properties

Property	Aluminum Beam	PZT Patch
Length (mm)	280	60
Width (mm)	15	15
Thickness (mm)	1.27	1
Young's Modulus (GPa)	68.9	62
Density (kg/m^3)	2660	7800
Poisson's Ratio	0.33	0.31
Piezoelectric Constant (10^{-9} mm/V)	–	-300

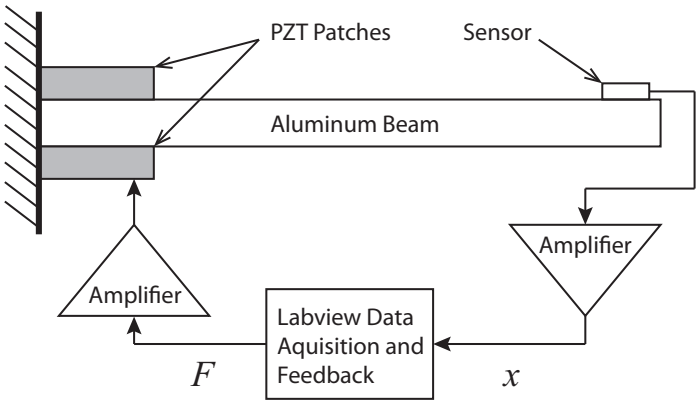

Figure 3.4: Layout of the experimental data acquisition set-up for a smart sensing beam.

parameters were set to $\alpha = -2$, $\beta = 0$ V^{-1}, $\gamma = 1$ V^{-2}, $A = 3$ V, and $\omega = 670$ Hz. A spatially distributed attractor was produced in the embedded state space. Feedback was supplied to the system at a frequency of 100 kHz, and data was recorded at a frequency of 10 kS/s. During each test, the system was sampled for approximately 10^7 data points. A set of 10^4 samples was drawn from the nominal system to serve as the set of initial conditions. Parametric variations were generated by adding small amounts of mass at various positions along the beam.

3.4.3 Initial Data Processing

Before any eSVFs can be constructed in an embedded state space, an appropriate dimension [73, 74] and time-delay [75, 76] with which to construct time-delay co-

ordinate vectors need to be determined. These two quantities depend on both the dynamical system being studied and the way in which the system is sampled. Both factors can be determined using available software, such as the TISEAN package [77] or other specialized programs, such as those for determining dimension based on false strands [74]. The TISEAN package is also useful for determining whether or not given dynamics are chaotic via a calculation of the largest Lyapunov exponent (a system is chaotic when this exponent is positive).

3.5 Results and Discussion

3.5.1 Simulated Time Series

For the simulated time series, using the data processing techniques in Section 3.4.3, we found that an embedding dimension $m = 3$ appears sufficient for the Lorenz system, and the best time-lag based on mutual information is approximately $\tau = 3$ ($\Delta t = 0.15$). For the Duffing oscillator, we choose either to embed x and y in an $m = 2$ embedding, treating the phase information (z) as known, or to separately fully embed in a $m = 3$ dimension embedding. For the Duffing system, the appropriate time delay is approximately $\tau = 10$.

The choice of time-delay is a critical factor in constructing eSVs. If the time-delay selected in the case of the Lorenz attractor is not optimal according to the first minimum of the mutual information, the error in eSV magnitudes increases significantly, in some cases doubling versus the error at the optimal time-delay.

With embedding and time-delay determined, one can apply the proposed methods to construct embedded eSVs. An example of such a construction is shown in Fig. 3.5. The states indicated by small o's represent varied trajectory points while the nominal trajectory is indicated by the large O. The semi-analytical prediction of the varied trajectory based on the state transition matrix formulation is indicated by the $\square$, while the prediction of the local model is indicated by $\times$. A coincident $\square$ and $\times$ indicate an accurate prediction. A 1% variation in σ is being captured by this eSV for the Lorenz attractor.

The Lorenz system affords one the opportunity to compare the locations of initial conditions which are appropriate for constructing eSVs (as determined by the process outlined in Section 3.3) with the locations of initial conditions generating low error eSVs (as determined via the analytical methodology outlined in Section 3.3.5). Figure 3.6 illustrates one way to make this comparison. On the left, validated eSV

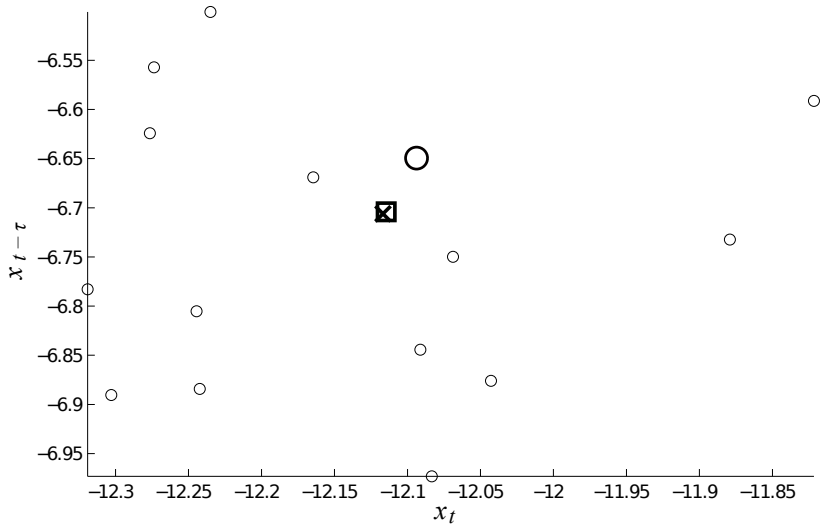

Figure 3.5: An example of a good eSV prediction for the Lorenz attractor. The large O represents the nominal trajectory; small o's indicate the varied data in the neighborhood nearby. The $\times$ represents a prediction of the varied trajectory via local modelling and the $\square$ via semi-analytical methods. Coincidence of the $\times$ and $\square$ indicate a good prediction.

initial conditions for 1% and 2% variations in σ are indicated by the darker points; the remainder of the initial conditions are shown by the lighter points. We consider the eSV validated if its proportionality is within 5% of the expectation. On the right, the same sets of initial conditions are shown, but in this case they are darker if the error in constructing a vector corresponding to 1% variation in σ is less than 10% and lighter otherwise. Here we are making predictions for $\Delta T = 9$. The similarity between the two plots confirms the methodology we have outlined for validating eSVs does select the eSVs with the lowest error. Moreover, these plots show that the distribution of low error / successfully validated eSVs is non-uniform across the attractor, often being concentrated in bands or clusters based on the deformation. Careful tightening of the proportionality requirement in the validation step will reduce the number of acceptable initial conditions but those that remain will generally produce eSVs with less error. Similar results hold for the Duffing oscillator, and when one only embeds two of the state vectors and retains the phase as additional information, the average eSV magnitude prediction error is generally lower.

With both surrogate ranking and proportionality validation one can consistently generate eSVFs with low error in low noise environments. These accurate eSVFs allow for excellent parameter reconstructions. For example, in the case of the Lorenz

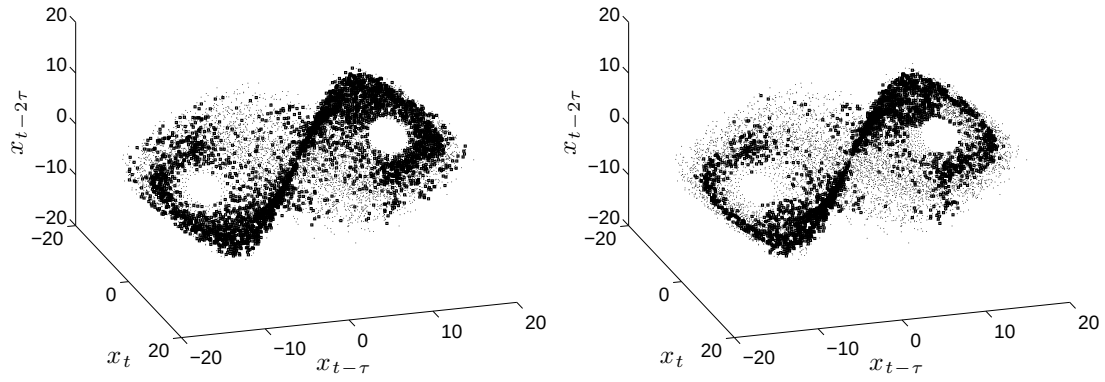

Figure 3.6: Initial conditions used in generating eSVs for the Lorenz data; darker points indicate valid eSVs (left). The same set of initial conditions; darker points indicate eSVs having less than 10% error (right).

Table 3.3: Simulated time series parameter reconstruction

Case	Parameter	Variation (%)	eSVF Prediction (%)
1	σ	1.50	1.47
	r	0.00	0.01
2	σ	0.00	0.04
	r	1.50	1.65
3	σ	1.50	1.46
	r	1.50	1.62
4	σ	3.00	2.97
	r	3.00	3.18

attractor after having collected initial eSVFs for changes in σ, r, and b of 1% and 2% one can perform the reconstructions shown in Tab. 3.3. These required the calibration eSVs to have a proportionality within 5% of the expectation based on the specified parameter variations. The eSVs were recorded for an evolution time of one time step ($\Delta T = 1$).

These results demonstrate the ability to make good predictions of parameter variations in this system, even when they occur simultaneously. The case where both parameters are changed by 3% also shows that even in cases where one extrapolates beyond the eSVFs collected initially (here validations were performed only up to 2%) one can still generate good results.

The accuracy of these types of parameter variation predictions is affected by several factors. The first of these is the level of proportionality required to validate

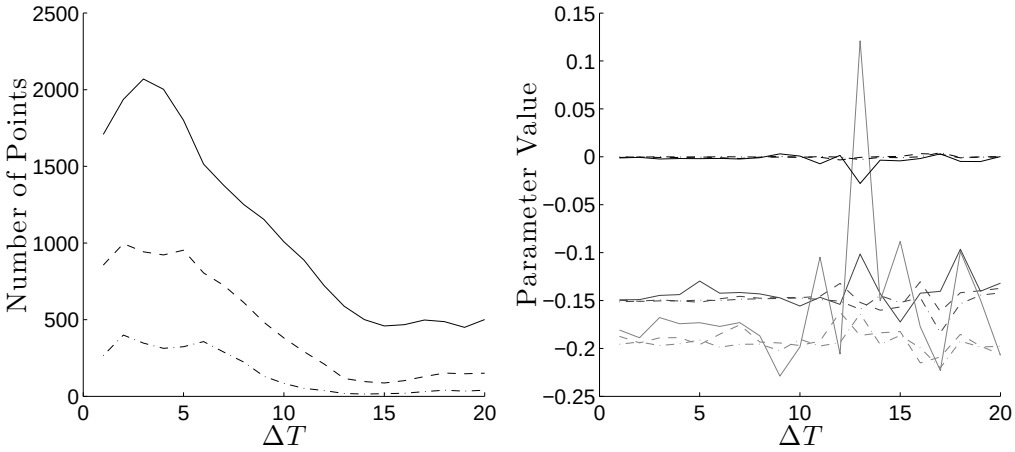

Figure 3.7: Number of initial conditions validated for eSV construction (out of 10^3) (left). Predictions of the parameter variations (right). Solid line corresponds to 5% proportionality, dashed line corresponds to 2% proportionality, dashed-dotted line corresponds to 1% proportionality.

calibration vectors. Figure 3.7 illustrates how tightening the proportionality requirement influences the predictions over a range of different evolution times. Here the actual values of the variations are -0.15 in σ, -0.2 in b and 0 in r. It is obvious that as the proportionality requirement is tightened, the predictions generally improve, markedly from 5% to 2% and only slightly from 2% to 1%. The number of initial conditions that are considered valid also declines.

Figure 3.7 also demonstrates that the length of the evolution time ΔT can have a large effect on eSV accuracy. If this time is too short, the eSVs will have small magnitude and will be prone to large error for any small errors in the individual time series predictions. For large times, a dynamic system that is chaotic will lose predictability and the error will again be large. Our predictions of b with a 5% proportionality requirement become inaccurate for $\Delta T > 10$ because a few of the initial conditions that pass the proportionality test generate eSVs that are in error. This suggests that it is prudent to make variation predictions over several different ΔT values and look for a consistent result before drawing any conclusions about how parameters may have changed.

A third factor affecting the accuracy of parameter predictions is quantity and density of the time series themselves. Having more data from which to construct a local model about a given initial condition can lead to an improvement in the predictions. The results are more subtle, but Fig. 3.8 shows how increasing the number of points in the time series from 10^5 to 10^6 can slightly reduce some of the

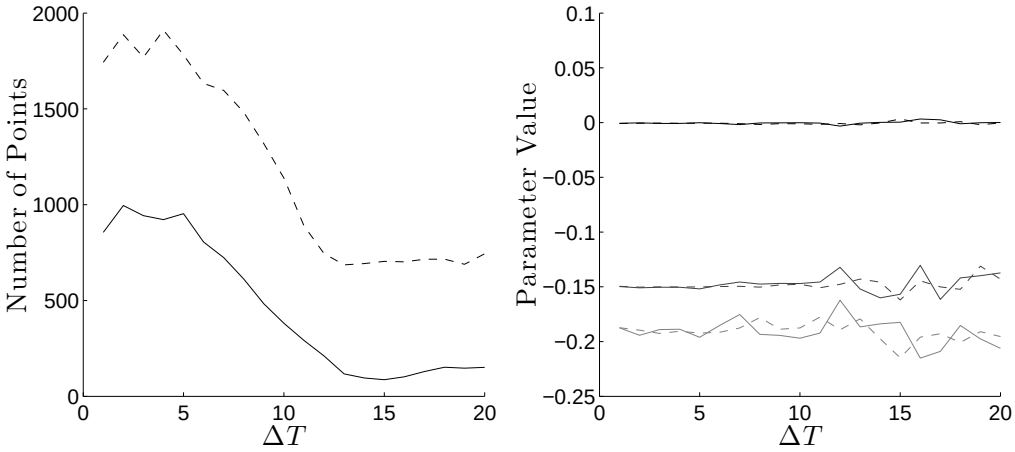

Figure 3.8: Number of initial conditions validated for eSV construction (out of 10^3) (left). Predictions of the parameter variations (right). Solid line corresponds to 10^5 points in time series, dashed line corresponds to 10^6 points.

variability in the variation predictions. The proportionality enforced for this plot was 2%.

The error in embedded eSVs is also significantly influenced by noise. To investigate this, noise was added to the simulated time series as described in Eq. (3.24). The levels added ranged from 0.0001 to 0.1. For levels of noise 0.0001 and below, errors in eSV magnitude were not significantly influenced. However, for noise around 0.001 the variation prediction began to be degraded. For higher levels of noise it was often impossible to find any initial conditions that generated eSVs meeting the proportionality requirements. This suggests that minimizing noise in any experimental system is very important in order to be able to construct eSVs. It is possible that by predicting both the future points on the nominal trajectory as well as on the varied trajectory (rather than just accepting the nominal trajectory data at face value) the impact of noise could be further reduced through the effects of neighborhood averaging, but this has not been explored here. Table (3.4) shows the impact of noise on eSV parametric variation reconstruction for $\Delta T = 3$.

3.5.2 Experimental Time Series

The investigation of eSVs using time series data generated by simulated systems shows that the methodology laid out for eSV construction is reliable. However, it is also important to be able to achieve similar results with experimental data to confirm that embedded SVF construction is applicable to real systems. For this reason, we first

Table 3.4: Simulated time series parameter reconstruction with noise

Noise Level	Parameter	Variation	eSVF Prediction
0	σ	-0.15	-0.149
	b	-0.20	-0.191
	r	0.00	0.001
0.0001	σ	-0.15	-0.144
	b	-0.20	-0.194
	r	0.00	-0.001
0.001	σ	-0.15	-0.132
	b	-0.20	-0.127
	r	0.00	-0.008

Table 3.5: Chua's circuit time series parameter reconstruction

Case	Parameter	Variation ($\delta\Omega$)	eSVF Prediction ($\delta\Omega$)
1	R	32	34.3
	R_L	0	0.3
2	R	0	3.9
	R_L	-47	-44.2
3	R	-33	-27.2
	R_L	48	49.8

examine the effects of parametric variation by adjusting R and R_L in Chua's circuit.

Applying the techniques for determining state dimension and time-delay, we found that the experimental data should be embedded in a state space having $m = 3$ and a time-delay of $\tau = 9$. The reconstructed attractor using these parameter values is shown in Fig. (3.9).

Once initial calibration eSVFs are taken about the nominal parameter values one can perform the reconstructions shown in Table 3.5. The fact that the data has low noise (the noise to signal ratio could be as low as 10^{-10} based on the resolution of the analog to digital converter) no doubt contributes to the predictions being accurate.

Using a similar process, the cantilever beam time series are required to be embedded in a state space having $m = 4$ and a time-delay of $\tau = 16$ (0.16 ms). When 5 mg and 15 mg additions to the beam are used to generate initial eSVFs one can perform the reconstructions shown in Table 3.6.

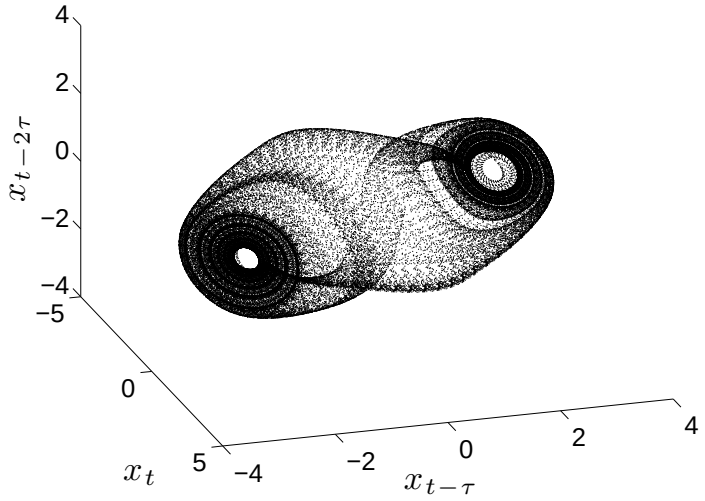

Figure 3.9: A 3-dimensional projection of the Chua's oscillator attractor.

Table 3.6: Cantilever beam time series parameter reconstruction

Case	Location	Mass (mg)	eSVF Prediction (mg)
1	Tip	10	9.71
	Middle	0	-0.11
2	Tip	0	-0.27
	Middle	10	10.21
3	Tip	10	10.13
	Middle	10	10.54

3.6 Conclusions

This paper presents a methodology for the construction of SVFs in time-delay embedding coordinates based on local linear modeling of time series. A specific method for weighting neighborhood states in local modeling called ePCA was introduced. This method minimizes quadratic cross terms in an effort to improve eSV accuracy. Local modeling proved to be a reliable means of constructing eSVFs and identifying parametric variations for both simulated and experimental time series. A technique for checking the accuracy of these SVF predictions was also presented for cases where the system equations are known and the dimension of the non-embedded state and the embedded state are equal. Being able to construct SVFs in embedded coordinates will make the application of SVFs to a wide variety of physical systems feasible, even

when it is not possible to measure the complete state.

CHAPTER 4

Rotating Fluid Microsensors with Nonlinear Feedback

4.1 Introduction

Detecting and characterizing small amounts of chemical and biological agents is important in many health and defense related applications. Fast and reliable identification of trace amounts of materials can be crucial for correct assessment and response in scenarios ranging from diagnosis of bacterial infections to counter-terrorism screening.

One way of providing chemical and biological detection is through the use of active, vibration-based micro-sensors. Typical vibration-based sensing methods apply a system excitation to the sensor and then monitor the dynamic response, which changes when the substance of interest is present. Frequency-shift methods based on changes in resonant frequencies caused by particles binding to a vibrating microstructure are examples of this approach [64, 78]. Unfortunately, when sensors exhibit nonlinearity, significant damping, or when sensor properties are liable to change over time (due to, for example, environmental changes or sensor damage), these frequency-shift based methods can lead to unsatisfactory results.

The case of vibration-based sensing in highly damped environments is of particular interest because detecting and quantifying particles in liquids is often necessary. For instance, being able to quantify different types of particles in a lab-on-a-chip environment could improve medical diagnosis. Resonant-frequency based detection is often poor in such damped environments because the quality factor is diminished and the resonant peak is no longer sharp. Burg and collaborators [15] constructed a resonator where flow is channeled within the resonating structure itself as one possible solution to this problem.

An alternate approach, taken here, is to minimize the effective damping by designing an immersed sensor which takes advantage of the flow to recover some of the energy lost to damping. This is challenging because only low Reynolds number flows are practical in liquid MEMS [79, 80]. Work on rotational galloping of prismatic structures is of particular interest, as we would like our system to be as near to this type of behavior as possible [81, 82].

In order to measure changes in system properties, such as added mass, we make use of an alternate metric known as sensitivity vector fields (SVFs) which quantify how attractors deform [58, 31]. SVFs are constructed by sampling system trajectories that diverge due to parametric variations and using the resulting snapshots of the deformation as references when the system changes under operating conditions. The SVF approach has several advantages. In many cases, using SVF analysis means that nonlinear features of the system can be enhanced and exploited to increase sensitivity rather than hindering the interrogation. As well, simultaneous sensing of multiple analyte properties with a single sensor is sometimes possible since we are dealing with vector, rather than scalar, features/quantities. Originally developed for structural health monitoring [35, 32, 26] in mechanical systems, SVF techniques have since been used to detect parameter variations in a variety of dynamical systems, including tapping mode atomic force microscopes [34].

The key to effectively utilizing SVF techniques is the design of nonlinear feedback controllers. These controllers need to provide system excitation which maximizes attractor deformations caused by changes in parameters of interest (thereby enhancing sensitivity) while minimizing attractor deformations caused by changes in other system parameters (thereby improving selectivity). We demonstrate how to design such controllers for a sensor using spline surfaces of feedback force optimized to enhance sensitivity.

4.2 Sensor Design Strategy

The primary challenge in designing an effective vibration-based micro-sensor for a liquid environment is overcoming, as much as possible, the high level of damping due to the viscosity of the liquid. Unlike in a near-vacuum or gas environments where damping can often be neglected, in liquids damping effects are not negligible and make frequency-shift based measurement difficult. In order to combat damping, the sensor must be designed in such a way that the effects of damping are reduced or measurements must be made using an alternate method that is more sensitive to the

desired analyte. Here we explore both of these options.

One strategy to try and overcome the high level of damping in a liquid is to harvest some energy from the oncoming flow to make up for the energy lost to damping. Examples of this type of energy gain include vibration-based energy harvesters [83, 84]. In some of these systems, the energy harvested from the flow reduces the effective damping experienced by the harvester until it is negative, and sustained motion ensues.

It is unclear if this type of energy harvesting is possible in an enclosed channel on the micro-scale. Simulations of rotational galloping found in the literature do not deal with high blockage ratios [81]. Additionally, inertial forces are small relative to viscous forces, and thus flows are restricted to low Reynolds numbers. If we consider a sensor in a square cross-section channel with dimensions on the order of tens of micrometers, we can expect pressure losses to be calculated similarly to a macro-scale system [79]. Using relevant micropump data [80] we can estimate the range of practical Reynolds numbers and pressure losses for channels of different cross-sections and lengths. For example, Figure 4.1 shows a plot of uniform velocity and pressure drop over a 1 mm length channel for a micropump with a maximum flow rate of 4.4 mL/min [80]. The acceptable pressure drop in this case is 21 kPa, so we would consider cross-sections larger than 100 μm by 100 μm. For these sorts of dimensions, Reynolds numbers based on a 10 μm face dimension will only be on the order of hundreds.

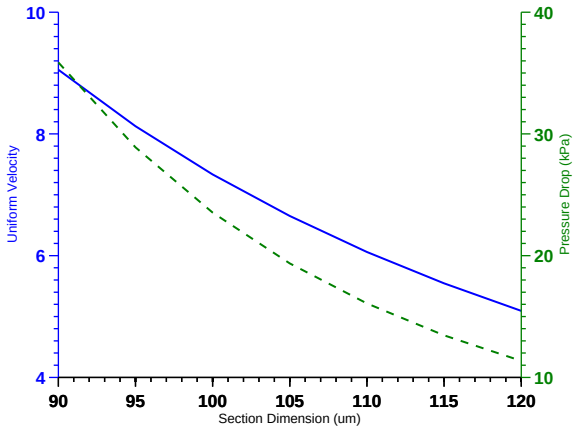

Figure 4.1: Uniform velocity and pressure drop for a 1 mm channel

4.3 Fluid System Simulations

To investigate the potential for energy harvesting, we consider two different sensor geometries. The first geometry consists of a flat plate that pivots about its geometric center with the pivot centered in the channel flow. Its largest face is parallel to the upper and lower channel walls when there is no flow as shown in profile in Figure 4.2. The channel considered is this case has H = 100 μm and W = 100 μm. The other relevant dimensions are D = 10 μm and L = 40 μm. The second geometry is also a flat plate, but its largest face is nominally at an angle of α to the upper and lower walls. Its pivot point is offset far from the geometric center of the plate and is also away from the center of the channel as shown in profile in Figure 4.3. The channel considered has H = 75 μm and W = 150 μm. Here D = 10 μm, L = 90 μm, and the angle α is 12°. The surrounding channels are 600 μm long. These geometries were selected as test cases because they are known to produce galloping-type instabilities under certain flow conditions [85].

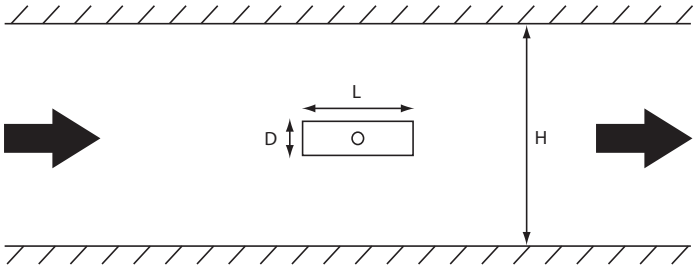

Figure 4.2: First system flow geometry

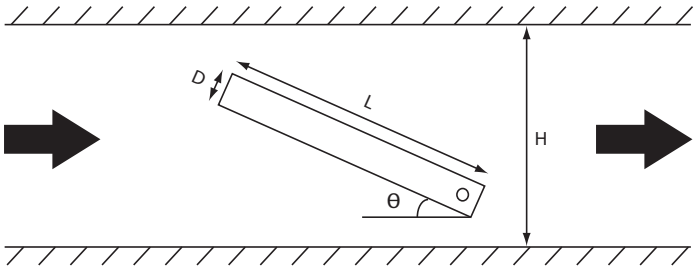

Figure 4.3: Second system flow geometry

The plates were considered to be made of silicon with nominal properties of E = 150 GPa, G = 64 GPa, and ρ_s = 2330 kg/m^3. The liquid was treated as water with ρ = 998.2 kg/m^3. The geometries of these sensors were generated in two forms for simulation in ANSYS CFX. One version was essentially two dimensional, consisting

of a mesh a single element thick, while the other contained the full system geometry, including the plates meshed as solid bodies, and took advantage of the symmetry at the channel midline. These systems were primarily meshed with tetrahedral elements. A close-up view of the mesh around one of the bodies is shown in Figure 4.4.

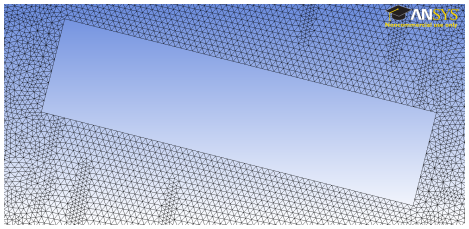

Figure 4.4: Computational domain for FSI simulation

Initial solutions of this FSI problem were carried out by examining the system in a quasi-static manner, evaluating the moments the fluid flow applied to the cross-sections at various angles from their nominal positions. Later, using the built in fluid-structure coupling in CFX, the models were simulated transiently with various inlet flow velocities in order to ascertain the effect of increased flow speed on the effective damping. The simulation was allowed to establish a steady-state condition, and then the section was perturbed by an applied moment to a position between 5° and 10° away from the nominal position. Some time later the moment was then removed. The recorded time series of the angular displacement θ (shown in Figure 4.3) for such cycles was then used to determine approximate values of the damping and the damped-vibration frequency of the system, using either fractional overshoot or logarithmic decrement techniques. Figure 4.5 shows a times series taken just after a moment has been applied to the cross-section, demonstrating its underdamped nature. Notice the decay envelope is not perfectly symmetric due to the fluid forces involved.

The transient analyses conducted using our 3D models showed displacements that are quickly damped in our two systems, with nominal damping coefficients ζ of approximately 0.2 and 0.18, respectively. As the flow rate is increased from zero flow rate to a large (and likely unrealistic value) of 5 m/s, the reduction in these damping coefficients is only about 10%.

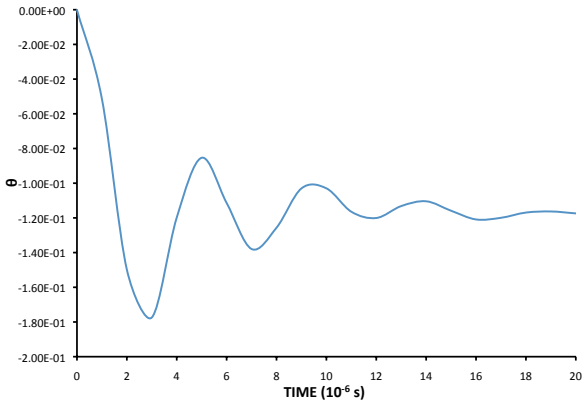

Figure 4.5: System response after a moment perturbation

4.4 Parameter Extraction

Whether the damping can truly be reduced via careful sensor design in order to take advantage of the oncoming flow, the second part of our strategy remains the same: measuring sensor changes using an alternate method, not based on frequency-shifts, that is more sensitive. In order to explore this further, the fluid-structure models previously discussed are recast as one degree of freedom (DOF) systems by making use of the damping properties calculated from simulations. With damping coefficient determined, each sensor can be modeled approximately as

$$\ddot{x} + b\dot{x} + {\omega_n}^2 x = N(x, \dot{x}, t) \ , \tag{4.1}$$

$$\text{where} \qquad \omega_n = \sqrt{\frac{k}{I}} \ , \tag{4.2}$$

$$\text{and} \qquad b = 2\zeta\omega_n \ . \tag{4.3}$$

The natural frequency is calculated by summing the moment of inertia of the section I and some 'added mass' based on the entrained fluid. Details on 'added mass' can be found in many hydrodynamics references [86]. $N(x, \dot{x}, t)$ represents the overall non-linear feedback force used to excite the system. By considering states of the form

$$\mathbf{x} = \begin{bmatrix} x_1 \\ x_2 \end{bmatrix} = \begin{bmatrix} x \\ \dot{x}/\omega \end{bmatrix} \ , \tag{4.4}$$

this system can be converted to a standard state space form $\dot{\mathbf{x}} = \mathbf{f}(\mathbf{x}, t)$ in order to apply SVF methods.

4.5 SVF Theory

SVFs are a way to quantify attractor deformations. If two different systems with initially coincident state space trajectories are compared, one system having a nominal set of parameters and the other having some parametric variations, the trajectories of these two systems will diverge over time. By sampling the diverged trajectories a specified period of time ΔT after coincidence, a vector can be generated connecting the sampled point on the nominal trajectory with the sampled point on the varied trajectory. This is a sensitivity vector (SV). An SVF is a collection of SVs computed over a system attractor for some parameter variation. This field characterizes how the varied attractor deforms with respect to the nominal attractor.

This can be formalized mathematically by considering a state space flow described by $\dot{\mathbf{x}} = \mathbf{f}(\mathbf{x}, p, t)$ where $\mathbf{x}$ is the state vector and p is the sensor readout, i.e. the parameter of interest that can be perturbed. Using a Taylor series to expand this flow about the nominal trajectory $\mathbf{x}(t) = \mathbf{x_o}(t)$ and a nominal parameter p_o one obtains

$$\delta\dot{\mathbf{x}} = \mathbf{A}(t)\delta\mathbf{x} + \mathbf{B}(t)\delta p \ , \tag{4.5}$$

$$\text{where} \qquad \mathbf{A}(t) = \left.\frac{\delta\mathbf{f}}{\delta\mathbf{x}}\right|_{\substack{\mathbf{x}=\mathbf{x_o} \\ p=p_o}} \ , \tag{4.6}$$

$$\text{and} \qquad \mathbf{B}(t) = \left.\frac{\delta\mathbf{f}}{\delta p}\right|_{\substack{\mathbf{x}=\mathbf{x_o} \\ p=p_o}} \ , \tag{4.7}$$

where only the linear terms are retained. Here $\delta\mathbf{x}$ is the state variation from the nominal trajectory, and δp is the parameter variation from the nominal parameter. Eq. (4.5) is valid as long as the discarded higher order terms remain small compared to the first order terms. For linear systems, this is always true since Eq. (4.5) is exact, and has no higher order terms. However, for nonlinear systems, both the parameter variation and the state variation must remain much less than one for Eq. (4.5) to hold. Thus, for nonlinear systems with specified initial variations there is a limit on the evolution time for which Eq. (4.5) is appropriate. Integrating Eq. (4.5) over the evolution time results in the equivalent map

$$\delta\mathbf{x}(t_o + \Delta T) = \Phi(t_o + \Delta T, t_o)\delta\mathbf{x}(t_o) + \mathbf{q}\delta p, \tag{4.8}$$

where Φ, the state transition matrix for the dynamical system (sensor), depends only on $\mathbf{A}(t)$, while $\mathbf{q}$ depends on both $\mathbf{A}(t)$ and $\mathbf{B}(t)$. For two trajectories which are truly initially coincident, $\delta\mathbf{x}(t_o) = \mathbf{0}$. Thus, any separation of the trajectories that develops over the evolution time is equal to the sensitivity vector $\mathbf{q}\delta p$. As long as the evolution time is short (in order to ensure the resulting changes to system behavior are locally linear with respect to the parameter variations) the sensitivity vectors will be linearly dependent on the parameter variation. Consequently, a change in a given system parameter will elicit a proportional change in the measured attractor deformation. When examining attractor deformations, this proportionality serves as the basis for quantifying parameter changes. Often, we refer to the normalized sensitivity vector $\mathbf{q}$, which is the sensitivity vector divided by the parameter variation. As normalized sensitivity vectors are independent of the level of parameter variation, they can be helpful in comparing results.

4.6 Feedback Design

The next question is how to maximize a system's SVs. The overall sensitivity will be effected by factors like the evolution time ΔT and the dynamics of the system. However, by changing the system through feedback, it is also possible to augment or amplify a system's natural sensitivity. Choosing an appropriate $N(x, \dot{x}, t)$ in Eq. (4.1) has the effect of changing the system and thereby the sensitivity.

$N(x, \dot{x}, t)$ in a real, physical system will be subject to some constraints. These constraints might include limits on the range of motion or the amount of force the controller can output. In this work, a limit is also placed on the attractor size since SV magnitude is closely related to attractor size. Within such constraints, we would like to design feedback to maximize a SVF.

Previous work by the authors helped to establish some basis for designing such feedback by considering an $N(x, \dot{x}, t)$ of the form

$$N(x, \dot{x}, t) = b_c\dot{x} - k_c x - \alpha_c x^3 + A\sin\omega t \ . \tag{4.9}$$

With $N(x, \dot{x}, t)$ specified, Eqs. (4.1) and (4.5) can be integrated simultaneously to find SVs. Using this method, the advantages and disadvantages of chaotic and non-chaotic regimes for generating SVFs with respect to parameter ω_n for different evolution times ΔT and phases of the harmonic excitation were demonstrated in Chapter 2. We were also able to optimize the control parameters in the fixed controller form given by Eq.

(4.9).

However, having a controller of fixed form, especially one with a relatively low number of polynomial terms, greatly reduces the possible distributions of feedback force across the state space. For this reason, we examine feedback that is based on control points distributed over the state space which can be interpolated with splines to arrive at an overall feedback law. This arrangement allows for a feedback force distribution that can take on a different variety of surface shapes than one based on polynomials alone. We specifically consider the case where

$$N(x, \dot{x}, t) = R(x, \dot{x}) + A \sin \omega t \tag{4.10}$$

and $R(x, \dot{x})$ is given by a spline surface of forces distributed over the state space.

The form of $R(x, \dot{x})$ can be optimized by adjusting the force values at certain control points. This form of feedback has been used in the past and proved a very effective approach to maximizing average SV magnitude. When using spline force surfaces for state feedback, almost all the initial parameter sets that we optimized resulted in higher sensitivities than in the case of a polynomial force controller. Part of this comparison is undoubtedly unfair since the polynomial controller has fewer adjustable parameters with which to begin. Nonetheless, it seems clear in examining the topology of optimized spline force surfaces, that this type of feedback surface would be difficult to construct with a low number of polynomial terms. When the constraint on the symmetry of the force surface is removed, even higher sensitivities can be generated when all the other constraints remain fixed. This is somewhat expected, since giving the optimizer more freedom in the parameter space should result in improved solutions, but it does highlight how significantly the assumed form of the controller function can effect its ability to provide the highest sensitivity regimes. We also attempted to optimize sensitivity using a larger number of control points to determine whether increasing the number of points could lead to large improvements in sensitivity. When the number of points was doubled for the case of the symmetric controller, this sometimes did not lead to significantly improved sensitivities; however, in the case of greatest improvement the sensitivity roughly doubled. Thus, we believe a more varied or "wavy" surface can sometimes yield significantly higher sensitivity regimes.

4.7 Application to Fluid Sensor Systems

The techniques in the section above are directly applicable to fluid sensor systems once they have been reduced to 1 DOF, first-order state space systems as previously outlined. As a specific example, consider the inclined plate geometry and $x = \theta$. The suitably transformed system will have values of $b = 2.5 \cdot 10^4 \text{s}^{-2}$ and $\omega_n = 6.4 \cdot 10^4 \text{s}^{-1}$. Bounding the spline surface between $\pm 1 \cdot 10^8 \text{s}^{-2}$ while considering several different combinations of A and ω allows for the calculation of various optimal controllers. Initial conditions for the spline surface were generated by dividing the total possible range by five and assigning a certain level of feedback for each of nine control points in a specified pattern or at random. One example of a specific pattern has all of the inner points closest to the origin assigned one value (either positive or negative) and all of the outer points farther from the origin assigned another value (again, either positive or negative). The parameter of interest, to which we want to increase the sensitivity, can be either I or ω_n.

Results obtained while specifying ω_n as the parameter of interest have shown that, in some cases, the optimization can result in SV magnitudes improving several times over the initial, pseudo-random feedback surface. In the best cases, we were able to improve sensitivity tenfold. Almost all of the returned results are limit cycle attractors; this is expected based on our previous work. However, these limit cycles sometimes do not have the same period as the forcing harmonic due to the influence of the spline surface feedback.

A larger set of optimizations was also conducted for the same system with completely random initial conditions selected on an interval centered on zero. Various combinations of surface constraints and harmonic forcing magnitudes and frequencies were explored. One hundred trials were carried out for each specific combination. Depending on the case, the individual initial values were constrained to be between ten and fifty percent of the allowable range. We saw much more diversity in the resulting optimal attractors for this larger set of simulations, including some chaotic attractors. Again, we found that sensitivity could be improved over the base value by about ten times for cases which were already quite sensitive due to the forcing frequency approaching the natural frequency.

Even greater sensitivity improvements are possible when either the spline surface magnitude constraint is relaxed or a larger number of points are used to define the surface. When the allowable magnitude is doubled, and for a driving frequency of $\omega_d = 6.0 \cdot 10^4 \text{s}^{-1}$, Table 4.1 lists the three greatest improvements in sensitivity over

the initial values.

Table 4.1: Sensitivity improvements due to changes in surface constraints

Set	Sensitivity Improvement Multiplier
1	21.7
2	11.6
3	11.3

Both chaotic and limit cycle cases are included in these attractors. Figures 4.6 and 4.7 show plots of two of the locally optimal surfaces and their attractors. If instead of increasing the allowable moment, the number of points used to define the surface is increased, sensitivity can also be greatly improved. In these cases, most of the high sensitivities are generated by chaotic attractors. Table 4.2 lists the three surfaces showing the greatest improvement in sensitivity over the initial conditions and Figure 4.8 shows one of these high sensitivity surfaces and its attractor.

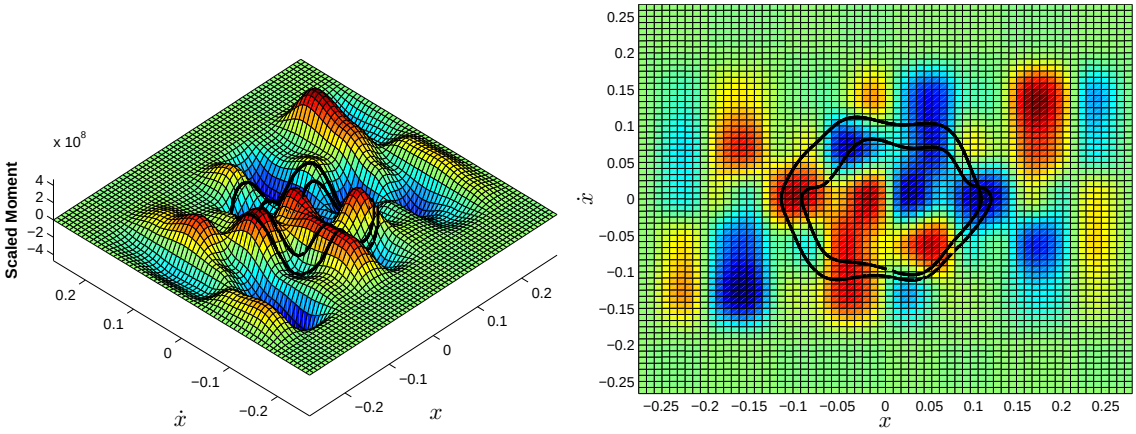

(a) (b)

Figure 4.6: High sensitivity limit cycle attractor for the angled plate sensor

If we instead consider the parallel plate geometry, the suitably transformed system will have values of $b = 3.9 \cdot 10^5 \text{s}^{-2}$ and $\omega_n = 9.8 \cdot 10^4 \text{s}^{-1}$. We bound the spline surface as before and then consider simulations, again choosing completely random initial conditions selected from an interval centered on zero and constrained to be between ten and fifty percent of the overall constraint range. We can again generate improvements in sensitivity that are several tens of times what was seen in the base case.

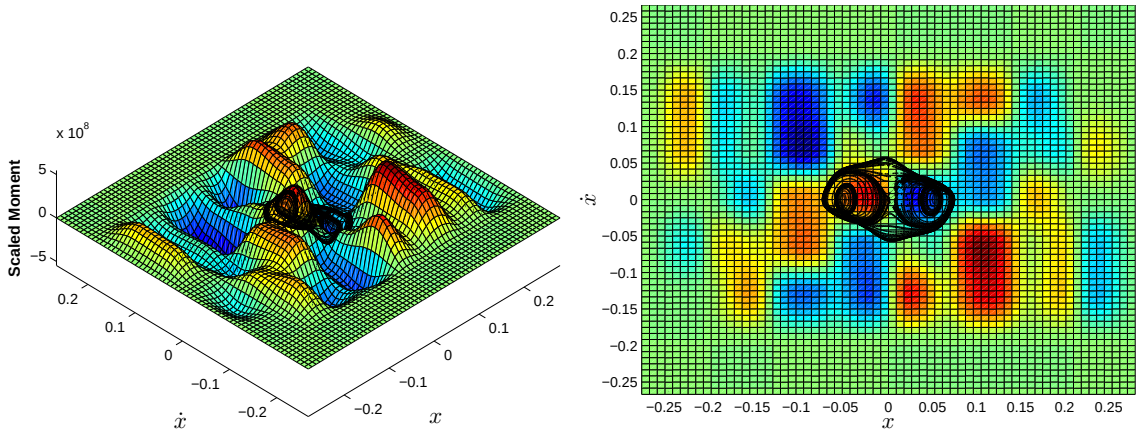

(a) (b)

Figure 4.7: High sensitivity chaotic attractor for the angled plate sensor

Table 4.2: Sensitivity improvements due to a higher number of interpolation points

Set	Sensitivity Improvement Multiplier
1	28
2	24.8
3	19.4

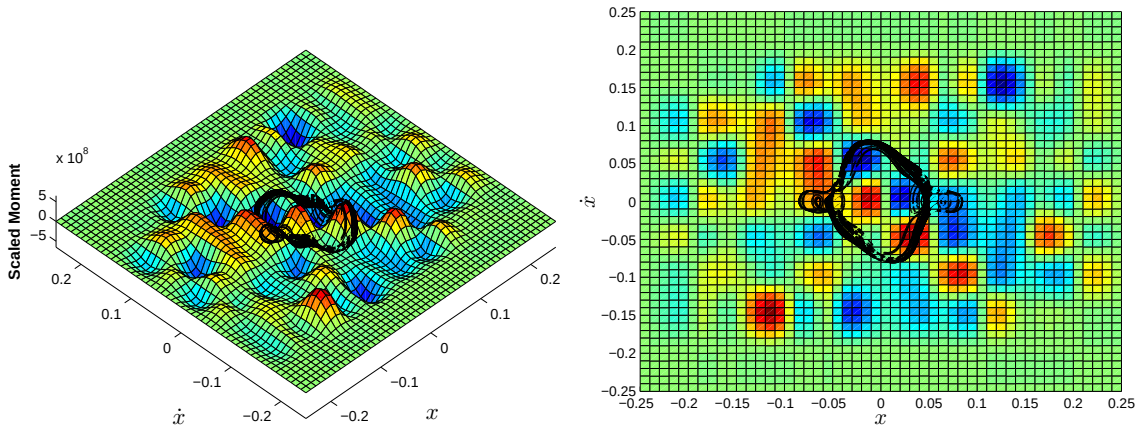

(a) (b)

Figure 4.8: High sensitivity chaotic attractor based on a finer surface mesh

4.8 Conclusions

We have demonstrated that for the low Reynolds number and high blockage ratio regimes involved in enclosed micro-system channel flow, it is difficult to design a geometry which will harvest energy from the oncoming flow and thereby reduce the effective damping ratio. Work involving a fluctuating incoming flow shows that we can generate motion in this case.

Using spline surfaces to define feedback forces over the state space and then optimizing these surfaces in order to maximize SV magnitude was shown to be an effective technique. We have illustrated how SVF techniques in conjunction with spline surfaces can be applied to our immersed sensors if they are modeled as simple 1 DOF systems. We have also shown how this feedback can be optimized, leading to large improvements in sensitivity. Thus, we have demonstrated that SVF techniques are effective in improving sensitivity, and may allow sensing in highly damped environments where traditional frequency-shift methods are not an alternative.

CHAPTER 5

System Augmentation and Modal Analysis Techniques

5.1 Introduction

Identifying parameter variations in nonlinear systems is increasingly important. This is true in traditional areas, such as structural health monitoring [1, 2], where the need for reliable and easy to understand damage detection techniques only grows as engineering systems become more and more complex. It is also true in non-traditional areas, such as in nonlinear micro-scale systems designed for microscopy or other sensing tasks [87], where improved identification of parameter variations can result in better device performance. Several different methods of identifying parameter variations specific to nonlinear systems have been proposed recently, including auto-regressive time series modeling [6], chaotic interrogation [17], and phase space warping [56]. However, these methods can have a high computational burden, require specialized interrogation, or be difficult to interpret. Thus, the ability to use more traditional modal analysis, which is well-established and easily understood, is desirable even for nonlinear systems.

System augmentation [43, 47, 44, 45, 48, 88, 46] is one way of casting a nonlinear system into a linear form so that modal analysis is applicable. For system augmentation to be successful, a system model that includes the forms of any nonlinearities must be available. Each nonlinearity in the system model can then be replaced with a new, corresponding linear variable, and additional differential equations involving the newly created variables can be added to the original system equations. The new differential equations are forced in such a way that the evolution of each new variable matches that of the respective nonlinearity being replaced in the original system. The advantage in this new, augmented system is that it is linear, making modal analysis applicable.

Starting from time series of the states of the original system and any inputs, the augmented variables and the augmented forcing can be computed via the equations describing the augmentation. The state and forcing data of the entire augmented system are then amenable to being analyzed using modal identification techniques, such as direct system parameter identification (DSPI) [49, 50] and smooth orthogonal decomposition (SOD) [51, 52]. Using the eigenvector information from the modal analysis, system parameter variations can be computed via a number of different techniques. In this work, generalized minimum rank perturbation theory (GMRPT) [43, 48], which originated out of minimum rank perturbation theory (MRPT) [89], is used to identify parameter variations.

Previous work on system augmentation and GMRPT is extended by showing that system augmentation techniques are applicable to systems having a general, state space form. In the past, system augmentation and GMRPT have only been applied to systems that can be formulated as second-order structural systems having mass and stiffness matrices. A particular formulation of SOD is also developed that can be used to compute a system's left-eigenvectors directly from its time series data. This is an advantage because it simplifies the process of performing GMRPT. This formulation of SOD also accounts for non-random excitations, which has not been done before. Finally, this work considers a system where the nonlinearity takes the form of a piecewise linear function. To deal with this type of nonlinearity, an alternate form of augmentation is proposed that may be beneficial when system nonlinearities are difficult or impossible to differentiate. All techniques are demonstrated using both simulation and physical systems in the form of analog circuits. This allows the reliability and effectiveness of system augmentation to be demonstrated in the context of real, physical systems.

5.2 Methodology

This section outlines the procedure for determining parametric variations in a dynamical system cast in a state space form using system augmentation and GMRPT. First, the general methodology of system augmentation is outlined. Second, the procedure for generating eigenvalues and right eigenvectors using DSPI is briefly reviewed. Third, the new procedure for generating left eigenvectors using SOD is presented. Finally, the basic steps involved in performing GMRPT to determine actual parameter variations, along with methods to improve accuracy and reduce noise, are reviewed.

5.2.1 System Augmentation

Certain types of nonlinear systems can be expressed in a state space form as

$$\dot{\mathbf{y}}(t) = \mathbf{A}_{sys}\mathbf{y}(t) + \mathbf{A}_{sys*}\mathbf{f}(\mathbf{y}(t)) + \mathbf{B}_{sys}\mathbf{v}(t), \tag{5.1}$$

where any system nonlinearities are contained within the $\mathbf{f}(\mathbf{y}(t))$ term. If each of the nonlinearities is instead represented by a new state variable in the vector $\mathbf{z}(t)$, then the system can be rewritten in augmented linear form as

$$\begin{aligned} \dot{\mathbf{y}}(t) &= \mathbf{A}_{sys}\mathbf{y}(t) + \mathbf{A}_{sys*}\mathbf{z}(t) + \mathbf{B}_{sys}\mathbf{v}(t), \\ \dot{\mathbf{z}}(t) &= \mathbf{A}_{aug}\mathbf{y}(t) + \mathbf{A}_{aug*}\mathbf{z}(t) + \mathbf{B}_{aug}\mathbf{w}(t), \end{aligned} \tag{5.2}$$

where $\mathbf{A}_{aug}$ and $\mathbf{A}_{aug*}$ are chosen by the user in forming the augmented system, and $\mathbf{w}(t)$ is prescribed to ensure that $\mathbf{z}(t) = \mathbf{f}(\mathbf{y}(t))$ for all t. Combining the states and inputs so that

$$\begin{aligned} \mathbf{x}(t) &= \begin{bmatrix} \mathbf{y}(t) \\ \mathbf{z}(t) \end{bmatrix}, \qquad \mathbf{A} = \begin{bmatrix} \mathbf{A}_{sys} & \mathbf{A}_{sys*} \\ \mathbf{A}_{aug} & \mathbf{A}_{aug*} \end{bmatrix}, \\ \mathbf{u}(t) &= \begin{bmatrix} \mathbf{v}(t) \\ \mathbf{w}(t) \end{bmatrix}, \qquad \mathbf{B} = \begin{bmatrix} \mathbf{B}_{sys} \\ \mathbf{B}_{aug} \end{bmatrix}, \end{aligned} \tag{5.3}$$

the overall augmented system can then be written in the standard state space form

$$\dot{\mathbf{x}}(t) = \mathbf{A}\mathbf{x}(t) + \mathbf{B}\mathbf{u}(t). \tag{5.4}$$

This augmented system model is linear in the extended state $\mathbf{x}(t)$ and hence amenable to modal analysis. A further example of the system augmentation process in the context of a specific dynamical system is presented in Section 5.4.1.

5.2.2 DSPI: Right Eigenvectors

DSPI makes use of a discrete-time autoregressive moving average (ARMA) model of a linear system to determine that system's right eigenvectors. The ARMA model is

given by

$$\begin{aligned}\dot{\mathbf{x}}(t) = &\mathbf{A_1}\mathbf{x}(t-1) + \cdots + \mathbf{A_p}\mathbf{x}(t-p) \\ &+ \mathbf{B_0}\mathbf{u}(t) + \mathbf{B_1}\mathbf{u}(t-1) + \cdots + \mathbf{B_{p-1}}\mathbf{u}(t-p+1) \\ &+ \mathbf{e}(t).\end{aligned} \tag{5.5}$$

Vector $\mathbf{x}(t)$ contains the measured states of the system, vector $\mathbf{u}(t)$ contains the measured inputs to the system, and $\mathbf{A_1}, \mathbf{A_2}, \ldots \mathbf{A_p}$ and $\mathbf{B_0}, \mathbf{B_1}, \ldots \mathbf{B_{p-1}}$ are sets of discrete time correlation matrices with respect to the states and inputs, respectively. Here p must be selected so that p times the number of measured states is greater than or equal to the total number of states in the system. When all of the L sampled time intervals for which equations having the form of Eq. (5.5) can be constructed are considered, they can be grouped in the compact form

$$\begin{aligned}\left[\begin{array}{cccc} \mathbf{x}(p+1) & \ldots & \mathbf{x}(p+L) \end{array}\right] = &\theta\Gamma \\ &+ \left[\begin{array}{cccc} \mathbf{e}(p+1) & \ldots & \mathbf{e}(p+L) \end{array}\right],\end{aligned} \tag{5.6}$$

where θ is given by

$$\theta = \left[\begin{array}{cccccc} \mathbf{A_1} & \ldots & \mathbf{A_p} & \mathbf{B_0} & \ldots & \mathbf{B_{p-1}} \end{array}\right], \tag{5.7}$$

and Γ is given by

$$\Gamma = \left[\begin{array}{ccc} \mathbf{x}(p) & \ldots & \mathbf{x}(p+L-1) \\ \vdots & & \vdots \\ \mathbf{x}(1) & \ldots & \mathbf{x}(L) \end{array}\right]. \tag{5.8}$$

Thus, using only the time series data in $\mathbf{x}(t)$ and $\mathbf{u}(t)$, the sets $[\mathbf{A_1}, \mathbf{A_2}, \ldots \mathbf{A_p}]$ and $[\mathbf{B_0}, \mathbf{B_1}, \ldots \mathbf{B_{p-1}}]$ in θ can be computed by using the pseudo-inverse in the expression

$$\theta = \left[\begin{array}{cccc} \mathbf{x}(p+1) & \ldots & \mathbf{x}(p+L) \end{array}\right] \Gamma^T(\Gamma\Gamma^T)^{-1}. \tag{5.9}$$

From the set $[\mathbf{A_1}, \mathbf{A_2}, \ldots \mathbf{A_p}]$ contained in θ it is then possible to compute the right

eigenvectors of the system using the matrix

$$\Theta = \begin{bmatrix} \mathbf{A_1} & \mathbf{A_2} & \dots & \mathbf{A_{p-1}} & \mathbf{A_p} \\ \mathbf{I} & \mathbf{0} & \dots & \mathbf{0} & \mathbf{0} \\ \mathbf{0} & \mathbf{I} & \dots & \mathbf{0} & \mathbf{0} \\ \vdots & \vdots & & \vdots & \vdots \\ \mathbf{0} & \mathbf{0} & \dots & \mathbf{I} & \mathbf{0} \end{bmatrix} \tag{5.10}$$

as is shown in detail in the literature [49, 50].

5.2.3 SOD: Left Eigenvectors

In the past, it has been difficult to calculate the left eigenvectors of a system for use in GMRPT. Here we formulate a procedure by which a system's left eigenvectors can be computed using SOD. This procedure is new in that it allows for a known, non-random input to the system. Such a non-random input is always present in an augmented system due to the augmented forcing. The procedure is shown for a system in state space form due to our focus on non-structural systems. However, it is equally applicable to systems having the second order form more common to structural dynamics. SOD considers the generalized eigenvalue problem

$$\mathbf{R}\Psi\Lambda^T = \mathbf{S}\Psi, \tag{5.11}$$

where Ψ is a square matrix containing eigenvectors as its columns, and Λ is a diagonal matrix of eigenvalues. If the matrices $\mathbf{R}$ and $\mathbf{S}$ are chosen so that

$$\mathbf{R} = \mathbf{x}\mathbf{x}^T, \tag{5.12}$$

$$\mathbf{S} = \mathbf{x}[\mathbf{D}\mathbf{x}^T - \mathbf{u}^T\mathbf{B}^T], \tag{5.13}$$

where $\mathbf{x}$ is the extended state as given in Section 5.2.1 and $\mathbf{D}$ is a difference operator, so that $\dot{\mathbf{x}}$ can be represented approximately by $\mathbf{x}\mathbf{D}^T$, then the eigenvalue problem of Eq. (5.11) can be rewritten as

$$\mathbf{x}\mathbf{x}^T\Psi\Lambda^T = \mathbf{x}[\mathbf{D}\mathbf{x}^T - \mathbf{u}^T\mathbf{B}^T]\Psi \tag{5.14}$$

Since $[\mathbf{D}\mathbf{x}^T - \mathbf{u}^T\mathbf{B}^T] = \mathbf{x}^T\mathbf{A}^T$ (compare with Eq. (5.4)), one can show that Eq. (5.11) is equivalent to

$$\Psi\Lambda = \mathbf{A}^T\Psi \tag{5.15}$$

for this choice of $\mathbf{R}$ and $\mathbf{S}$ when $\mathbf{x}\mathbf{x}^T$ is invertible and well-conditioned. Since Eq. (5.15) has the form of a standard left eigenvalue problem, this demonstrates that by using the time series data of the states and the inputs to compute the expressions in Eq. (5.12) and Eq. (5.13) and then solving the generalized eigenvalue problem given by Eq. (5.11), the left eigenvectors of the system matrix $\mathbf{A}$ can be found.

5.2.4 GMRPT: Parameter Variations

To identify the locations and extent of any parameter variations that occur in a system, GMRPT [43, 48] is utilized. For a system having the form of Eq. (5.4) and no variations, the right and left eigenvalue problems can be stated as

$$\mathbf{V}\Lambda - \mathbf{A}\mathbf{V} = \mathbf{0}, \tag{5.16}$$

$$\mathbf{U}\Lambda - \mathbf{A}^T\mathbf{U} = \mathbf{0}, \tag{5.17}$$

where Λ is the diagonal matrix of eigenvalues, and $\mathbf{V}$ and $\mathbf{U}$ are the right and left eigenvector matrices, respectively. If one is able to generate a complete set of either right or left eigenvectors and accompanying eigenvalues, then Eq. (5.16) or Eq. (5.17), respectively, can be used to estimate $\mathbf{A}$ directly and identify any parameter variations that may occur. However, for many systems obtaining this type of complete information is impossible and GMRPT or some other update method is necessary. If the system parameters change so that the varied system matrix can be represented as the original matrix $\mathbf{A}$ minus some variation $\delta\mathbf{A}$, then the new eigenvalue problems for the system are defined by

$$\mathbf{V}_d\Lambda_d - (\mathbf{A} - \delta\mathbf{A})\mathbf{V}_d = \mathbf{0}, \tag{5.18}$$

$$\mathbf{U}_d\Lambda_d - (\mathbf{A} - \delta\mathbf{A})^T\mathbf{U}_d = \mathbf{0}, \tag{5.19}$$

where the subscript d implies that the eigenvalues and eigenvectors are associated with the varied system. These equations can be rearranged to separate the variation matrices $\delta\mathbf{A}$ so that

$$\mathbf{D} = \delta\mathbf{A}\mathbf{V}_d = \mathbf{V}_d\Lambda_d - \mathbf{A}\mathbf{V}_d, \tag{5.20}$$

$$\mathbf{C} = \delta\mathbf{A}^T\mathbf{U}_d = \mathbf{U}_d\Lambda_d - \mathbf{A}^T\mathbf{U}_d, \tag{5.21}$$

where $\mathbf{D}$ and $\mathbf{C}$ are defined as the right and left variation matrices, respectively. As Eq. (5.20) and Eq. (5.21) indicate, these variation matrices can be computed so long as the parameters in the original system model $\mathbf{A}$ are known and some of the right and left eigenvectors of the varied system are accessible. The number of right and left eigenvectors that must be determined is equal to the rank of $\delta\mathbf{A}$. Sections 5.2.2 and 5.2.3 demonstrate how this eigenvector information can be determined using the state and input time series. The variation matrices $\mathbf{D}$ and $\mathbf{C}$ can then be used in the equation

$$\delta\mathbf{A} = \mathbf{D}(\mathbf{C}^T\mathbf{V}_d)^{-1}\mathbf{C}^T \tag{5.22}$$

to determine the system parameter variations, where the number of vectors included in $\mathbf{D}$ and $\mathbf{C}$ is again equal to the rank of $\delta\mathbf{A}$. Performance can sometimes be improved by slightly modifying the procedure and including additional modes in $\mathbf{D}$ and $\mathbf{C}$. Subspace selection can then be employed, whereby only select parts of the eigenvector space are used in estimating parameter changes; this is presented in more detail by D'Souza et al. [48]. Noise reduction is also possible [53], although in this work we found it to only be reliable with SOD; DSPI seemed to be less effective when paired with the noise reduction algorithm.

5.3 Systems

To demonstrate the applicability of system augmentation techniques to general, nonlinear dynamical systems in state space form, three familiar systems that can be physically represented by analog circuits were selected. The first of these systems is the well-known Duffing oscillator, which is given by the equations

$$\begin{aligned} \dot{x} &= y, \\ \dot{y} &= -by - k_1 x - k_3 x^3 + \gamma \sin \omega t, \end{aligned} \tag{5.23}$$

where x and y are state variables, and γ, b, k_1, k_3, and ω are system parameters. This system can be physically realized through the analog circuit [90] shown schematically in Fig. 5.1 and as constructed in Fig. 5.2. The value of the components in this figure are given in Table 5.1. The potentiometers labelled P1–P3 allow control of b, k_1, and k_3, while γ and ω can be varied through the function generator responsible for the input signal. In all of the circuits presented, the operational amplifiers (op-amps) are

model TL082 and the multipliers are model AD633.

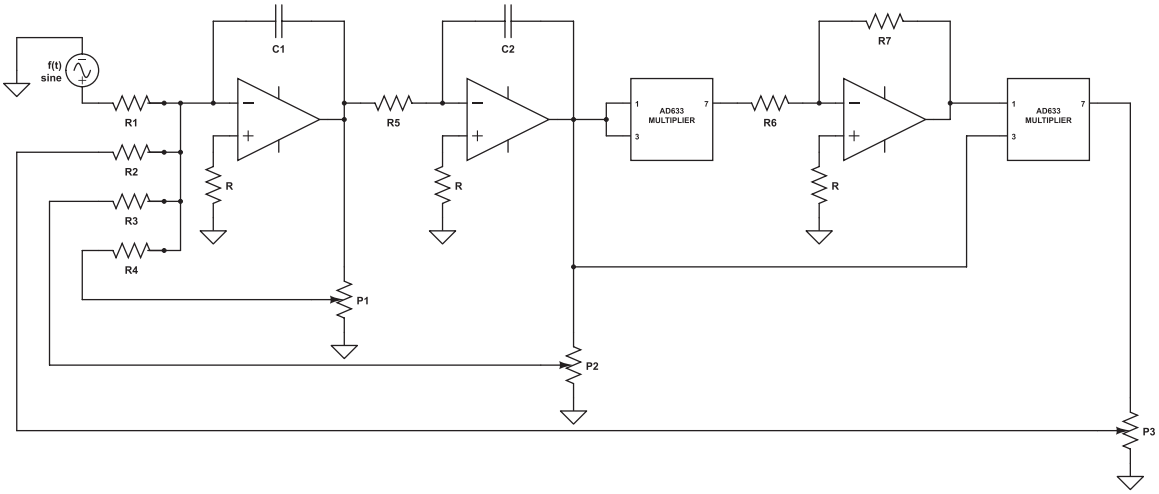

Figure 5.1: Schematic for an analog circuit realization of the Duffing oscillator.

The Rossler system is another familiar nonlinear dynamical system. Its equations are given by

$$\begin{aligned} \dot{X} &= -Y - Z, \\ \dot{Y} &= X + A_R Y, \\ \dot{Z} &= B_R + XZ - C_R Y. \end{aligned} \tag{5.24}$$

This system can also be realized as an analog circuit, as shown schematically in Fig. 5.3 and as constructed in Fig. 5.4. In this circuit, the system variables of Eq. (5.24) have been halved (i.e. $x = X/2$, etc.) so that the voltages will lie within $\pm$10V. The resulting equations are

$$\begin{aligned} \dot{x} &= -y - z, \\ \dot{y} &= x + a_R y, \\ \dot{z} &= b_R + 2z(x - c_R), \end{aligned} \tag{5.25}$$

where $a_R = A_R$, $b_R = B_R/2$, and $c_R = C_R/2$. The component values for this circuit are shown in Table 5.2. The potentiometer Pa allows for adjustment of the parameter a_R, while b_R and c_R are controlled by adjusting input voltages. This is accomplished through the use of potentiometers not shown in the circuit diagram.

The final system of interest is a jerk circuit proposed by Sprott [91, 92] and fully developed in the form used in this work by Kiers et al. [93, 94]. This circuit has the

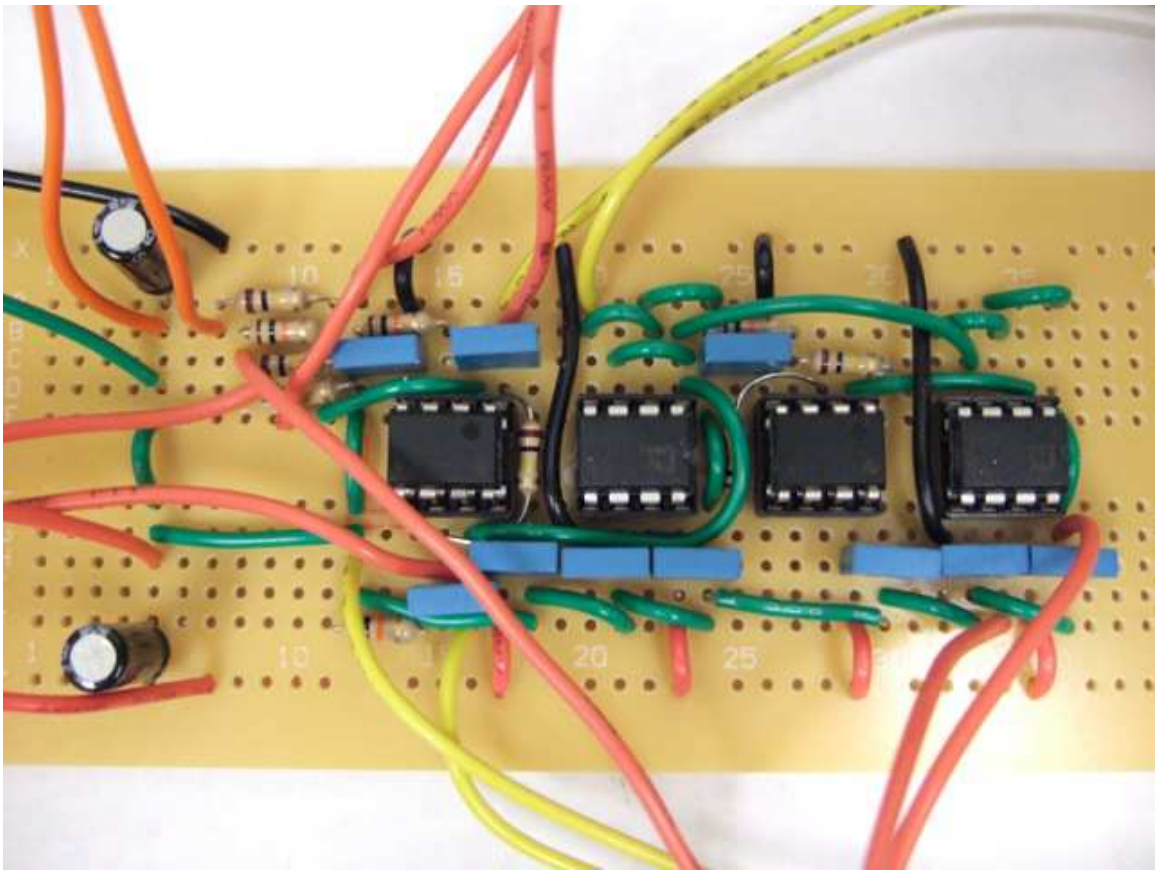

Figure 5.2: The Duffing circuit as constructed in the laboratory.

Table 5.1: Duffing circuit component values

Component	Value
R	10 kΩ
R1	100 kΩ
R2	10 kΩ
R3	100 kΩ
R4	100 kΩ
R5	100 kΩ
R6	10 kΩ
R7	100 kΩ
P1	1 kΩ pot
P2	1 kΩ pot
P3	1 kΩ pot
C1	10 nF
C2	10 nF

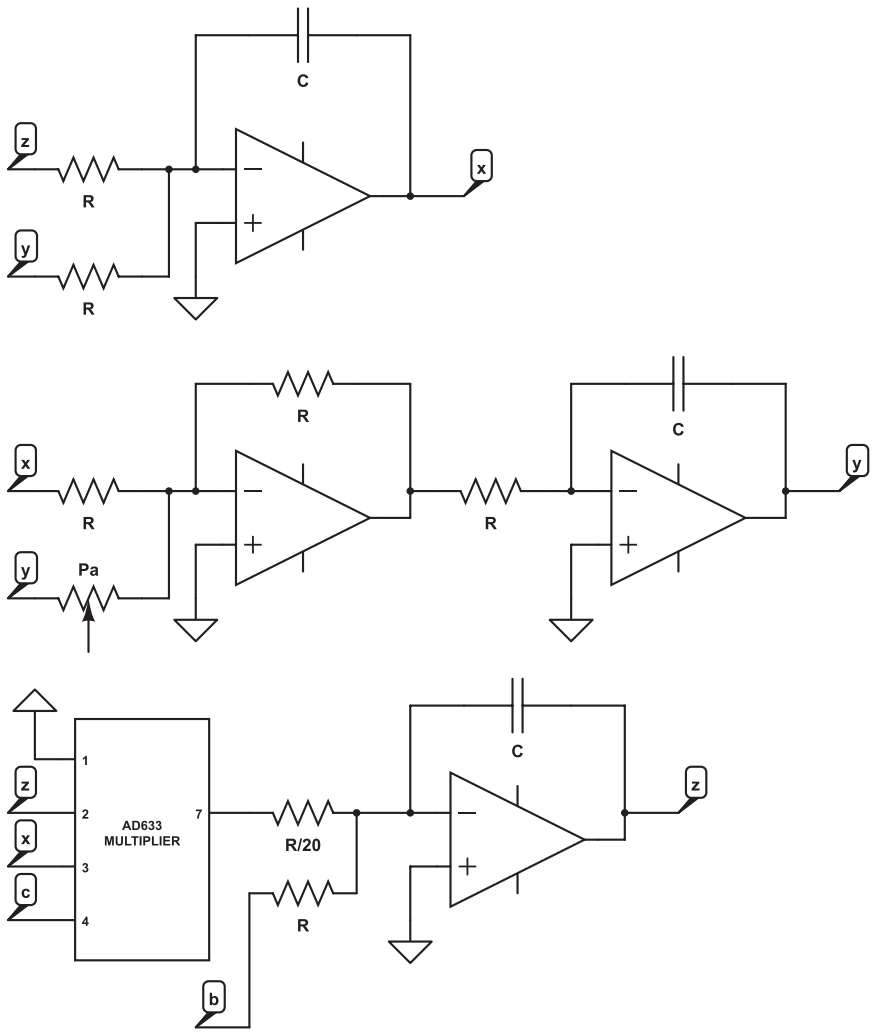

Figure 5.3: Schematic for an analog circuit realization of the Rossler system.

Table 5.2: Rossler circuit component values

Component	Value
R	10 kΩ
Pa	100 kΩ pot
C	100 nF

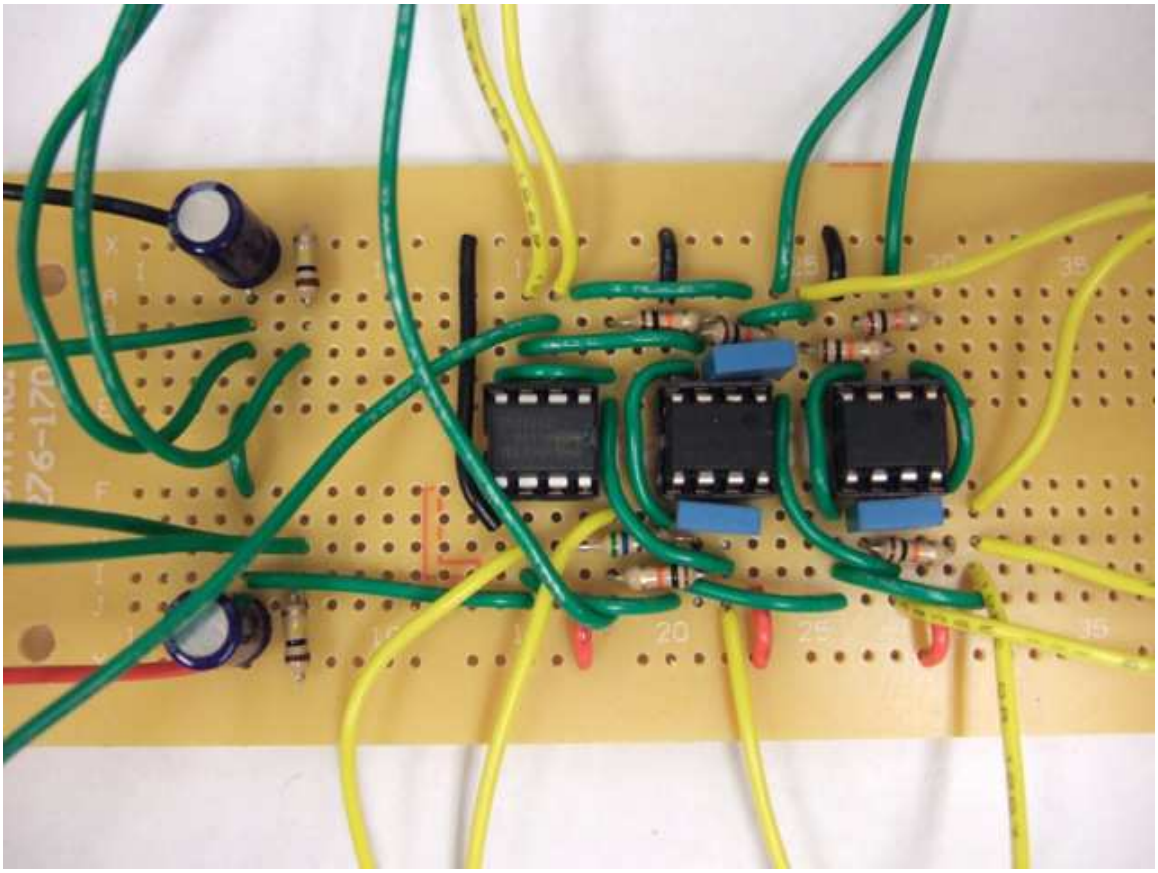

Figure 5.4: The Rossler circuit as constructed in the laboratory.

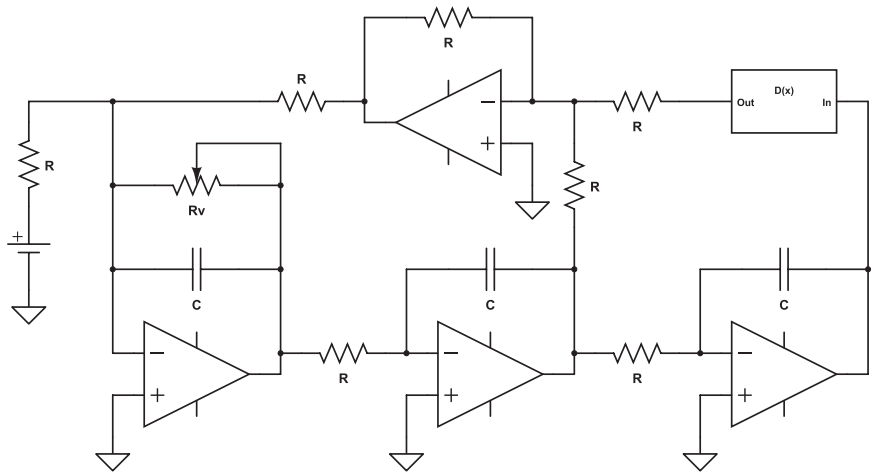

Figure 5.5: Schematic for an analog circuit realization of the general jerk system.

Table 5.3: Jerk circuit component values

Component	Value
R	1 kΩ
R1	560 Ω
R2	5 kΩ pot
Rv	5 kΩ pot
C	1 μF

general state space form

$$\begin{aligned} \dot{x} &= y, \\ \dot{y} &= z, \\ \dot{z} &= -A_J z + y + D_J(x) - C_J, \end{aligned} \tag{5.26}$$

where x, y, and z are states representing the system position, velocity, and acceleration, respectively, and A_J and C_J are parameters. $D_J(x)$ is the system nonlinearity, which can take on several forms depending on the kind of system in which one is interested. For this work, the nonlinearity given by $D_J(x) = B_J \min(x, 0)$ [94] is considered, where B_J is a parameter. The general circuit can be constructed as shown in the schematic of Fig. 5.5. The specific piecewise nonlinearity we have chosen to use is shown in Fig. 5.6. The component listing for the circuit as a whole is given in Table 5.3. Images of the physical circuit and its enclosure are presented in Fig. 5.7.

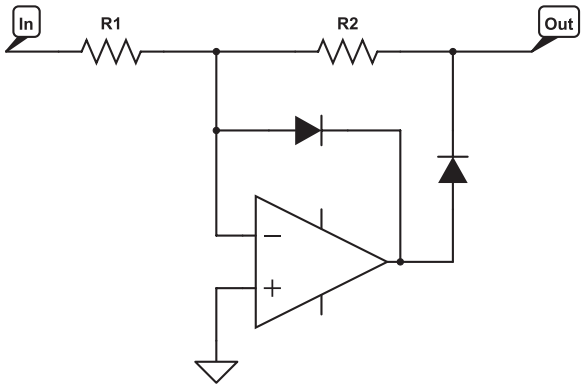

Figure 5.6: An analog realization of the specific piecewise nonlinearity $D(x) = B_J \min(x, 0)$.

(a) (b)

Figure 5.7: The jerk circuit and its enclosure as constructed in the laboratory.

5.4 Results and Discussion

In this section, results generated using both simulation and experimental data are discussed. An emphasis is placed on analyzing when good results can be expected from GMRPT, and possible options to pursue when having difficulty with a given system.

5.4.1 Example of the System Augmentation Process

To provide additional clarity regarding the system augmentation process outlined in Section 5.2.1 a specific example of system augmentation is provided here for the Rossler system. In the original system given by Eq. (5.24) the system nonlinearity has the form xz. One can choose to replace this nonlinearity with the new variable s given by

$$\begin{aligned} s &\triangleq xz, \\ \dot{s} &\triangleq \dot{x}z + z\dot{z}. \end{aligned} \tag{5.27}$$

An equation that describes the evolution of s will then take the form

$$\dot{s} = a_1 x + a_2 y + a_3 z + a_4 s + g(t), \tag{5.28}$$

where $a_{1...4}$ are constants of the user's choosing. For instance, $a_1 = -1$, $a_2 = 10$,$a_3 = 20$, and $a_4 = -1$ might be chosen. Equation (5.28) can be rearranged to read

$$g(t) = \dot{s} - a_1 x - a_2 y - a_3 z - a_4 s \tag{5.29}$$

for use in calculating the prescribed forcing. Thus, as data is collected, it will be used first in Eq. (5.27) to calculate the augmented variable s and its derivative $\dot{s}$. Then it, in conjunction with the augmented variable, will be used in Eq. (5.28) to find the augmented forcing $g(t)$. All of this information can then be passed on for further processing by an algorithm such as DSPI or SOD.

5.4.2 Simulation Data

In general, system augmentation in combination with GMRPT will work extremely well for simulated systems, particularly when those simulations lack any noise. For instance, in the Duffing system, where the nominal system parameters are given as $\gamma = 0.4$, $b = 0.5$, $k_1 = -1$, $k_3 = 1$, and $\omega = 1$, if k_1 and k_3 are allowed to independently vary over some range, we can achieve results using GMRPT as shown in Table 5.4

Table 5.4: Duffing simulation results for Δk_1

Actual Δk_1	Δk_1 via GMRPT
0	-0.005
0.05	0.058
0.10	0.110
0.15	0.158
0.20	0.209
0.25	0.273
0.30	0.329

and Table 5.5. Any system parameters which were not varied, with the exception of the augmented ones (which are known to be zero), showed estimated changes of less than 0.01. The one exception to this was in the case when $\Delta k_1 = 0.3$, when an error of just less than 0.04 occurred. Here the data was collected for a time step of 0.01 and 5,000 samples were obtained. The augmentation is selected, without any particular attempt at optimization, to have the form

$$\ddot{s} = x - 5s + g(t), \tag{5.30}$$

with the augmented variable given by $s = x^3$. Here $g(t)$ is the augmented forcing, which must be calculated at each time step. This calculation makes use of the subspace selection process for a single parameter variation. The reconstruction of the parameter variations is very successful because one can find the left and right eigenvectors of the augmented system very accurately in the absence of noise. Note that the accuracy in the absence of noise can be improved even further by reducing the time step and increasing the number of samples.

Similar successful results are possible for all three of the systems, but here we will dwell only on the jerk system because it offers the opportunity to present a new methodology for augmenting a system. Typically, a system is augmented as in Eq. (5.30), where the nonlinearity is replaced by a new variable (i.e., s). The variable s and some differentiation of it (i.e., $\dot{s}$) are combined with components of the extended state to construct the augmented equations. This works well, but poses a problem if the system nonlinearities are difficult to differentiate. In the case of the jerk system, where the nonlinearity is given by $D_J(x) = B_J \min(x, 0)$, we can only differentiate once with respect to time in closed form. With other forms of

Table 5.5: Duffing simulation results for Δk_3

Actual Δk_3	Δk_3 via GMRPT
0	-0.005
-0.05	-0.050
-0.10	-0.094
-0.15	-0.145
-0.20	-0.194
-0.25	-0.243
-0.30	-0.290

nonlinearity, even a first differentiation may be impossible [48]. In the context of the jerk system we therefore propose a new way of forming the augmentation that is amenable to nonlinearities that are difficult to differentiate. Previously, the jerk system may have been augmented using a set of equations such as the one given below

$$\begin{aligned} s &\triangleq \min(x, 0), \\ \dot{s} &\triangleq \dot{x}/2 - \text{sign}(x1)\dot{x}/2, \\ \dot{s} &= -x - y - z - s + g(t). \end{aligned} \tag{5.31}$$

However, the system can also be augmented by using a form such as

$$\begin{aligned} \dot{s} &\triangleq \min(x, 0) - \alpha s, \\ s &\triangleq \int \dot{s}\, \mathrm{d}t, \\ \dot{s} &= -x - y - z - s + g(t), \end{aligned} \tag{5.32}$$

where α is a parameter carefully chosen to ensure stability of the integration. The αs term is included to keep the integration bounded in cases where the nonlinearity does not switch signs, as is true here. There is little difference in results produced by these two different augmentations in this case, but the idea is useful for nonlinearities that are not differentiable. In the jerk system, the nominal system parameters are chosen as $A_J = 0.5$, $B_J = 6$, and $C_J = 0.5$. If A_J and B_J are allowed to vary simultaneously over some range, using GMRPT we can achieve the results shown in Table 5.6. Here the data was collected for a time step of 0.01 and 5,000 samples were obtained as in the previous cases.

These results show that two simultaneous parameter changes of somewhat different

Table 5.6: Jerk simulation results for ΔA and ΔB

Actual ΔA	*Actual*ΔB	ΔA via GMRPT	ΔB via GMRPT
0	0	-0.011	0.026
0	0.25	0.002	0.259
0	0.5	0.000	0.500
0.1	0	0.058	0.031
0.1	0.25	0.071	0.245
0.1	0.5	0.142	0.516

magnitudes may be difficult to distinguish accurately using GMRPT, but overall the method still works well. The accuracy of the results is primarily dependent on DSPI and SOD computing the right and left eigenvectors of the system accurately, and, secondarily, with the DSPI and SOD estimates agreeing with each other. This can be compromised significantly by noise. In these investigations, if Gaussian white noise was added to the systems with a signal to noise ratio of 1,000 or less, it became very difficult to recover the parameter variations successfully.

5.4.3 Experimental Data

The Duffing circuit considered has the same nominal parameters and augmentation as in the simulations (Section 5.4.2). For the circuit presented in Fig. 5.1, 160 Hz is equivalent to $\omega = 1$. Data is sampled at 100 kHz and over a million time points are collected per set. This data is also low-pass filtered using a filter with a corner frequency of 2000 Hz to remove the effects of high frequency noise. An example of the time series data collected is shown in Fig. 5.8. As in the simulations, one of the parameters is selected for variation and results such as those shown in Table 5.7 can be generated. Here, the noise reduction technique [53] has been applied to the SOD data in addition to using the appropriate subspace selection techniques.

Although these results are less accurate than the comparable values generated using simulations, the trend of the changes is well captured by the estimates and the individual estimates themselves are reasonable. The maximum error made in estimating changes to other parameters that did not actually occur was 0.028, although in most cases this value was much lower. In these results, as with most of the experimental work performed, GMRPT tended to perform poorly when the parameter variations were small and improved when they were larger. This is expected, since

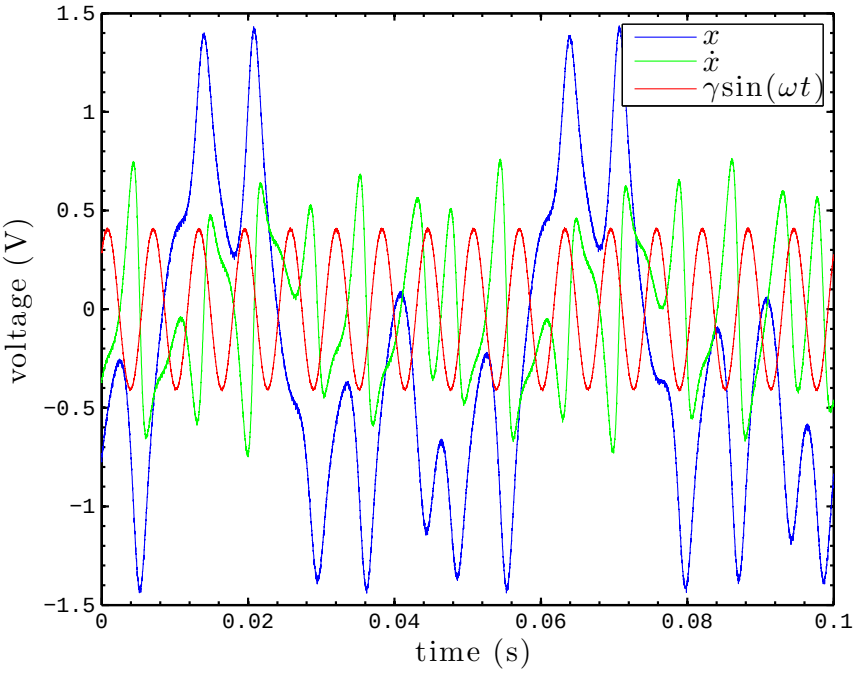

Figure 5.8: An example of time series data collected from the Duffing circuit.

Table 5.7: Duffing circuit experimental results for Δk_3

Actual Δk_3	Δk_3 via GMRPT
0	-0.056
-0.05	-0.092
-0.10	-0.078
-0.125	-0.123
-0.15	-0.157
-0.175	-0.195
-0.20	-0.231

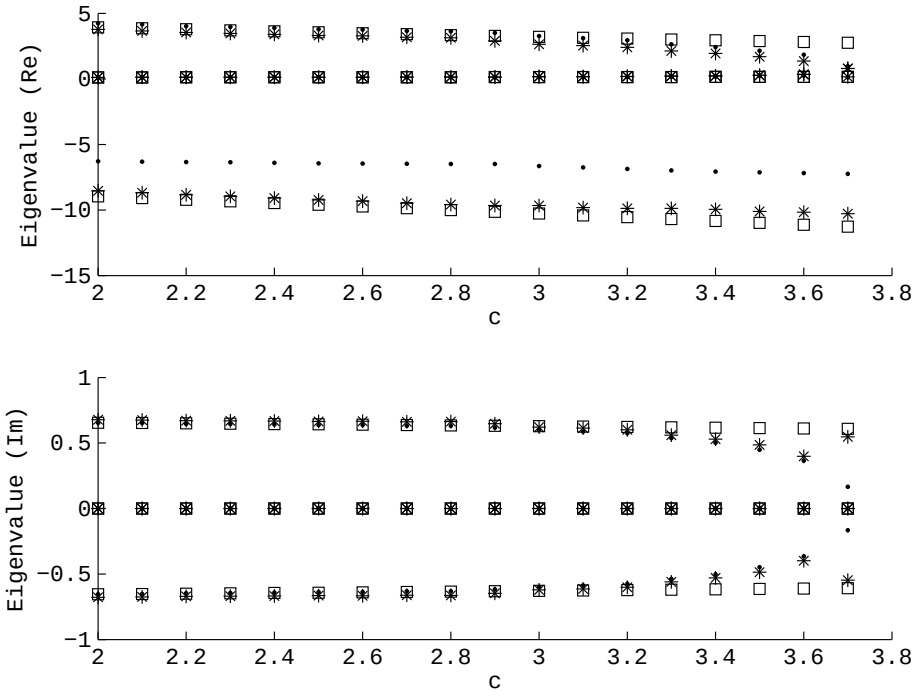

Figure 5.9: Rossler circuit eigenvalues versus the parameter c_R.

changes in the modal properties of the system for small changes in in the system itself are of the order of the accuracy of determining the modal properties of the system.

The Rossler circuit presented challenges in generating good results experimentally. The parameter ranges where we tried to predict parameter changes saw many bifurcations between limit cycle and chaotic behavior. It also seemed difficult to accurately capture all of the eigenvalues of the augmented system due to large differences in the time scales involved in the system. Figure 5.9 shows that DSPI in particular can struggle with making accurate eigenvalue predictions. In the figure, the $\square$ symbols are used to represent the analytically calculated eigenvalues, the $\bullet$ symbols are used to represent DSPI's estimates, and the $*$ symbols are used to represent SOD's estimates. Due to these difficulties, we were unable to generate reliable results for this system.

The jerk system, however, produced good results. An example of the time series data collected is shown in Fig. 5.10. Some results are given in Table 5.8. Again, most of the parameter values which were not changed showed relatively low error in the form of false change predictions. Also, estimation generally improved as the parameter change grew larger.

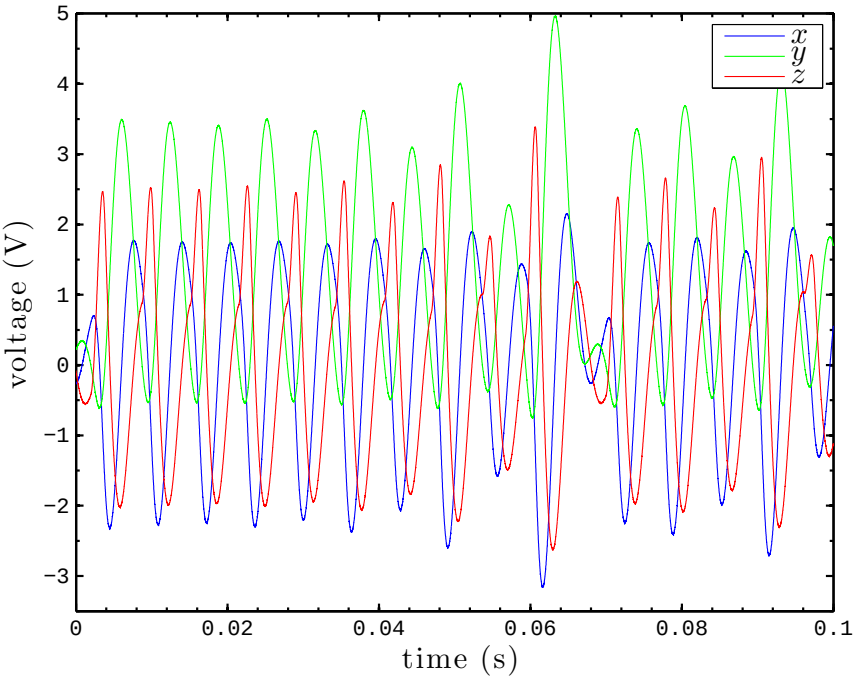

Figure 5.10: An example of time series data collected from the jerk circuit.

Table 5.8: Jerk circuit experimental results for ΔA_J

Actual ΔA_J	ΔA_J via GMRPT
0	-0.013
-0.041	-0.055
-0.071	-0.063
-0.106	-0.181
-0.125	-0.126
-0.167	-0.159
-0.190	-0.182
-0.214	-0.207
-0.241	-0.225

5.5 Conclusions

We have shown that system augmentation in conjunction with GMRPT can be applied to general dynamical systems in state space form for the purpose of detecting parameter variations. We have presented an alternate way of performing the actual system augmentation that allows systems with non-differentiable nonlinearities that, if integrated directly, would case drift, to be treated within the system augmentation framework. We have also shown how SOD can be used to extract left-eigenvector information from system time series data, which makes localization of parameter variations using GMRPT much easier. Our application of these methods to real physical systems shows that these techniques are practical. System augmentation itself is a reliable method for treating nonlinearities within a linear framework. In fact, when all of the eigenvalues and eigenvectors in Eq. (5.16) or Eq. (5.17) are available, a full reconstruction of $\mathbf{A}$ is often more accurate than GMRPT. This suggests that alternative methods of identifying the parameter variations may be desirable. GMRPT seems sensitive to small disagreements between the left and right eigen-information as generated by the two methods employed herein. Thus, if alternate techniques for eigenvalue and eigenvector estimation or some way to reconcile the right and left information could be developed, GMRPT would be that much more robust.

CHAPTER 6

Conclusions and Future Work

This dissertation further develops several techniques for identifying parameter variations in nonlinear dynamical systems. Two overarching methodologies are presented: SVFs in Chapters 2–4 and system augmentation in Chapter 5. In some ways, these two methodologies approach the same problem from opposite tacks. Using SVFs, the investigator seeks to exploit existing system nonlinearities (or perhaps introduce new nonlinearities via feedback) in order to better examine changes in attractor geometry and thereby determine any parameter variations. Using system augmentation, on the other hand, the investigator seeks to recast a system having nonlinearities within a larger, linear framework so that familiar tools from modal analysis are applicable and any parameter variations are reflected in changes to the augmented system's eigenvalues and eigenvectors. Rather than recapitulate some of the more specific conclusions stated in the preceding chapters, the contributions of this dissertation are summarized in Section 6.1. Section 6.2 outlines directions for future work.

6.1 Contributions

In general, the work presented in this dissertation develops the ideas of SVFs and system augmentation into tools that can be used in real, physical systems. It does so via the following contributions:

- In Chapter 2, a parametric study is presented which determines factors critical to making the best use of SVFs in identifying parameter variations. Specifically, it examines the impact the system dynamics, attractor characteristics, and choices made in SVF construction (such as the length of time allowed for trajectory divergence when generating SVs), have on the resulting SVF. The simulation-based findings suggest that having chaotic dynamics is only helpful

for generating optimal SVFs when the evolution time is long; for short evolution times, limit cycle behavior can actually produce larger magnitude SVs. However, these limit cycle SVs may be difficult to realize in a physical system because of a lack of coincident states between data sets. This chapter also explores the use of nonlinear feedback to alter a dynamical system in order to maximize SVF sensitivity. Two forms of feedback, one of fixed polynomial form and the other based on an interpolated spline surface, are implemented to generate the feedback. They are both shown to be effective in improving SVF sensitivity. However, the system attractors selected through feedback optimization are often near bifurcation points or stability boundaries, where SVFs may also be difficult to realize in physical systems.

- Chapter 3 presents a methodology for constructing SVFs in embedded coordinates, which is important for using SVFs in physical systems. Previously, it has only been possible to construct SVFs for a given dynamical system when a full set of state variables is available. This severely restricts SVF applicability because it may be cost prohibitive, or even impossible, to measure the entire state of high-dimensional systems. Thus, Chapter 3 presents a method for constructing SVFs with only partial state information by using time-delay coordinate embeddings. Local models are employed in which the embedded states of a neighborhood are weighted in a novel way referred to as embedded point cloud averaging. Application of the methodology to both simulated and experimental time series prove its utility and reliability.

- The ultimate goal in developing SVFs is that they would find use in practical systems and devices. In Chapter 4, initial steps towards realizing this goal using a fluidic micro-sensor are outlined. Two designs for an immersed micro-plate that would vibrate rotationally about an axis as fluid flows past it in a microchannel are presented. Fluid-structure interaction simulations established that these architectures would not experience sustained vibration from the excitation provided by the fluid flow alone. However, despite the fact that the system as designed would have limited effectiveness as a sensor, it provided a test case to which the feedback optimization techniques of Chapter 2 could be applied.

- Chapter 5 extends past work on system augmentation by demonstrating how left eigenvectors can be extracted from time series data using smooth orthogonal decomposition (SOD). This enables generalized minimum rank perturbation

theory (GMRPT) to be more easily applied to non-symmetric systems. Additionally, a new approach to generating the augmented variables is proposed that may be advantageous when dealing with systems whose nonlinearities are non-differentiable. For the first time, system augmentation is performed experimentally by using a variety of nonlinear circuits. Experimental results, along with results from simulations, demonstrate that the system augmentation methodology is effective.

6.2 Future Work

The following are suggested areas for continuing research into SVFs and system augmentation:

- One of the drawbacks of current SVF techniques is their requirement of coincident states between data sets that can serve as the initial conditions for diverging trajectories. In many instances, there are no such states. This drawback can, to some extent, be alleviated by local modeling (such as was carried out in constructing SVFs in coordinate embeddings). However, even in the case of chaotic dynamics, the power of local modeling is limited and as a result some portion of the attractor will remain unsuitable for generating SVs. This problem is exacerbated for other types of attractors, such as limit cycles, where, depending on the parameter variation of interest, it may be impossible to construct any SVs at all. For this reason, a method that examines attractor deformation geometrically, independent of the precise states of the nominal and varied data sets, would be beneficial. Only one prior work [95] has taken this approach by looking at how the moments of groups of data points belonging to a Poincaré section change with system parameter variations. It seems plausible that by coupling image processing and pattern recognition techniques [96] with small numbers of representative points from the dynamical system's trajectories, it may be possible to divorce measurements of attractor deformation from any requirement on the existence of matched states between the data sets of interest.

- Another characteristic of SVFs, which is undoubtedly a strength when detecting multiple simultaneous variations, is that they are fields composed of many vectors. However, this characteristic can also be a weakness because it means that a choice must be made when adjusting feedback or available system parameters

to optimize SVFs. Is the optimization designed to maximize the sensitivity of the SVs on average? Some fraction of the best performing SVs? Only the best SV? In many circumstances, not all of the information the SVF provides may be needed. Instead, more frequent updates of the best performing SVs might be of interest. Acquiring this type of information may be possible by using targeting control [60, 61] in conjunction with SVFs to repeatedly visit only the regions of state space critical for generating the selected SVs.

- System augmentation as presented herein is an effective methodology. However, it relies on having knowledge of the entire state. If there were a way to achieve system augmentation with limited knowledge of the state, either through some type of state estimation or via time-delay embedded coordinates, this methodology could be applied to even more systems. Determining how best to work with limited state data in the context of system augmentation is an area of potential exploration.

- System augmentation has been successfully used with circuits to experimentally determine parameter changes. It is an open question how well this success translates to electro-mechanical systems, such as vibrating beams instrumented with piezoelectric devices, where noise levels may be higher and multiple modes of vibration may interact. Further investigation in this vein could extend to other coupled systems involving multi-physics, such as those with fluid or electromagnetic forces.

BIBLIOGRAPHY

[1] Doebling, S. W., Farrar, C. R., Prime, M. B., and Shevitz, D. W., "Damage identification and health monitoring of structural and mechanical systems from changes in their vibration characteristics: a literature review," Tech. rep., Los Alamos National Laboratory, 1996.

[2] Doebling, S. W., Farrar, C. R., and Prime, M. B., "A summary review of vibration-based damage identification methods," *The Shock and Vibration Digest*, Vol. 30, No. 2, 1998, pp. 91–105.

[3] Kim, H. M. and Bartkowitz, T. J., "Damage detection and health monitoring of large space structures," *Proceedings of AIAA Structures, Structural Dynamics, and Materials Conference*, 1993, pp. 3527–3533.

[4] Atalla, M., "On model updating using neural networks," *Mechanical Systems and Signal Processing*, Vol. 12, No. 1, 1998, pp. 135–161.

[5] Marwala, T. and Hunt, H. E. M., "Fault identification using finite element models and neural networks," *Mechanical Systems and Signal Processing*, Vol. 13, No. 3, 1999, pp. 475–490.

[6] Sohn, H. and Farrar, C. R., "Damage diagnosis using time series analysis of vibration signals," *Smart Materials and Structures*, Vol. 10, No. 3, 2001, pp. 446–451.

[7] Amaravadi, V., Rao, V., Koral, L. R., and Derriso, M. M., "Structural health monitoring using wavelet transforms," *Proceedings of SPIE*, Vol. 4327, 2001, pp. 258–269.

[8] Amizic, B., "Two-dimensional wavelet mapping techniques for damage detection in structural systems," *Proceedings of SPIE*, Vol. 4693, 2002, pp. 267–278.

[9] Weinberg, M. S., Dube, C. E., Petrovich, A., and Zapata, A. M., "Fluid damping in resonant flexural plate wave device," *Journal of Microelectromechanical Systems*, Vol. 12, No. 5, 2003, pp. 567–576.

[10] Braun, T., Barwich, V., Ghatkesar, M., Bredekamp, A., Gerber, C., Hegner, M., and Lang, H., "Micromechanical mass sensors for biomolecular detection in a physiological environment," *Physical Review E*, Vol. 72, No. 3, 2005, pp. 1–9.

[11] Vignola, J. F. and Judge, J. A., "Architectural considerations of micro- and nanoresonators for mass detection in the presence of a fluid," *Journal of Applied Physics*, Vol. 104, No. 12, 2008, pp. 124305–111124305–8.

[12] Judge, J. A., Vignola, J. F., and Jarzynski, J., "Dissipation from microscale and nanoscale beam resonators into a surrounding fluid," *Applied Physics Letters*, Vol. 92, No. 12, 2008, pp. 124102–1–124102–3.

[13] Hwang, K. S., Lee, S.-M., Kim, S. K., Lee, J. H., and Kim, T. S., "Micro and nanocantilever devices and systems for biomolecule detection," *Annual Review of Analytical Chemistry*, Vol. 2, 2009, pp. 77–98.

[14] Yang, Y. T., Callegari, C., Feng, X. L., Ekinci, K. L., and Roukes, M. L., "Zeptogram-scale nanomechanical mass sensing," *Nano letters*, Vol. 6, No. 4, 2006, pp. 583–6.

[15] Burg, T. P., Mirza, A. R., Milovic, N., Tsau, C. H., Popescu, G. A., Foster, J. S., and Manalis, S. R., "Vacuum-packaged suspended microchannel resonant mass sensor for biomolecular detection," *Journal of Microelectromechanical Systems*, Vol. 15, No. 6, 2006, pp. 1466–1476.

[16] Burg, T. P., Godin, M., Knudsen, S. M., Shen, W., Carlson, G., Foster, J. S., Babcock, K., and Manalis, S. R., "Weighing of biomolecules, single cells and single nanoparticles in fluid," *Nature*, Vol. 446, 2007, pp. 1066–1069.

[17] Nichols, J. M., Trickey, S. T., Todd, M. D., and Virgin, L. N., "Structural health monitoring through chaotic interrogation," *Meccanica*, Vol. 38, 2003, pp. 239–250.

[18] Todd, M. D., Erickson, K., Chang, L., Lee, K., and Nichols, J. M., "Using chaotic interrogation and attractor nonlinear cross-prediction error to detect fastener preload loss in an aluminum frame," *Chaos*, Vol. 14, No. 2, 2004, pp. 387–99.

[19] Torkamani, S., Butcher, E. A., Todd, M. D., and Park, G., "Detection of system changes due to damage using a tuned hyperchaotic probe," *Smart Materials and Structures*, Vol. 20, 2011, pp. 025006–1–025006–16.

[20] Torkamani, S., Butcher, E. A., Todd, M. D., and Park, G., "Hyperchaotic probe for damage identification using nonlinear prediction error," *Mechanical Systems and Signal Processing*, Vol. 29, 2012, pp. 457–473.

[21] Chelidze, D., Cusumano, J. P., and Chatterjee, A., "A dynamical systems approach to damage evolution tracking, part 1: description and experimental application," *Journal of Vibration and Acoustics*, Vol. 124, No. 2, 2002, pp. 250–257.

[22] Cusumano, J. P., Chelidze, D., and Chatterjee, A., "A dynamical systems approach to damage evolution tracking, part 2: model-based validation and physical interpretation," *Journal of Vibration and Acoustics*, Vol. 124, No. 2, 2002, pp. 258–264.

[23] Chatterjee, A., Cusumano, J. P., and Chelidze, D., "Optimal tracking of parameter drift in a chaotic system: experiment and theory," *Journal of Sound and Vibration*, Vol. 250, No. 5, 2002, pp. 877–901.

[24] Chelidze, D. and Cusumano, J. P., "A dynamical systems approach to failure prognosis," *Journal of Vibration and Acoustics*, Vol. 126, No. 1, 2004, pp. 2–8.

[25] Chancellor, R. S., Alexander, R. M., and Noah, S. T., "Detecting parameter changes using experimental nonlinear dynamics and chaos," *Journal of Vibration and Acoustics*, Vol. 118, No. 3, 1996, pp. 375–383.

[26] Yin, S. and Epureanu, B., "Enhanced nonlinear dynamics and monitoring bifurcation morphing for the identification of parameter variations," *Journal of Fluids and Structures*, Vol. 21, 2005, pp. 543–559.

[27] Yin, S.-H. and Epureanu, B. I., "Nonlinear feedback excitation for system interrogation by bifurcation morphing," *AIAA Journal*, Vol. 46, No. 8, 2008, pp. 2058–2065.

[28] Cusumano, J. P. and Chatterjee, A., "Steps towards a qualitative dynamics of damage evolution," *International Journal of Solids and Structures*, Vol. 37, No. 44, 2000, pp. 6397–6417.

[29] Feeny, B., Yuan, C. M., and Cusumano, J. P., "Parametric identification of an experimental magneto-elastic oscillator," *Journal of Sound and Vibration*, Vol. 247, No. 5, 2001, pp. 785–806.

[30] Hashmi, A. I. and Epureanu, B. I., "Sensitivity vector fields for damage detection and sensing," *Proceedings of SPIE*, Vol. 5765, 2005, pp. 236–244.

[31] Hashmi, A. I. and Epureanu, B. I., "Sensitivity resonance and attractor morphing quantified by sensitivity vector fields for parameter reconstruction," *Nonlinear Dynamics*, Vol. 45, No. 3-4, 2006, pp. 319–335.

[32] Yin, S.-H. and Epureanu, B. I., "Structural health monitoring based on sensitivity vector fields and attractor morphing," *Philosophical transactions. Series A, Mathematical, physical, and engineering sciences*, Vol. 364, 2006, pp. 2515–38.

[33] Lim, J. and Epureanu, B. I., "Multimode dynamics of atomic-force-microscope tip-sample interactions and application of sensitivity vector fields," *Proceedings of SPIE*, Vol. 6529, 2007, pp. 65293Y–1–65293Y–12.

[34] Lim, J. and Epureanu, B. I., "Sensitivity vector fields for atomic force microscopes," *Nonlinear Dynamics*, Vol. 59, No. 1-2, 2010, pp. 113–128.

[35] Yin, S.-H. and Epureanu, B. I., "Experimental enhanced nonlinear dynamics and identification of attractor morphing modes for damage detection," *Journal of Vibration and Acoustics*, Vol. 129, No. 6, 2007, pp. 763–770.

[36] Bradley, C., Daqaq, M. F., Bibo, A., and Jalili, N., "Sensitivity enhancement of cantilever-based sensors using feedback delays," *Journal of Computational and Nonlinear Dynamics*, Vol. 5, No. 4, 2010, pp. 041014–1–041014–9.

[37] Packard, N. H., Crutchfield, J. P., Farmer, J. D., and Shaw, R. S., "Geometry from a time series," *Physical Review Letters*, Vol. 45, No. 9, 1980, pp. 712–716.

[38] Takens, F., "Detecting strange attractors in fluid turbulence," *Dyanamical Systems and Turbulence*, edited by D. Rand and L. S. Young, Springer, Berlin, 1981, pp. 366–381.

[39] Broomhead, D. and King, G., "Extracting qualitative dynamics from experimental data," *Physica D*, Vol. 20, 1986, pp. 217–236.

[40] Sauer, T., Yorke, J. A., and Casdagli, M., "Embedology," *Journal of Statistical Physics*, Vol. 65, No. 3, 1991, pp. 579–616.

[41] Abarbanel, H. D. I., *Analysis of Observed Chaotic Data*, Springer-Verlag, New York, 1996.

[42] Kantz, H. and Schreiber, T., *Nonlinear Time Series Analysis*, Cambridge University Press, Cambridge, 1997.

[43] D'Souza, K. and Epureanu, B. I., "Damage detection in nonlinear systems using system augmentation and generalized minimum rank perturbation theory," *Smart Materials and Structures*, Vol. 14, No. 5, 2005, pp. 989–1000.

[44] D'Souza, K. and Epureanu, B. I., "Sensitivity enhancement for damage detection in linear systems using optimal feedback auxiliary signals and system augmentation," *Proceedings of SPIE*, Vol. 6928, 2008, pp. 692819–1–692819–12.

[45] D'Souza, K. and Epureanu, B. I., "Nonlinear feedback auxiliary signals for system interrogation and damage detection," *Proceedings of the Royal Society A: Mathematical, Physical and Engineering Sciences*, Vol. 464, No. 2100, 2008, pp. 3129–3148.

[46] D'Souza, K. and Epureanu, B. I., "Interrogation of structures using system augmentation and nonlinear feedback auxiliary signals," *Proceedings of SPIE*, Vol. 7292, 2009, pp. 72920H–1–72920H–11.

[47] D'Souza, K., "Damage detection in nonlinear systems using multiple system augmentations and matrix updating," *Proceedings of SPIE*, Vol. 6174, 2006, pp. 61742Y–1–61742Y–12.

[48] D'Souza, K. and Epureanu, B. I., "Multiple augmentations of nonlinear systems and generalized minimum rank perturbations for damage detection," *Journal of Sound and Vibration*, Vol. 316, 2008, pp. 101–121.

[49] Leuridan, J., *Some direct parameter model identification methods applicable for multiple modal analysis*, Ph.D. thesis, University of Cincinnati, 1984.

[50] He, J. and Fu, Z.-F., *Modal analysis*, Butterworth-Heinemann, 2001.

[51] Chelidze, D. and Wenliang, Z., "Smooth orthogonal decomposition-based vibration mode identification," *Journal of Sound and Vibration*, Vol. 292, 2006, pp. 461–473.

[52] Farooq, U. and Feeny, B. F., "Smooth orthogonal decomposition for modal analysis of randomly excited systems," *Journal of Sound and Vibration*, Vol. 316, 2008, pp. 137–146.

[53] D'Souza, K. and Epureanu, B. I., "Noise rejection for two time-based multi-output modal analysis techniques," *Journal of Sound and Vibration*, Vol. 330, 2011, pp. 1045–1051.

[54] Farrar, C. R., Doebling, S. W., and Nix, D. A., "Vibration-based structural damage identification," *Philosophical Transactions of the Royal Society: Mathematical, Physical and Engineering Sciences*, Vol. 359, No. 1778, 2003, pp. 131–149.

[55] Worden, K., Farrar, C. R., Haywood, J., and Todd, M., "A review of nonlinear dynamics applications to structural health monitoring," *Structural Control and Health Monitoring*, Vol. 15, 2008, pp. 540–567.

[56] Chelidze, D. and Cusumano, J. P., "Phase space warping: nonlinear time-series analysis for slowly drifting systems," *Philosophical transactions of the Royal Society A: Mathematical, physical, and engineering sciences*, Vol. 364, No. 1846, 2006, pp. 2495–513.

[57] Todd, M. D., Nichols, J. M., Pecora, L. M., and Virgin, L. N., "Vibration-based damage assessment utilizing state space geometry changes: local attractor variance ratio," *Smart Materials and Structures*, Vol. 10, 2001, pp. 1000–1008.

[58] Epureanu, B. I. and Hashmi, A., "Parameter reconstruction based on sensitivity vector fields," *Journal of Vibration and Acoustics*, Vol. 128, No. 6, 2006, pp. 732–740.

[59] Corron, N. J., Blakely, J. N., and Stahl, M. T., "A matched filter for chaos," *Chaos*, Vol. 20, 2010, pp. 023123–1–023123–10.

[60] Shinbrot, T., Ott, E., Grebogi, C., and Yorke, J. A., "Using chaos to direct trajectories to targets," *Physical Review Letters*, Vol. 65, No. 6, 1990, pp. 3215–3218.

[61] Shinbrot, T., Ditto, W., Grebogi, C., Ott, E., Spani, M., and Yorke, J. A., "Using the sensitive dependence of chaos (the "butterfly effect") to direct trajectories in an experimental chaotic system," *Physical Review Letters*, Vol. 68, No. 19, 1992, pp. 2863–2866.

[62] Melby, P., Kaidel, J., Weber, N., and Hubler, A., "Adaptation to the edge of chaos in the self-adjusting logistic map," *Physical Review Letters*, Vol. 84, No. 26, 2000, pp. 5991–5993.

[63] Garcia, R. and Perez, R., "Dynamic atomic force microscopy methods," *Surface Science Reports*, Vol. 47, No. 6–8, 2002, pp. 197–301.

[64] Ilic, B., Craighead, H., Krylov, S., Senaratine, W., Ober, C., and Neuzil, P., "Attogram detection using nanoelectromechanical oscillators," *Journal of Applied Physics*, Vol. 95, 2004, pp. 3694–3703.

[65] Farmer, J. D. and Sidorowich, J. J., "Predicting chaotic time series," *Physical Review Letters*, Vol. 59, No. 8, 1987, pp. 845–848.

[66] Casdagli, M., "Nonlinear prediction of chaotic time series," *Physica D*, Vol. 35, 1989, pp. 335–356.

[67] Smith, L. A. and Bhansali, R. J., "Local optimal prediction: exploiting strangeness and the variation of sensitivity to initial condition," *Philosophical Transactions of the Royal Society A*, Vol. 348, 1994, pp. 371–381.

[68] Bolt, E. M., "Model selection, confidence, and scaling in predicting chaotic time-series," *International Journal of Bifurcation and Chaos*, Vol. 10, No. 6, 2000, pp. 1407–1422.

[69] Brown, R., Bryant, P., and Abarbanel, H. D. I., "Computing the Lyapunov spectrum of a dynamical system from an observed time series," *Physical Review A*, Vol. 43, 1991, pp. 2787–2806.

[70] Sauer, T., "Time series prediction by using delay coordinate embedding," *Time Series Prediction: Forecasting the Future and Understanding the Past*, edited by A. S. Weigend and N. A. Gershenfeld, Santa Fe Institute, 1994, pp. 175–193.

[71] Kugiumtzis, D., "Regularized local linear prediction of chaotic time series," *Physica D*, Vol. 112, No. 3-4, 1998, pp. 344–360.

[72] Torres, L. A. B. and Aguirre, L. A., "Inductorless Chua's Circuit," *Electronics Letters*, Vol. 36, No. 23, 2000, pp. 1915–1916.

[73] Kennel, M. B., Brown, R., and Abarbanel, H. D. I., "Determining embedding dimension for phase space reconstruction using a geometrical construction," *Physical Review A*, Vol. 45, No. 6, 1992, pp. 3403–3411.

[74] Kennel, M. B. and Abarbanel, H. D. I., "False neighbors and false strands: a reliable minimum embedding dimension algorithm," *Physical Review E*, Vol. 66, No. 2, 2002, pp. 026209.

[75] Fraser, A. M. and Swinney, H. L., "Independent coordinates for strange attractors from mutual information," *Physical Review A*, Vol. 33, No. 2, 1986, pp. 1134–1140.

[76] Buzug, T. and Pfister, G., "Optimal delay time and embedding dimension for delay-time coordinates by analysis of the global and local dynamical behavior of strange attractors," *Physical Review A*, Vol. 45, 1992, pp. 7073–7084.

[77] Hegger, R., Kantz, H., and Schreiber, T., "Practical implementation of nonlinear time series methods: The TISEAN package," *Chaos*, Vol. 9, No. 2, 1999, pp. 413–435.

[78] Thundat, T., Wachter, E. A., Sharp, S. L., and Warmack, R. J., "Detection of mercury-vapor using resonating microcantilevers," *Journal of Vacuum Science and Technology*, Vol. 19, No. 6, 1995, pp. 2825–2828.

[79] Judy, J., Maynes, D., and Webb, B. W., "Characterization of frictional pressure drop for liquid flows through microchannels," *International Journal of Heat and Mass Transfer*, Vol. 45, 2002, pp. 3477–3489.

[80] Laser, D. J. and Santiago, J. G., "Journal of Micromechanical Microengineering," *A review of micropumps*, Vol. 14, 2004, pp. R35–R64.

[81] Robertson, I., Li, L., Sherwin, S. J., and Bearman, P. W., "A numerical study of rotational and transverse galloping rectangular bodies," *Journal of Fluids and Structures*, Vol. 17, 2003, pp. 681–699.

[82] Nakamura, Y. and Mizota, T., "Torsional flutter of rectangular prisms," *Journal of Engineering Mechanics Division*, Vol. 2, 1975, pp. 125–142.

[83] Sodano, H. A., Inman, D. J., and Park, G., "A review of power harvesting from vibration using piezoelectric materials," *The Shock and Vibration Digest*, Vol. 36, 2004, pp. 197–205.

[84] Anton, S. R. and Sodano, H. A., "A review of power harvesting using piezoelectric materials," *Smart Materials and Structures*, Vol. 16, 2007, pp. R1–R21.

[85] Naudascher, E. and Rockwell, D., *Flow Induced Vibrations: An Engineering Guide*, A. A. Balkema, Rotterdam, 2000.

[86] Newman, J. N., *Marine Hydrodynamics*, MIT Press, Cambridge, 1977.

[87] Rhoads, J. F., *Exploring and exploiting resonance in coupled and/or nonlinear microelectromechanical oscillators*, Ph.D. thesis, Michigan State University, 2007.

[88] D'Souza, K. and Epureanu, B. I., "Sensor placement for damage detection in nonlinear systems using system augmentations," *AIAA Journal*, Vol. 46, No. 10, 2008, pp. 2434–2442.

[89] Zimmerman, D. C. and Kaouk, M., "Structural damage detection using a minimum rank update theory," *Journal of Vibration and Acoustics*, Vol. 116, No. 2, 1992, pp. 222–231.

[90] Lakshmanan, M. and Murali, K., *Chaos in Nonlinear Oscillators: Controlling and Synchronization*, Vol. 13 of *Nonlinear Science Series A*, World Scientific, 1996.

[91] Sprott, J. C., "A new class of chaotic circuit," *Physics Letters A*, Vol. 266, 2000, pp. 19–23.

[92] Sprott, J. C., "Simple chaotic systems and circuits," *American Journal of Physics*, Vol. 68, No. 8, 2000, pp. 758–763.

[93] Kiers, K., Klein, T., Kolb, J., Price, S., and Sprott, J. C., "Chaos in a nonlinear analog computer," *International Journal of Bifurcation and Chaos*, Vol. 14, No. 8, 2004, pp. 2867–2873.

[94] Kiers, K., Schmidt, D., and Sprott, J. C., "Precision measurements of a simple chaotic circuit," *American Journal of Physics*, Vol. 72, No. 4, 2004, pp. 503–509.

[95] Liu, M. and Chelidze, D., "Identifying damage using local flow variation method," *Smart Materials and Structures*, Vol. 15, 2006, pp. 1830–1836.

[96] Belongie, S., Malik, J., and Puzicha, J., "Shape matching and object recognition using shape context," *IEEE Transactions on Pattern Analysis and Machine Intelligence*, Vol. 24, No. 24, 2002, pp. 509–522.